

Photovoltaic Materials and Devices 2017

Lead Guest Editor: Bhushan Sopori

Guest Editors: Prakash Basnyat and Srinivas Devayajanam



Photovoltaic Materials and Devices 2017

International Journal of Photoenergy

Photovoltaic Materials and Devices 2017

Special Issue Editor in Chief: Bhushan Sopori

Guest Editors: Prakash Basnyat and Srinivas Devayajanam



Copyright © 2018 Hindawi. All rights reserved.

This is a special issue published in "International Journal of Photoenergy." All articles are open access articles distributed under the Creative Commons Attribution License, which permits unrestricted use, distribution, and reproduction in any medium, provided the original work is properly cited.

Editorial Board

M. S.A. Abdel-Mottaleb, Egypt	Germà Garcia-Belmonte, Spain	Tsuyoshi Ochiai, Japan
Angelo Albini, Italy	Elisa Isabel Garcia-Lopez, Italy	Kei Ohkubo, Japan
Alberto Álvarez-Gallegos, Mexico	M. Ashraf Gondal, Saudi Arabia	Leonardo Palmisano, Italy
Vincenzo Augugliaro, Italy	Giulia Grancini, Switzerland	Thierry Pauporté, France
Detlef W. Bahnemann, Germany	Pierluigi Guerriero, Italy	Philippe Poggi, France
Simona Binetti, Italy	Michael D. Heagy, USA	Francesco Riganti-Fulginei, Italy
Fabio Bisegna, Italy	Wing-Kei Ho, Hong Kong	Leonardo Sandrolini, Italy
Thomas M. Brown, Italy	Jürgen Hüpkes, Germany	Jinn Kong Sheu, Taiwan
Joaquim Carneiro, Portugal	Tariq Iqbal, Canada	Zofia Stasicka, Poland
Yatendra S. Chaudhary, India	Adel A. Ismail, Kuwait	Elias Stathatos, Greece
Věra Cimrová, Czech Republic	Chun-Sheng Jiang, USA	Jegadesan Subbiah, Australia
Juan M. Coronado, Spain	Cooper H. Langford, Canada	K. R. Justin Thomas, India
P. Davide Cozzoli, Italy	Manuel Ignacio Maldonado, Spain	Nikolai V. Tkachenko, Finland
Dionysios D. Dionysiou, USA	Dionissios Mantzavinos, Greece	Ahmad Umar, Saudi Arabia
Abderrazek Douhal, Spain	Santolo Meo, Italy	Thomas Unold, Germany
Mahmoud M. El-Nahass, Egypt	Claudio Minero, Italy	Mark van Der Auweraer, Belgium
Polycarpos Falaras, Greece	Antoni Morawski, Poland	Wilfried G.J.H.M. Van Sark, Netherlands
Chris Ferekides, USA	Fabrice Morlet-Savary, France	Xuxu Wang, China
Paolo Fornasiero, Italy	Mohammad Muneer, India	Yanfa Yan, USA
Manuel Fuentes Conde, Spain	Maria da Graça P. Neves, Portugal	Jiangbo Yu, USA

Contents

Photovoltaic Materials and Devices 2017

Bhushan Sopori , Prakash Basnyat, and Srinivas Devayajanam 
Editorial (2 pages), Article ID 5717323, Volume 2018 (2018)

Performance Investigation of Air Velocity Effects on PV Modules under Controlled Conditions

Muzaffar Ali, Muhammad Hasan Iqbal, Nadeem Ahmed Sheikh, Hafiz M. Ali, M. Shehryar Manzoor, Muhammad Mahabat Khan, and Khairul Fikri Tamrin
Research Article (10 pages), Article ID 3829671, Volume 2017 (2018)

The Design and Optimization of GaAs Single Solar Cells Using the Genetic Algorithm and Silvaco ATLAS

Kamal Attari, Lahcen Amhaimar, Ali El yaakoubi, Adel Asselman, and Mounir Bassou
Research Article (7 pages), Article ID 8269358, Volume 2017 (2018)

Characteristics of Nanocrystallite-CdS Produced by Low-Cost Electrochemical Technique for Thin Film Photovoltaic Application: The Influence of Deposition Voltage

Obi Kingsley Echendu, Francis Birhanu Dejene, Imyhamy Mudiy Dharmadasa, and Francis Chukwuemeka Eze
Research Article (13 pages), Article ID 3989432, Volume 2017 (2018)

The Effects of Interdot Spacing and Dot Size on the Performance of InGaAs/GaAs QDIBSC

Sayed Amina Amin, Md. Tanvir Hasan, and Muhammad Shaffatul Islam
Research Article (10 pages), Article ID 9160381, Volume 2017 (2018)

Optical Tests on a Curve Fresnel Lens as Secondary Optics for Solar Troughs

D. Fontani, P. Sansoni, F. Francini, M. DeLucia, G. Pierucci, and D. Jafrancesco
Research Article (11 pages), Article ID 1945875, Volume 2017 (2018)

Editorial

Photovoltaic Materials and Devices 2017

Bhushan Sopori^{ID},¹ Prakash Basnyat,² and Srinivas Devayajanam^{ID}²

¹National Renewable Energy Laboratory, 21564 Shady Lane, Idledale, CO 80453, USA

²New Jersey Institute of Technology, 138 Warren Street, University Heights, Newark, NJ 07102, USA

Correspondence should be addressed to Bhushan Sopori; bhushan.sopori@gmail.com

Received 26 October 2017; Accepted 26 October 2017; Published 19 April 2018

Copyright © 2018 Bhushan Sopori et al. This is an open access article distributed under the Creative Commons Attribution License, which permits unrestricted use, distribution, and reproduction in any medium, provided the original work is properly cited.

The demand of photovoltaic energy has continued to grow in recent years concomitant with a decrease in the module prices. There continues to be slight overcapacity of production despite large installations worldwide, particularly in China and the USA. The global capacity additions in 2017 are expected to reach 79 gigawatts (GW), slightly higher than 77 GW in 2016. While most of the solar cell manufacturing is occurring in China, there is a growing interest in developing module assembly in many other countries (particularly in India). As the manufacturing volume grows, there is continued reduction in the manufacturing cost. However, there continues to be considerable need for further research into improved cell/module designs and fabrication technology. This is the 4th special issue of the *International Journal of Photoenergy* on “Photovoltaic Materials and Devices” and is a very short assembly of accepted papers from a much wider submission, aimed at recent advances in materials and PV systems. This issue contains 5 papers on various aspects of photovoltaics, which are briefly described here.

Research paper “Optical Tests on a Curve Fresnel Lens as Secondary Optics for Solar Troughs” by D. Fontani et al. reveals the development of curved Fresnel lens as a secondary concentrator for solar parabolic troughs used during solar thermal collection. Results for the accuracy of the realized shape of cylindrical Fresnel lens (CFL) based on optical characterization of various samples are also presented. The study and the tests have made possible to detect the criticality of the first CFL prototypes and they provide some precise indications of the possible implementation plans during the lens construction processes which can be considered as the main responsible factors for loss of optical lens performance.

The paper by O. K. Echendu et al. entitled “Characteristics of Nanocrystallite-CdS Produced by Low-Cost Electrochemical Technique for Thin Film Photovoltaic Application: The Influence of Deposition Voltage” presents electrodeposition of cadmium sulfide thin films at different cathodic growth voltages and characterization of the films before and after postdeposition heat treatment. Postdeposition annealing results in phase transformation which leaves the films with only the hexagonal crystal phase and reduced strain and dislocation density while increasing the crystallite sizes.

Article written by S.A. Amin et al. “The Effects of Interdot Spacing and Dot Size on the Performance of InGaAs/GaAs QDIBSC” elucidates the wave behavior of charge carriers inside the dot and its barrier with varying dot size and interdot spacing. Based on the behavior of electron wave function, they found that changing the dot spacing leads to a change in the intermediate band (IB) width and in the density of states, whereas varying the size of dots leads to a formation of a second IB. Presented results suggest that multiple IBs can potentially improve the efficiency, if the widths and positions of the IBs are optimized.

Paper submitted by M. Ali et al. “Performance Investigation of Air Velocity Effects on PV Modules under Controlled Conditions” to this journal sheds light on the efficacy of air cooling on solar panels. An experimental investigation was carried using a wind tunnel and an artificial solar simulator. Change in surface temperature, power output, and efficiency of PV modules under different air velocity in different direction was studied. Thermal analysis of the modules is performed through ANSYS Fluent in which

junction temperature and heat flux of modules are determined. Experiments helped in determining the optimum tilt angle with the incoming air flow to increase the performance parameters for both the (c-Si and poly Si) modules.

K. Attari's paper "The Design and Optimization of GaAs Single Solar Cells Using the Genetic Algorithm and Silvaco ATLAS" proposes a cell structure with new buffer layer and the back surface filled (BSF) that can significantly improve the performance due to higher collection of photo-generated minority carriers. The work demonstrates the simulation based on MATLAB algorithm of a maximum output power solar cell and its optimization. Effect of doping densities, thickness of cell layers, and choice of materials on various cell parameters was monitored. Results suggest an improvement in the conversion efficiency of up to 29.7%.

We hope that readers will enjoy this issue.

Acknowledgments

Special thanks are due to Nadine Abdelhay for her continued help in coordinating this issue.

*Bhushan Sopori
Prakash Basnyat
Srinivas Devayajanam*

Research Article

Performance Investigation of Air Velocity Effects on PV Modules under Controlled Conditions

Muzaffar Ali,¹ Muhammad Hasan Iqbal,² Nadeem Ahmed Sheikh,³ Hafiz M. Ali,¹ M. Shehryar Manzoor,¹ Muhammad Mahabat Khan,³ and Khairul Fikri Tamrin⁴

¹*Mechanical Engineering Department, University of Engineering and Technology Taxila, Taxila, Pakistan*

²*Mechanical Engineering Department, COMSATS Sahiwal, Sahiwal, Pakistan*

³*Mechanical Engineering Department, Faculty of Engineering, HITEC University, Taxila, Pakistan*

⁴*Department of Mechanical and Manufacturing Engineering, Faculty of Engineering, Universiti Malaysia Sarawak (UNIMAS), 94300 Kota Samarahan, Sarawak, Malaysia*

Correspondence should be addressed to Muzaffar Ali; muzaffar.ali@uettaxila.edu.pk

Received 26 May 2017; Accepted 6 August 2017; Published 12 December 2017

Academic Editor: Srinivas Devayajanam

Copyright © 2017 Muzaffar Ali et al. This is an open access article distributed under the Creative Commons Attribution License, which permits unrestricted use, distribution, and reproduction in any medium, provided the original work is properly cited.

Junction temperature of PV modules is one of the key parameters on which the performance of PV modules depends. In the present work, an experimental investigation was carried out to analyze the effects of air velocity on the performance of two PV modules, that is, monocrystalline silicon and polycrystalline silicon under the controlled conditions of a wind tunnel in the presence of an artificial solar simulator. The parameters investigated include the surface temperature variation, power output, and efficiency of PV modules under varying air velocity from near zero (indoor lab. conditions) to 15 m/s. Additionally, the results were also determined at two different module angular positions: at 0° angle, that is, parallel to air direction and at 10° angle with the direction of coming air to consider the effects of tilt angles. Afterwards, the thermal analysis of the modules was performed using Ansys-Fluent in which junction temperature and heat flux of modules were determined by applying appropriate boundary conditions, such as air velocity, heat flux, and solar radiation. Finally, the numerical results are compared with the experiment in terms of junction temperatures of modules and good agreement was found. Additionally, the results showed that the maximum module temperature drops by 17.2°C and the module efficiency and power output increased from 10 to 12% with increasing air velocity.

1. Introduction

With the increasing demand of energy, attention of researchers is titillating towards the renewable energy sector. PV cells have gained much attention in past couple of years. The total PV capacity of all major countries increased from about 40 GW to 100 GW during 2010–2012 [1]. With the rising demand of energy and environmental effects of other energy sources, an efficient utilization of solar energy is considered to be the best way for power generation [2, 3].

Although PV system allows direct electrification of solar energy, however, it faces severe limitations when the surface temperature of the module increases. Generally, high solar irradiance comes with higher ambient temperatures especially in climatic zones such as Pakistan. For such zones,

energy utilization efficiency of PV systems can be improved through different methods for instances: multijunction cells [4], optical frequency shifting [5], multiple generation cells [6], hot carrier cells [7], and concentration photovoltaic system [8]. However, such methods have not been yet commercialized because of their complexity and high cost. Therefore, cheap and simple methods to improve the efficiency of PV systems become the basic need of this technology especially in those areas where high temperatures are experienced.

The standard test conditions of typical photovoltaic modules consist of global irradiance of 1000 W/m², module temperature of 25°C, and air mass 1.5 (according to IEC 61215/IEC 61646 tests) in which certified measurement was performed by TÜV immissionsschutz und Energiesysteme GmbH (Cologne, Germany) [9]. However, these values may

not comply with the measurements in actual operating conditions because of variations in several environmental parameters [10]. Therefore, the predicted module performance deviates under real climate conditions. PV panels absorb around 80% of the incident solar irradiation but their maximum theoretical conversion efficiency is not more than 30% due to various losses [11, 12]. A major cause of these losses is the heat generation during absorption of photons that results in high junction temperature causing thermalization that decreases output power and efficiency of PV cells. In order to gain the maximum efficiency from PV cells, their junction temperature is required to be kept low, that is, around 25°C.

Several studies have been conducted to study the dependence of module performance on its junction temperature. In a reported work, it was investigated that with the increase in the junction temperature, the reverse saturation current increases which causes a decrease in the open circuit voltage (V_{oc}); thus, the efficiency of modules decreases [13].

In another similar study, it was observed that the efficiency of PV modules depends upon many environmental parameters out of which temperature plays a vital role on the performance of modules. The investigation carried out at high irradiance showed that the module working temperature will be high resulting in lower efficiency of modules [14]. In one of the research work, an active cooling system for solar panels was proposed and investigated showing that when there is no active cooling, the efficiency of panels was about 9%, and with active cooling, the temperature of the panel decreases appreciably with their efficiency increased up to 12-13% [15].

In a study, the effects of other environmental variables such as dust, humidity, and air velocity on the efficiency of solar panels were investigated. Accumulation of dust on panel surface and increase in relative humidity causes a decrease in the efficiency of panels. When air flows on the surface of panels it is expected to blow away dust particles and remove the heat from the panel surface, primarily through convection. This decreases the temperature of panels and also results in the decrease of local relative humidity, and the overall result is increased efficiency of the panels [16]. To reduce the cell temperature, a research was carried out to investigate the effects of microchannel cooling of PV cells on their efficiency. This approach resulted in a 14% increase in power output with a temperature drop of up to 15°C. This temperature drop was caused by water flow in microchannels on the back surface of cells at the rate of 3 LPM [17].

The body of cited literature suggests that a number of studies have been carried out to study the influence of various external parameters and mechanisms on performance of PV modules. From the commercial point of view, wind blowing over the installed PV modules whether on small scale or large scale provides a simple and economical solution. However, such solution requires investigation and quantification in a controlled situation. Until now no appropriate quantificational assessment on the airflow over PV module has not been studied in detail. In order to

ascertain the influence of airflow, in a parametric fashion, a controlled experimental setup is required for testing. Here, a controlled set of conditions is established by placing the PV panel in a wind tunnel with exact quantification of airflow and its direction. The real-time performance of the PV module is assessed in presence of an artificial solar simulator. This experiment is designed to quantify the influence of air velocity on the performance of PV module. As the solar panels are installed at a specific tilt, the effect of tilt angle is also studied so that the results can be utilized, with confidence, while designing cooling mechanisms for PV modules.

2. Methodology

Maximum power of the PV module is the product of maximum current and maximum voltage as determined by

$$P_{\max} = E_{\max} I_{\max}. \quad (1)$$

Module efficiency is determined by

$$\eta_m = \frac{P_{\max}}{I_{rr}A}, \quad (2)$$

where I_{rr} is the amount of solar radiation in W/m² and A is the active area of cells on which the radiation is focused. The heat flux on the surface of cell is measured by

$$Q = hA(T_s - T_a), \quad (3)$$

where h is the convective heat transfer coefficient, T_s is the junction temperature of panel, and T_a is the temperature of incoming air. The relationship as expressed through 4 is used to determine the convective heat transfer coefficient, primarily for laminar flow [18].

$$h = 3.83 V^{0.5} L^{-0.5}, \quad (4)$$

where V is the upstream air velocity and L is the characteristic length of the module.

2.1. Experimental Setup and Procedure. Experiments were conducted to estimate the behavior of different types of PV modules under controlled conditions. PV modules were placed on a moveable stand placed inside the wind tunnel test section (dimension: 0.13 × 0.093 ft²) made with Perspex glass. There were four K-type thermocouples attached to the backside of PV module. The test box was mounted with a low subsonic wind tunnel (model number HM 170) with a maximum airspeed of 25 m/s. The platform was placed at the center of the wind tunnel test section. The test section was placed under an artificial solar simulator (model number TRM-PD) having a maximum electrical power of 3 kW. The platform with PV cells was placed right beneath the solar simulator so that maximum radiations directly fall on the module. The actual experimental setup is shown in Figure 1. The rated specifications of the PV modules (manufactured by Polysun Energy) are given in Table 1.

Air velocity inside the wind tunnel was controlled using a calibrated inclined manometer. The intensity of incident

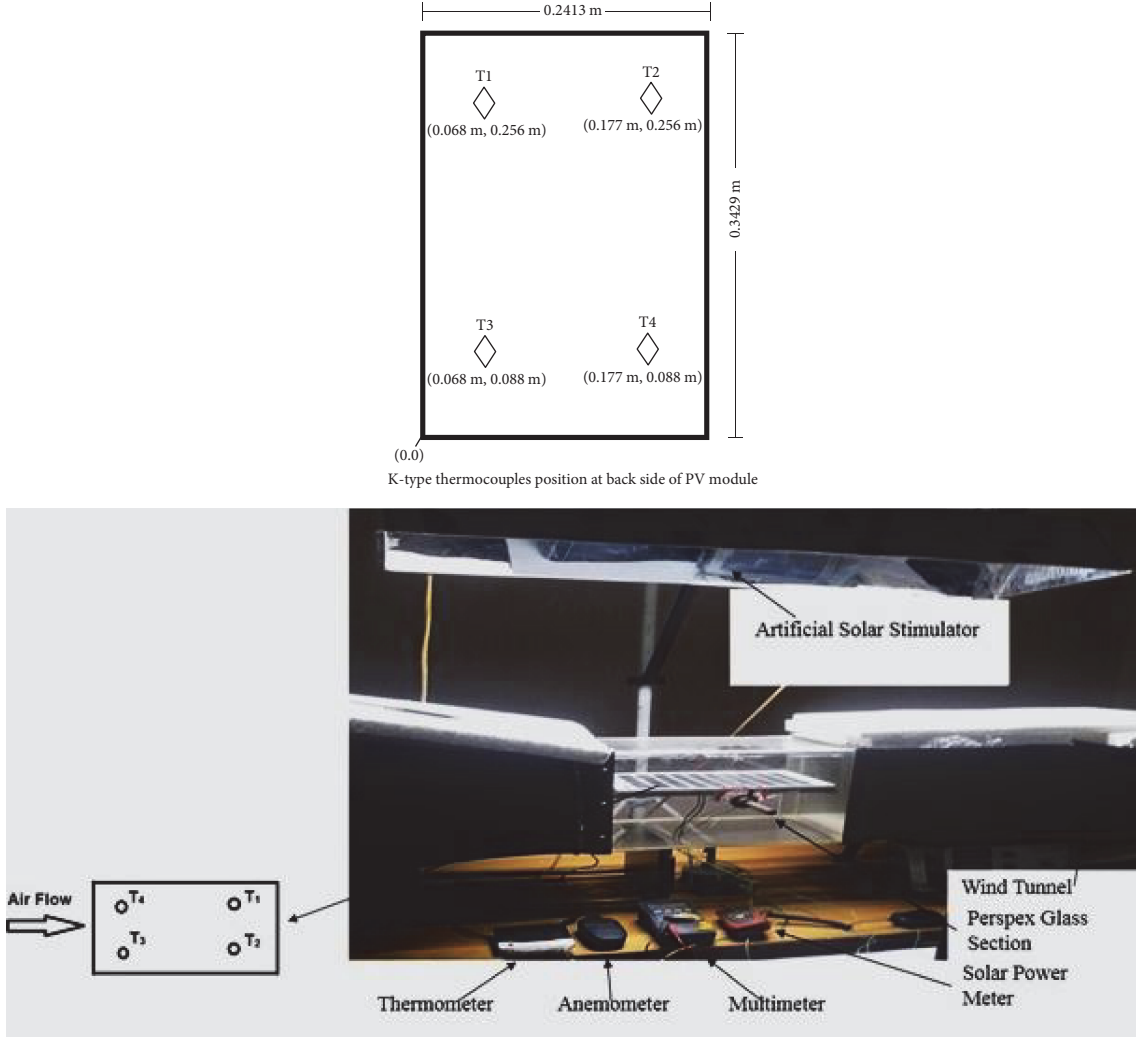


FIGURE 1: Schematic description of placement of thermocouples on PV module and the actual experimental setup in the wind tunnel.

TABLE 1: Module specifications.

Module design parameters	c-Si	p-Si
Module dimensions (mm × mm)	342.9 × 241.3	342.9 × 241.3
Module area (m ²)	0.0816	0.0816
Maximum power, P_{\max} (W)	10 W ± 3%	10 W ± 3%
Maximum current, I_{\max} (A)	0.56	0.57
Maximum voltage, E_{\max} (V)	18	17.5
Short circuit current, I_{sc} (A)	0.64	0.66
Open circuit voltage, V_{oc} (V)	21.6	21.5

radiations was measured through solar power meter (model number (Amprobe Solar-100)). For temperature measurement on the surface of the PV panel, four K-type thermocouples were installed on the backside of panels with the help of a heat-conducting adhesive. The temperature of panel surface with air approaching and leaving the module was measured through these thermocouple probes.

Initial performance of the PV panels was noted at zero wind conditions (static wind tunnel fan) under the solar simulator only. The temperature and relevant parameters of the modules were recorded until the average surface temperature of the panel reached 40°C. Afterwards, similar measurements were made at different airflow velocities at fixed incident radiations. A similar procedure was repeated for PV panels tilted at an angle of 10° with the horizontal. The set of measurements include the incident intensity of radiation, temperature of module at four points, and current and voltage produced by the PV panel. The measurements were made for sufficiently long durations so that time averaged steady values are noted and these values are then used for further calculations and comparisons. The velocity of the wind was increased incrementally and the same procedure was adopted. The temperatures of the module were measured only once stable condition is achieved at a set wind speed. The same set of experiments was repeated for both mono- and polycrystalline modules at both 0° and 10° tilt angles. The purpose of introducing the tilt angle was to analyze the

TABLE 2: Calculation of Reynolds number.

Velocity (m/s)	Reynolds number
5	116,405.8
6	139,687
7	162,968.1
8	186,249.3
9	209,530.5
10	232,811.6
11	256,092.8
12	279,374
13	302,655.1
14	325,936.3
15	349,217.4

effects of airflow over the actual installation configuration of modules in tilted mode.

2.2. Numerical Analysis. The process of heat transfers from the surface of modules due to varying flow speeds is analyzed using numerical simulations. As the experiments were conducted under controlled conditions, the rate of heat removal from the surface of the module can be simulated and results can be compared with experimental measurements. Using a commercial CFD code (Fluent), flow over a 2D flat plate, mimicking the module, is simulated at varying airspeeds. It was noted that under zero wind conditions, the maximum temperature of the modules was raised to 40°C due to radiations of the solar simulator and power generation of panels. Under zero wind speed, heat flux generated by the module was calculated using the surface temperature measurements and is used as a boundary condition for the simulations. Under constant influx of radiations, it is assumed that the heat flux generated by the panel does not change significantly. However, the surface temperatures of the module are expected to vary at varying flow velocities and numerical simulations are used to predict the surface temperature variations.

For flow over a flat plate, transition from laminar to turbulent is usually taken to occur at the critical Reynolds number. The value of the critical Reynolds number for a flat plate may vary from 5×10^5 to 3×10^6 , depending on the surface roughness and the turbulence level of the free stream [19]. Maximum Reynolds number for the study was calculated 3.5×10^5 as given in Table 2 where density is 1.225 kg m^{-3} , viscosity is $0.00001789 \text{ N s m}^{-2}$, and characteristic length L is 0.34 m, so the flow over the flat module was assumed to remain laminar.

Temperature of the incoming airflow was measured during experiments and kept at $T_{\text{air}} = 293 \text{ K}$ for all simulations. The flow at the inlet was assumed to be uniform with its magnitude ranging from 5 to 15 m/s. The simulated geometry and relevant boundaries are indicated in Figure 2.

2.2.1. Governing Equations and Boundary Conditions. The simulation involves solving balances of mass, momentum, and energy with relevant boundary conditions. The set of

equations for incompressible, steady laminar flow of fluid with constant physicochemical properties are as follows:

Continuity equation

$$\frac{\partial U}{\partial X} + \frac{\partial V}{\partial Y} = 0, \quad (5)$$

X-momentum equation

$$\frac{\partial(UU)}{\partial X} + \frac{\partial(VU)}{\partial Y} = -\frac{(\partial p/\partial X) + (\partial^2 U/\partial X^2) + (\partial^2 U/\partial Y^2)}{Re}, \quad (6)$$

Y-momentum equation

$$\frac{\partial(UV)}{\partial X} + \frac{\partial(VV)}{\partial Y} = -\frac{(\partial p/\partial Y) + (\partial^2 V/\partial X^2) + (\partial^2 V/\partial Y^2)}{Re}, \quad (7)$$

Thermal energy equation

$$\frac{\partial(U\theta)}{\partial X} + \frac{\partial(V\theta)}{\partial Y} = \frac{(\partial^2\theta/\partial X^2) + (\partial^2\theta/\partial Y^2)}{RePr}, \quad (8)$$

where Reynolds and Prandtl numbers are defined as

$$\begin{aligned} Re &= \frac{(LU\rho)}{\mu}, \\ Pr &= \frac{(\mu c_p)}{k}. \end{aligned} \quad (9)$$

No slip condition was used over the cylinder surface with uniform heat flux thermal boundary condition.

For uniform heat flux, the nondimensional temperature is given as $\theta = T - T_{\infty}/(q_w D/k)$. q_w is specified heat flux, D is characteristic length, and k is thermal conductivity.

2.2.2. Numerical Details. For the problem in consideration, computational grid was generated using Gambit software and the numerical calculations were accomplished using a computational fluid dynamics (CFD) solver FLUENT (14.0). A multiblock-structured grid was used. Figure 3 shows the grid employed for the simulations and results reported in this paper.

In order to establish grid independence of results, a detailed study was conducted. Computations were performed on 3 different grids in order to get domain-independent results. The total number of grid points was varied to select the grid that generates accurate results with a minimum number of nodes to save computation time. The number of elements in grid 3 was more than grid 2 and grid 1 but the results obtained from executing grid 3 were more accurate and precise than the results attained from grid 1 and grid 2 as shown in Table 3. Therefore, grid 3 was selected with a total of 38,230 cells.

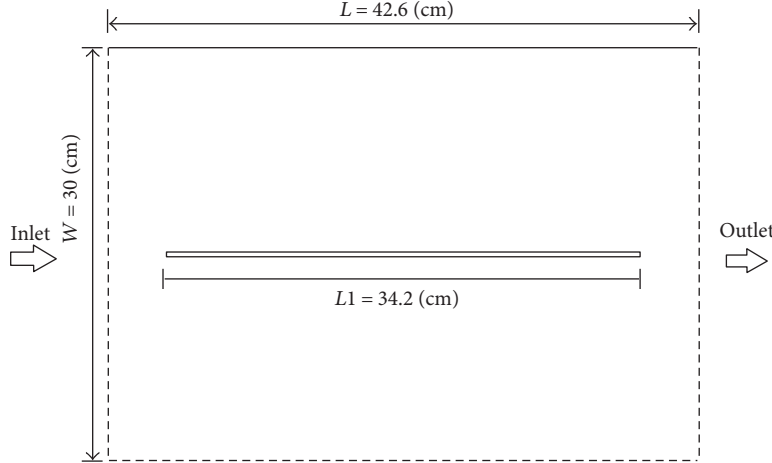


FIGURE 2: Schematic diagram of unconfined flow on module.

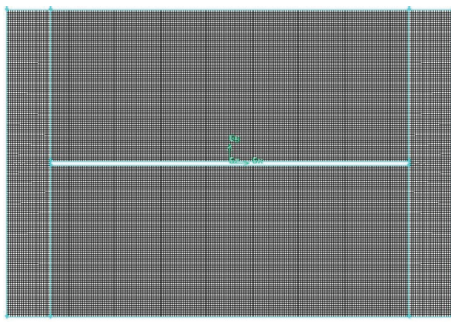


FIGURE 3: Grid structure corresponding to G3 (Table 3) for the simulation.

3. Results and Discussion

After comprehensive numerical and experimental analysis, results are presented in terms of module power, temperature, and efficiency.

3.1. Module Temperature Analysis

3.1.1. Experimental Variation of the Surface Temperature of the PV Module with the Airflow Velocity. Figure 4 shows experimental results of temperature for monocrystalline and polycrystalline modules. Figures 4(a) and 4(b) show the temperature results obtained from monocrystalline module at positions 0° and 10°, respectively, while Figures 4(c) and 4(d) show the trends obtained from the polycrystalline module. The temperatures at four different points on the module are represented. Additionally, the average temperature of module is also shown. It can be observed that temperatures labeled as T1 and T2 are slightly high compared to temperatures T3 and T4. This is due to the fact that air gets heated along its flow path from point T3 and T4 to point T1 and T2. In the presence of a solar simulator, the temperature readings were recorded with an average temperature of module reaching 40°C (maximum temperature considered in the current

study). At higher velocities, the temperature of the monocrystalline module decreases up to 16.8°C compared to zero velocity measurement. Whereas the drop in temperature for polycrystalline module was up to 17.2°C compared to zero velocity measurement as shown in Figure 4. It can be concluded that there was a significant drop in temperature when the airflow velocity was at 5 m/s. However, at velocities greater than 15 m/s, the temperature depression was not significant.

3.1.2. Calculation of the Temperature Variation of the PV Cells with Air Velocity. Figures 5(a)–5(d) show the temperature results along the length of monocrystalline and polycrystalline PV modules at velocities of 5, 8, 12, and 15 m/s. The results show that the temperature of panel increased along the length of the panel; this is due to the fact that air gets heated up as it flows over the panel along the length and heat transfer rate decreases due to decrease in temperature difference.

A comparison of numerical simulations with experimental results is represented in Figure 6. The simulation results near the leading tip of the module are compared with the average temperature of points (T3, T4) as shown in Figures 6(a), 6(c), 6(e), and 6(f). While the simulated results at the trailing end of module were compared with the average temperature of points (T1, T2) as shown in Figures 6(b), 6(d), 6(f), and 6(h). The comparison indicates that the results of temperatures obtained experimentally are in good agreement with the numerically achieved results as the trend of both lines is almost the same and the difference between the results was found to be around 2°C, mainly towards the leading tip. The expected reason for the deviation is flow transition taking place inside the wind tunnel, which could have disturbed the leading edge flow patterns. Also, the leading point of the boundary layer has high local heat transfer coefficient, and deviation of around 10% at the leading edge is quite admissible. The numerical simulations showed good agreement with experimental findings, especially after the leading edge as shown in Figures 6(b), 6(d), 6(f), and 6(h). This comparison shows a reliable means to directly estimate

TABLE 3: Details of meshes tested in grid independence.

Grid	Nodes	Number of cells	Domain size (cm)	Step size Δt (s)	Experimental temperature of module (K)	Fluent temperature of module (K)	Difference in temperature (K)
G1	25,002	24,272	30×42.6	0.0008	297.4	293.9	3.5
G2	36,492	35,600	30×42.6	0.0008	297.4	295.4	2
G3	39,246	38,320	30×42.6	0.0008	297.4	296.1	1.3

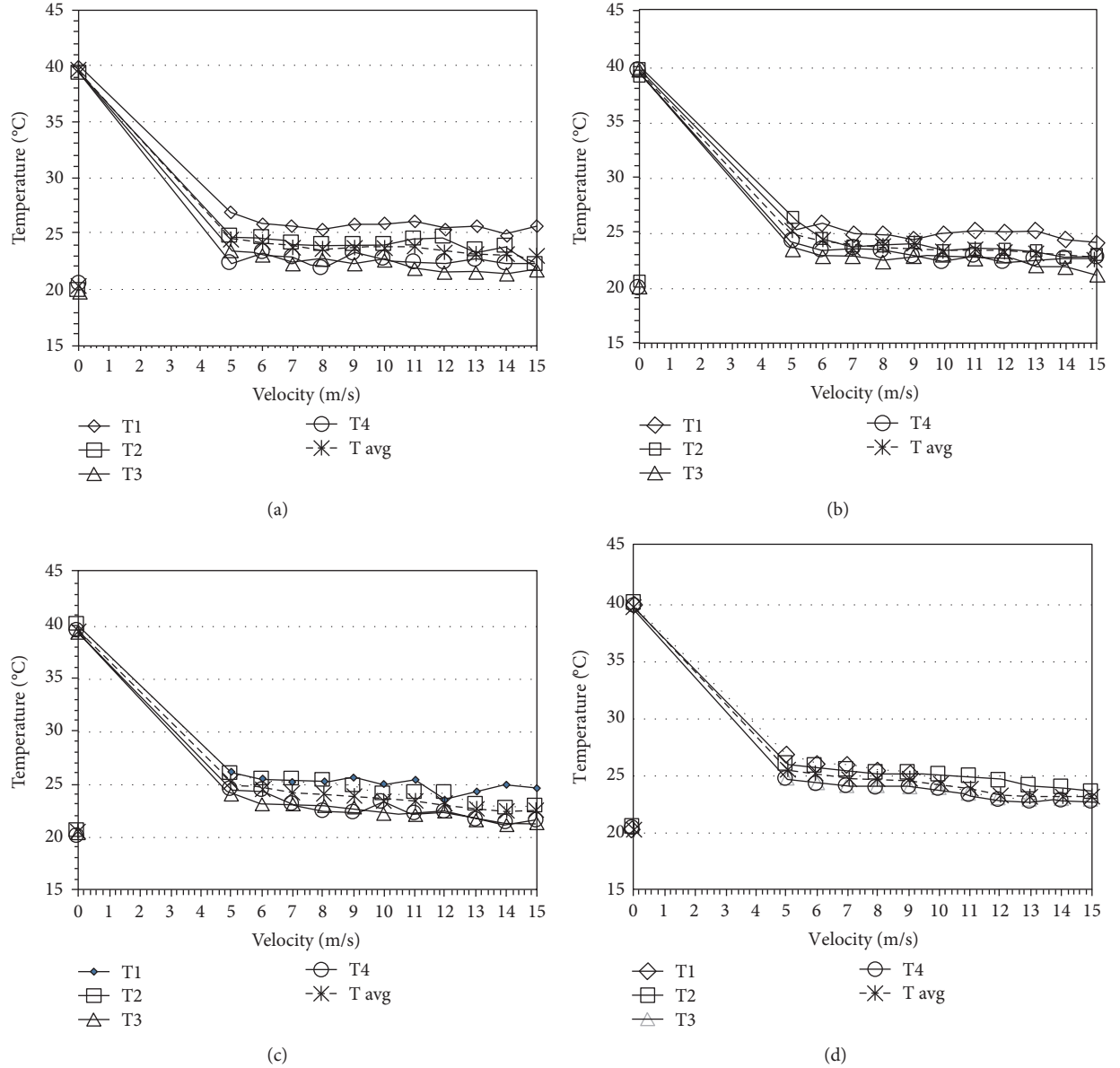


FIGURE 4: Variation of temperature with velocity. (a) Monocrystalline at 0°, (b) monocrystalline at 10°, (c) polycrystalline at 0°, and (d) polycrystalline at 10°.

surface temperatures over the complete surface of the module. Furthermore, the numerical methods can be directly employed in real-time scenarios and configurations.

3.2. Variation of Module Power and Efficiency with Air Velocity

Figure 7 shows the effect of velocities on the power

of modules. Initially, at high temperature, the module power was recorded low when the air velocity was almost negligible, while at higher velocities, the module power increases due to the decrease in temperature of module. Maximum power achieved was 7.5 W for monocrystalline module and 4.8 W for polycrystalline module under considered conditions.

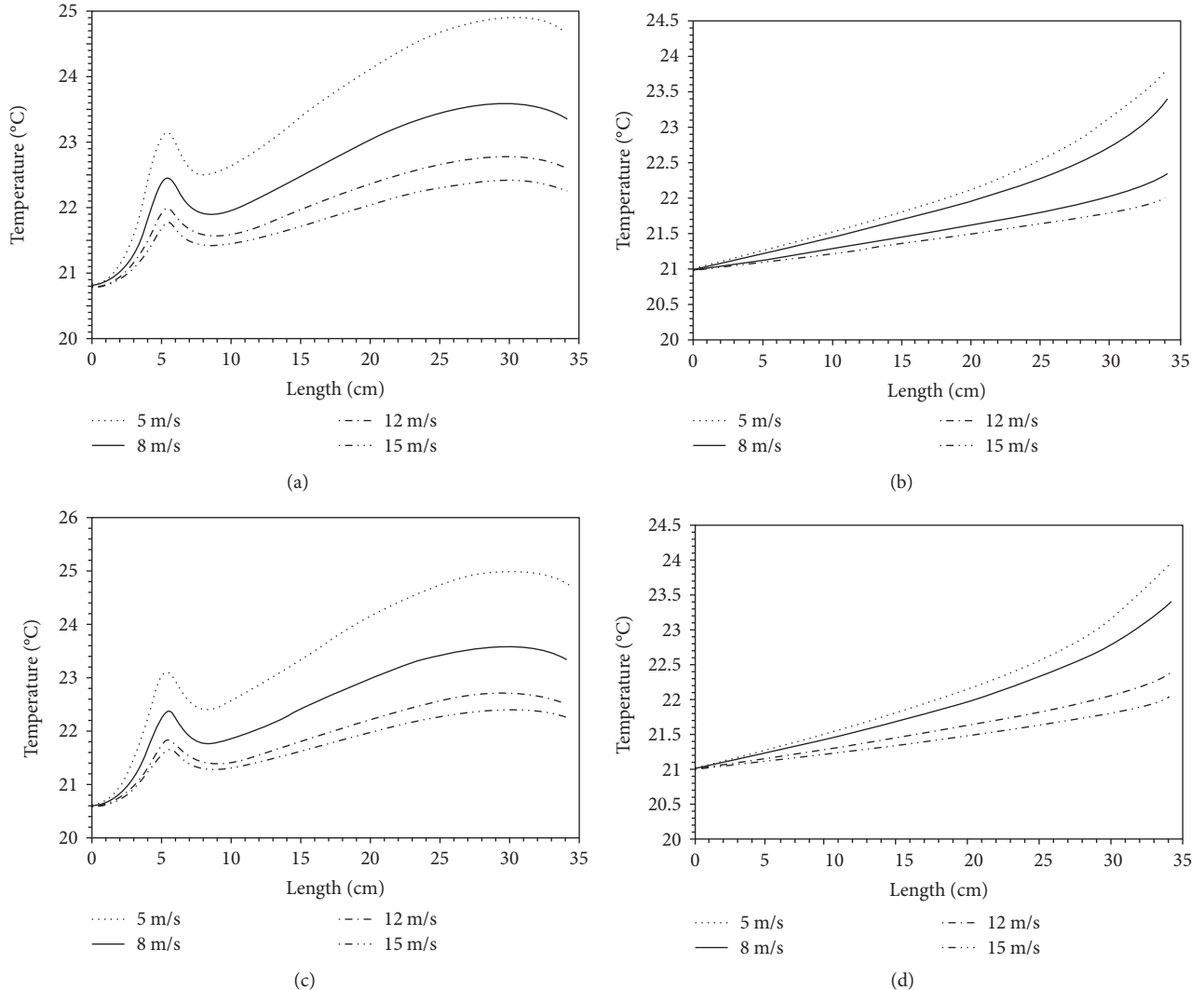


FIGURE 5: PV module surface temperature along length. (a) Monocrystalline at 0° , (b) monocrystalline at 10° , (c) polycrystalline at 0° , and (d) polycrystalline at 10° .

Figures 7(a) and 7(b) show the results for monocrystalline and polycrystalline modules correspondingly. The variation in angles of modules from 0° to 10° results in additional air contact with modules, owing to which further decrease in temperature and increase in power are observed.

Figure 8 indicates that the efficiency of photovoltaic modules followed exactly the same trend as shown in Figure 7. The efficiency of modules is directly proportional to the power. The increase in power and efficiency of monocrystalline and polycrystalline modules at position 0° with the airflow was found to be 10–15% and 5–10%, respectively, while in the case of tilt angle of 10° with the incoming airflow, increase in performance parameters for both modules is found to be 11–18% and 8–12%, respectively, at considered velocity range. Thus, it can be concluded that the effects of airflow on the modules' power and efficiency at a tilt angle of 10° are better than at 0° . Furthermore, from these results, it can be also concluded that the effects of airflow on monocrystalline module are

significant compared to the polycrystalline module under the same conditions.

4. Conclusions and Future Work

The effect of blowing wind on photovoltaic modules was studied experimentally and results are compared with numerical simulations. It is observed that the effect of wind on the temperature of PV module is significant, which results in increase of power and efficiency of modules. Results showed that at moderate velocity of air, significant change in module temperature is observed. Further higher velocities of air do not necessarily increase the advantage. At air velocity range of 5 to 15 m/s up to 42%, decrease in average temperature of monocrystalline module was observed whereas the drop in temperature for polycrystalline module was up to 43%. This leads to increase in power and efficiency of monocrystalline and polycrystalline modules. Moreover, the influence of inclination angle is also significant. At tilt

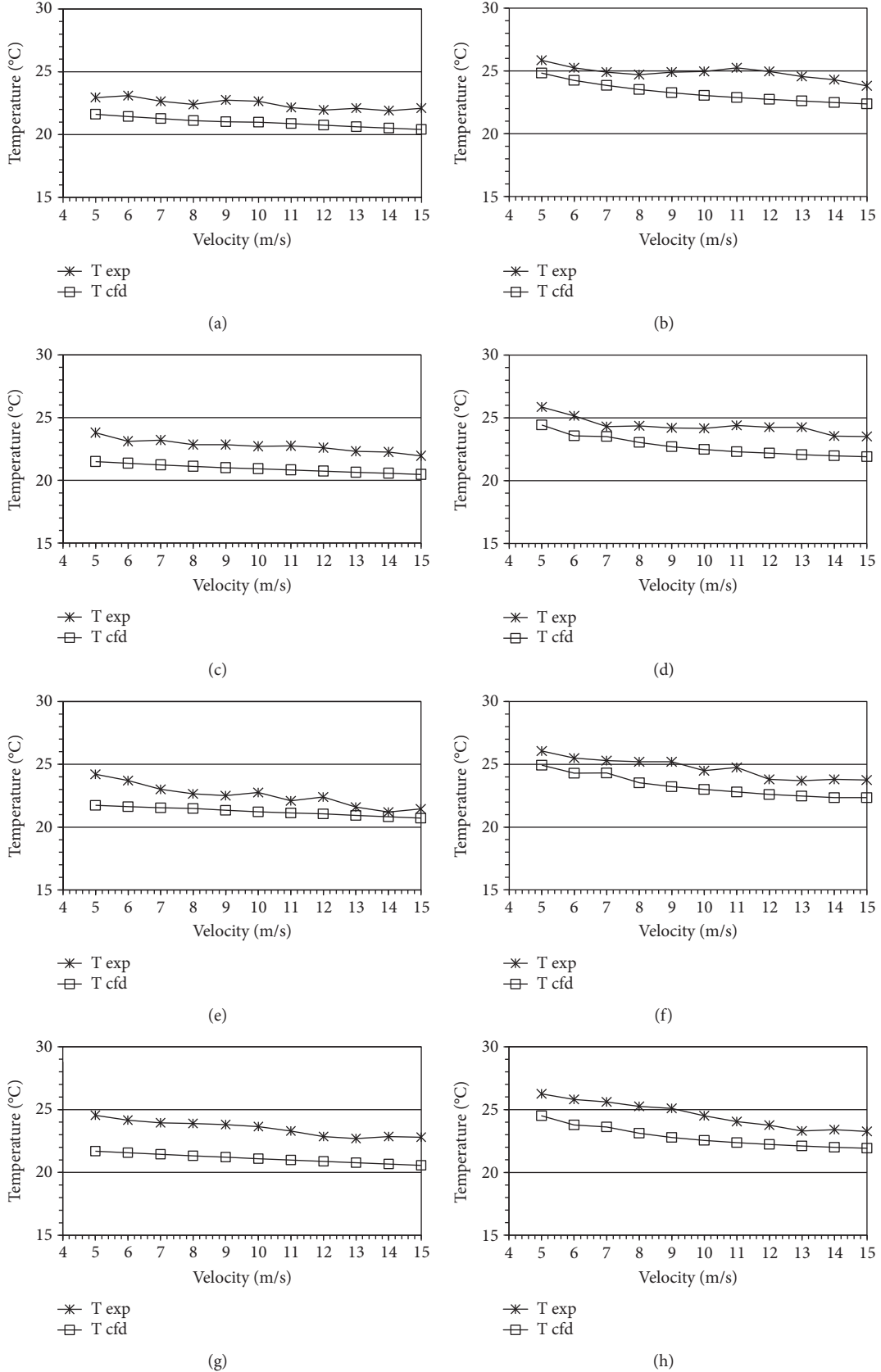


FIGURE 6: Comparison between experimental and CFD temperature results. (a) Monocrystalline at 0° initial point, (b) monocrystalline at 0° final point, (c) monocrystalline at 10° initial point, (d) monocrystalline at 10° final point, (e) polycrystalline at 0° initial point, (f) polycrystalline at 0° final point, (g) polycrystalline at 10° initial point, and (h) polycrystalline at 10° final point.

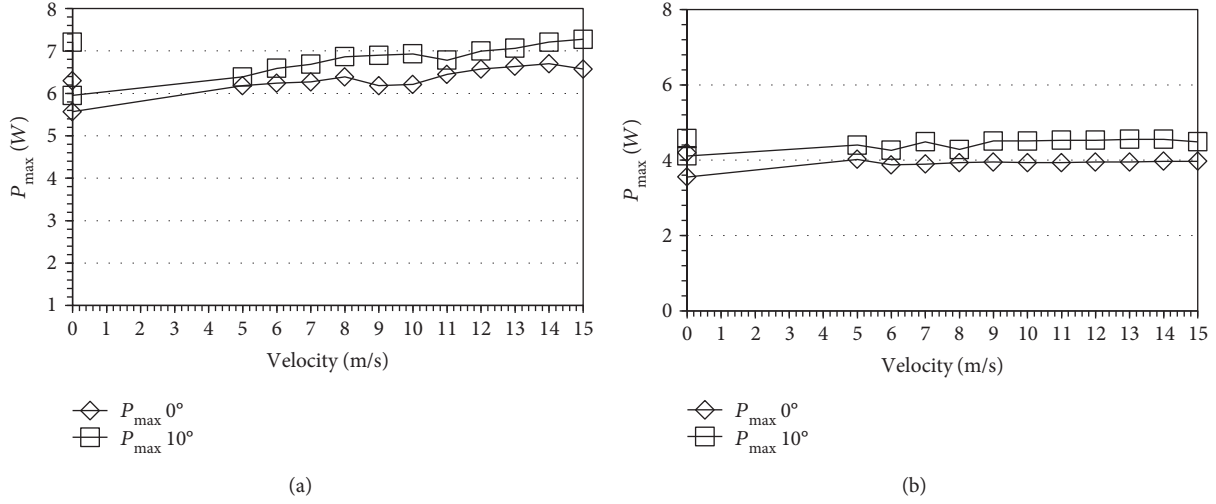


FIGURE 7: Modules power at different velocities. (a) Monocrystalline and (b) polycrystalline.

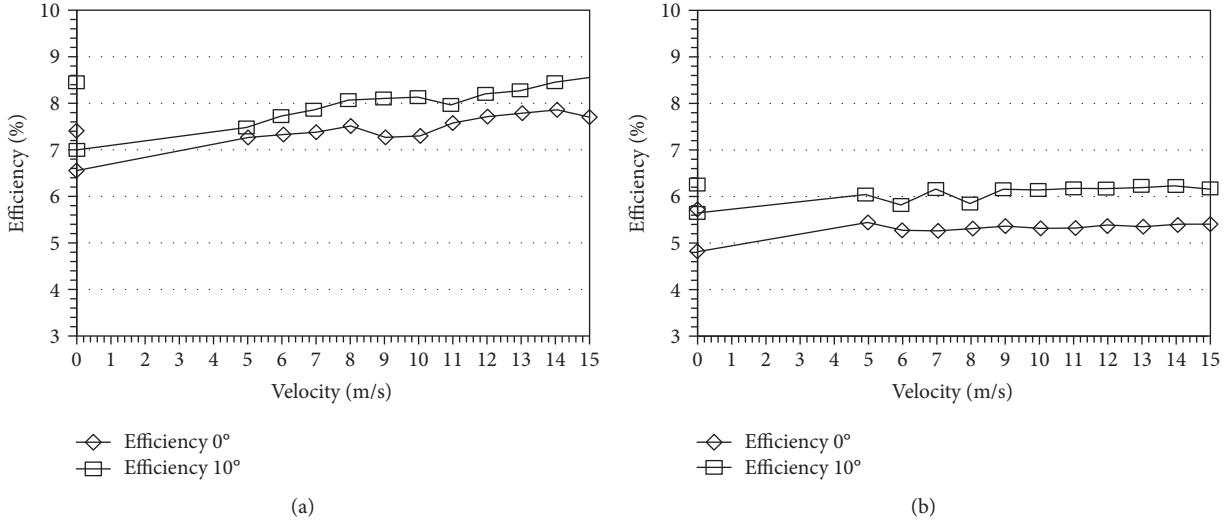


FIGURE 8: Modules efficiency at different velocities. (a) Monocrystalline and (b) polycrystalline.

angle of 0° with the airflow, it was found that the efficiency of monocrystalline module increases from 10 to 15% while for polycrystalline module the increase was from 5 to 10%. In case of tilt angle of 10° with the incoming airflow, increase in performance parameters for both modules are found to be 11 to 18% and 8 to 12%, respectively.

Nomenclature

- A: Active area of cells [m^2]
- C-Si: Monocrystalline silicon module
- h : convective heat transfer coefficient [$\text{W}/\text{m}^2\text{K}$]
- I: Current [A]
- I_{rr} : Solar irradiance [W/m^2]
- L: Length of panel [m]
- P-Si: Polycrystalline silicon module
- P: Power [W]
- Q: Heat flux [W/m^2]

STC: Standard testing condition

T: Temperature [$^\circ\text{C}$]

E: Voltage [V]

Re: Reynolds number

Pr: Prandtl number

U: Velocity along x -axis [m/s]

V: Velocity along y -axis [m/s]

n_s : Normal unit direction vector

q_w : Specified heat flux

D: Characteristic length

K: Thermal conductivity.

Greek Symbols

- μ : Dynamic viscosity [$\text{kg}\cdot\text{m}^{-1}\cdot\text{s}^{-1}$]
- η_m : Module efficiency (%)
- θ : Nondimensional temperature
- ρ : Density [kg/m^3].

Subscripts

- a: Air
- Max: maximum
- Mea: Measured
- sc: Short circuit
- s: Surface of module
- oc: Open circuit.

Conflicts of Interest

The authors declare that they have no conflicts of interest.

Acknowledgments

This work was supported by Mechanical Engineering Department of University of Engineering and Technology Taxila, Pakistan, which is gratefully acknowledged.

References

- [1] N. Stephen, "Trends in photovoltaic applications," in *International Energy Agency Report*, IEA-PVPS T1-23, 2013.
- [2] N. S. Sariciftci, *Organic Photovoltaics Mechanisms Materials and Devices*, CRC Press, Boca Raton, 2005.
- [3] R. H. Bube, *Photovoltaic Materials*, Imperial College Press, London, 1998.
- [4] R. J. Kaplar, D. Kwon, S. A. Ringel et al., "Deep levels in p-and n-type In Ga As N for high-efficiency multi-junction III-V solar cells," *Solar Energy Materials and Solar Cells*, vol. 69, no. 1, pp. 85–91, 2001.
- [5] T. Trupke, M. A. Green, and P. Würfel, "Improving solar cell efficiencies by down-conversion of high energy photons," *Journal of Applied Physics*, vol. 92, no. 3, pp. 1668–1674, 2002.
- [6] R. D. Schaller and V. I. Klimov, "High efficiency carrier multiplication in PbSe nanocrystals: implications for solar energy conversion," *Journal of Applied Physics*, vol. 92, no. 18, article 186601, 2004.
- [7] R. T. Ross and A. J. Nozik, "Efficiency of hot-carrier solar-energy converters," *Journal of Applied Physics*, vol. 53, pp. 3813–3818, 1982.
- [8] D. Vincenzi, A. Busato, M. Stefancich, and G. Martinelli, "Concentrating PV system based on spectral separation of solar radiation," *Physica Status Solidi (a)*, vol. 206, no. 2, pp. 375–378, 2009.
- [9] J. Palm, V. Probst, and F. H. Karg, "Second generation CIS solar modules," *Solar Energy*, vol. 77, no. 6, pp. 757–765, 2004.
- [10] M. Fuentes, G. Nofuentes, J. Aguilera, D. L. Talavera, and M. Castro, "Application and validation of algebraic methods to predict the behavior of crystalline silicon PV modules in Mediterranean climates," *Solar Energy*, vol. 81, no. 11, pp. 1396–1408, 2007.
- [11] R. Levy, "Solar energy conversion can be small-scale and low-tech," *Physics Today*, vol. 60, pp. 12–14, 2007.
- [12] W. Shockley and H. J. Queisser, "Detailed balance limit of efficiency of P-N junction solar cells," *Journal of Applied Physics*, vol. 32, no. 3, pp. 510–519, 1961.
- [13] P. Singh and N. M. Ravindra, "Temperature dependence of solar cell performance—an analysis," *Solar Energy Materials and Solar Cells*, vol. 101, pp. 36–45, 2012.
- [14] A. Q. Malik and M. F. Haji Metali, "Performance of single crystal silicon photovoltaic module in Bruneian climate," *International Journal of Applied Science and Engineering*, vol. 8, pp. 179–188, 2010.
- [15] H. G. Teo, P. S. Lee, and M. N. Hawlader, "An active cooling system for photovoltaic modules," *Applied Energy*, vol. 90, no. 1, pp. 309–315, 2012.
- [16] S. Mekhilef, R. Saidur, and M. Kamalifarvestani, "Effect of dust, humidity and air velocity on efficiency of photovoltaic cells," *Renewable and Sustainable Energy Reviews*, vol. 16, pp. 2920–2925, 2012.
- [17] A. Muzaffar, "Performance enhancement of PV cells through micro channel cooling," in *WEENTECH Proceedings in Energy: Global Conference on Energy and Sustainable Development*. Coventry: World Energy and Environment Technology Ltd., pp. 211–217, 2015.
- [18] Satori. E, "Convection coefficient equations for forced air flow over flat surfaces," *Solar Energy*, vol. 80, no. 9, pp. 1063–1071, 2006.
- [19] A. Yunus, *Heat Transfer, A practical approach*, p. 372, 2nd edition, 2002.

Research Article

The Design and Optimization of GaAs Single Solar Cells Using the Genetic Algorithm and Silvaco ATLAS

Kamal Attari, Lahcen Amhaimar, Ali El yaakoubi, Adel Asselman, and Mounir Bassou

Optics & Photonics Team, Faculty of Science, Abdelmalek Essaadi University, Tetuan, Morocco

Correspondence should be addressed to Kamal Attari; attari.kamal@gmail.com

Received 10 May 2017; Revised 6 August 2017; Accepted 29 August 2017; Published 12 November 2017

Academic Editor: Srinivas Devayajanam

Copyright © 2017 Kamal Attari et al. This is an open access article distributed under the Creative Commons Attribution License, which permits unrestricted use, distribution, and reproduction in any medium, provided the original work is properly cited.

Single-junction solar cells are the most available in the market and the most simple in terms of the realization and fabrication comparing to the other solar devices. However, these single-junction solar cells need more development and optimization for higher conversion efficiency. In addition to the doping densities and compromises between different layers and their best thickness value, the choice of the materials is also an important factor on improving the efficiency. In this paper, an efficient single-junction solar cell model of GaAs is presented and optimized. In the first step, an initial model was simulated and then the results were processed by an algorithm code. In this work, the proposed optimization method is a genetic search algorithm implemented in Matlab receiving ATLAS data to generate an optimum output power solar cell. Other performance parameters such as photogeneration rates, external quantum efficiency (EQE), and internal quantum efficiency (EQI) are also obtained. The simulation shows that the proposed method provides significant conversion efficiency improvement of 29.7% under AM1.5G illumination. The other results were $J_{sc} = 34.79 \text{ mA/cm}^2$, $V_{oc} = 1 \text{ V}$, and fill factor (FF) = 85%.

1. Introduction

Direct band gap materials prove that the use of an optimum configuration leads to a highly functional single- or multiple junction solar cells. The interest in GaAs solar cells has become more popular in the recent years due to its band gap (1.42 ev) close to the standard spectrum [1]. However, its major problem was the surface recombination rate that has been reducing the GaAs solar cells improvement's start with 10% [2]. This problem was solved by means of using a $\text{Ga}_{1-x}\text{Al}_x$ on the surface of GaAs [3]. Using GaAs junction only is not enough to get higher efficient solar cells. In fact, the improvement of its performance will surely be accomplished by adding other material layers on the top and bottom of the junction. For instance, a wider band gap material such as AlGaAs used as a back surface field (BSF) makes a significant improvement [4, 5]. Also under the same cell configuration, the use of $\text{In}_{0.5}(\text{Al}_{0.7}\text{Ga}_{0.3})_{0.5}\text{P}$ material increases the efficiency by 6% compared to other materials thanks to its high photogeneration rate material [6]. The GaAs solar cell has greater electron saturation velocity and higher electron mobility compared with silicon solar cells [1].

This solar cell has achieved an accurate success of around 20–25% [7]. Recently, the single solar cells performance made a significant growth, an efficiency of 27% was recorded for the GaAs single cells [8]. A detailed set of simulated material parameters used in our design has been taken from previous publication [9–11]. The purpose of this work is to design a single solar cell based on GaAs that is highly efficient and to investigate its performance. Moreover, an optimization technique has been performed and proposed. A presentation and comparison of obtained results to similar solar devices from recent publication have been done. This work is organized as follows: an introduction of the model solar cell is taking place in Section 2. Section 3 explains the genetic algorithm of solar cells. The ATLAS simulation and the method of the proposed results are elaborated in Section 4. The last section concludes the whole work.

2. Solar Cell Modeling

In order to model a high efficiency single solar cell, it is important to start with similar cells of well-known characteristics and obtained performances to verify the accuracy of our

TABLE 1: Standard parameters used in this solar cell design.

Material	GaAs	InAlGaP	AlGaAs
Band gap Eg (eV) at 300 K	1.42	2.3	1.8
Lattice constant α (\AA)	5.65	5.65	5.64
Permittivity (es/eo)	13.1	11.7	11.0
Affinity (eV)	4.07	4.2	4.1
Heavy e- effective mass (m_e^*/m_0)	0.06	2.85	2.4
Heavy h+ effective mass (m_h^*/m_0)	0.5	0.64	0.62
e- mobility MUN ($\text{cm}^2/\text{V} \times \text{s}$)	8800	2150	2000
h+ mobility MUP ($\text{cm}^2/\text{V} \times \text{s}$)	400	141	138
e- density of states NC (cm^{-3})	$4.7E + 17$	$1.20E + 20$	$4.35E + 17$
h+ density of states NV (cm^{-3})	$7.0E + 18$	$1.28E + 19$	$8.16E + 18$
Lifetime (el) (s)	$1.00E - 09$	$1.00E - 09$	$1.00E - 09$
Lifetime (ho) (s)	$2.00E - 08$	$1.00E - 09$	$2.00E - 08$

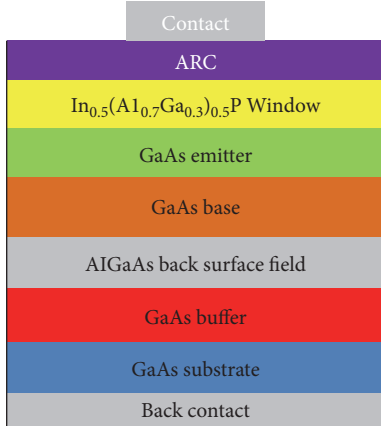


FIGURE 1: Schematic diagram of single solar cell structure used in the initial design.

model. Based on their various advantages such as absorbing a higher quantity of light, several materials were chosen and detailed in Table 1. The objective of this work was at first to construct a solar cell and then improve its efficiency. For a first step using TCAD Silvaco software, an ATLAS code was then prepared to build this structure made up of a gold contact placed at the top of the structure, and then under that was the Si₃N₄ anti-reflective coating (ARC) then the InAlGaP window layer, under that was the *n*-type GaAs emitter, then a *p*-type GaAs base, AlGaAs back surface field (BSF), GaAs buffer, GaAs substrate, and finally a gold contact in the bottom of the cell. A schematic of this model is designed in Figure 1. The solar cell was illuminated by a spectral illumination source of AM1.5G as shown in Figure 2. ATLAS solves Poisson's equation; carrier continuity equations for both electrons and holes were solved, the drift-diffusion transport model. Refractive index of each material and important parameters for the simulation of solar cells are obtained from [9, 10, 12] and from the Sopra database

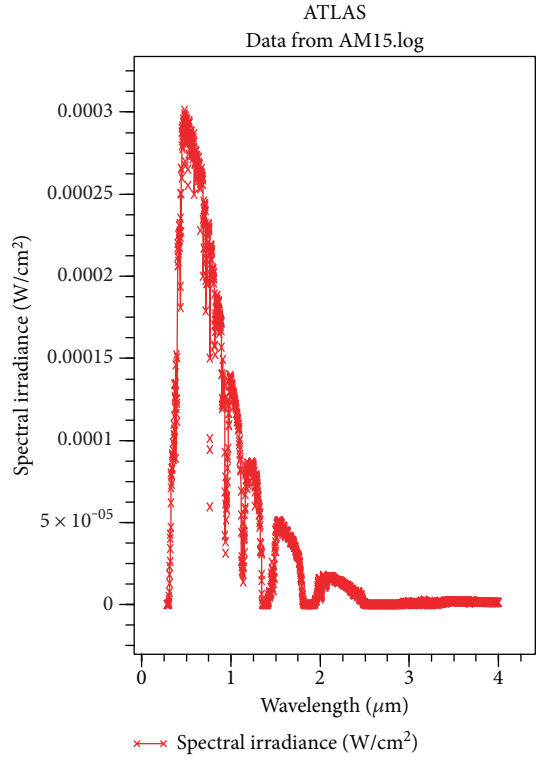


FIGURE 2: Solar spectrum AM1.5G.

incorporated in Silvaco. Different physics models were used to calculate recombination and carrier mobility for a solar cell structure. The Shockley-Read-Hall (SRH) recombination models and the concentration-dependent low-field-mobility model (CONMOB) are used to model the doping-dependent low-field mobilities of electrons and holes. To consider bulk and interface recombination velocities, (Auger) models are also utilized.

To determine the solar cell efficiency, it is important to use the following parameters: the open-circuit voltage (V_{oc}),

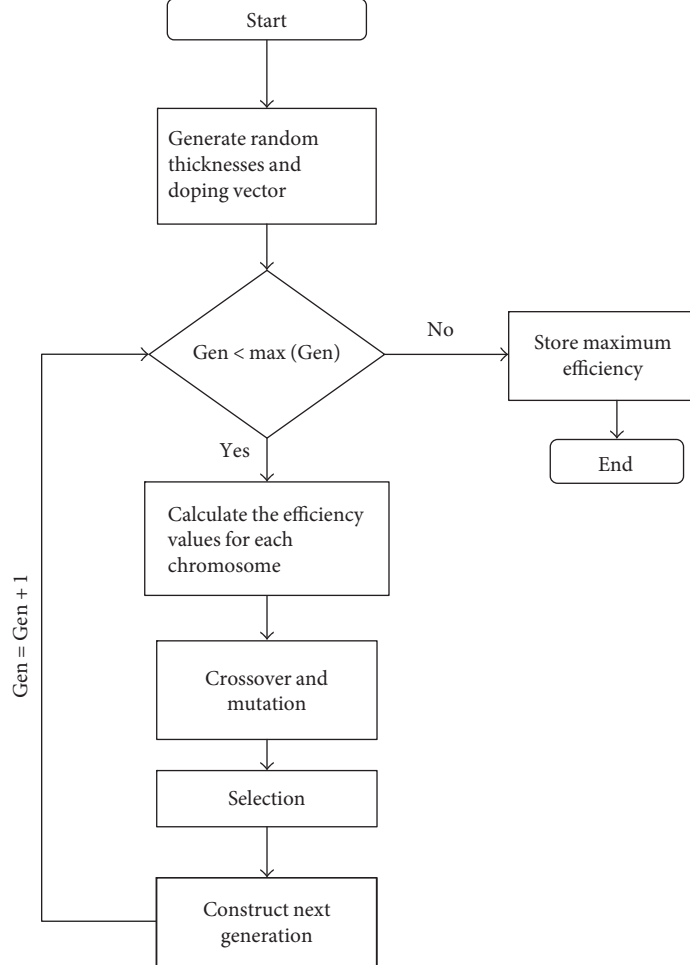


FIGURE 3: Flowchart of genetic algorithm.

short-circuit current (I_{sc}), and fill factor (FF) in the ATLAS design code.

$$I = I_0 \left[\exp\left(\frac{qV}{nkT}\right) - 1 \right] - I_L, \quad (1)$$

where I_L = light generated current.

$$V_{oc} = \left(\frac{nKT}{q} \right) \times \ln\left(\frac{I_L}{I_0}\right) + 1. \quad (2)$$

The short-circuit current (J_{sc}) is the maximum current available from a solar cell, and this occurs at zero voltage.

The expression for the FF can be determined empirically as [9]

$$FF = V_{oc} - \ln\left(\frac{V_{oc} + 0.72}{V_{oc} + 1}\right). \quad (3)$$

The maximum power is converted solar energy (solar spectrum) to electricity and can be calculated as follows:

$$P_{max} = V_{oc} \times J_{sc} \times FF. \quad (4)$$

Based on the above parameters, we can get the efficiency of a solar cell calculated as

$$\eta = \left(\frac{V_{oc} \times I_{sc} \times FF}{P_{in}} \right), \quad (5)$$

where P_{in} is the input power.

$$G = \eta_0 \times \left(\frac{p\lambda}{hc} \right) \times \alpha \exp(-\alpha y), \quad (6)$$

with G as the photogeneration rate; P is the cumulative effects of reflections, transmissions, and loss due to absorption over the ray path; y is the relative distance for the given ray; h is Planck's constant; λ is the wavelength; c is the speed of light; and α is the absorption coefficient calculated for each set of (n, k) value. η_0 is the internal quantum efficiency, which represents the number of carrier pairs generated per photon pairs.

3. Proposed Algorithm for Efficiency Optimization

The genetic algorithm (GA) is generally an optimization method that allows to obtain helpful solutions to complex problems [13]. The GA has a small computing time and good convergence that makes it a powerful optimization tool. In many published classical techniques, a variable layer (thickness or doping intensity) varies by affecting random values until achieving a higher efficiency, then move to the next variable and perform the same operation. However, in our method, all variables are tested simultaneously and result to an ideal junction configuration to produce higher efficiency. A random selected binary 8 bit strings constitute the initial generation of chromosomes. The Silvaco code is called by the GA in order to get the needed data that is encoded and then exposed to some evolution mechanisms like crossover and mutation then used as chromosomes to build the next generation. In a second step, these values are decoded then written into Silvaco ATLAS code to construct the new solar cells with the new configuration. After the simulation of all chromosome generations, child chromosomes were created from the best performing parent chromosomes. The junction layer optimization process includes the window, emitter, base, BSF, buffer, and substrate layers and determines the best thickness and doping of each layer. The flowchart of GA used for optimizing the efficiency is shown in Figure 3.

4. Results and Discussion

In this section, two steps are performed, the first one is an initial single-structure solar cell designed and simulated using Silvaco ATLAS as shown in Figure 1. The second step consists of using the GA technique to compare the cell performance parameters with an optimized solar cell.

In the first ATLAS simulation, the layer configuration were adjusted as follows: the window thickness was 400 nm, the emitter thickness was 200 nm, the base thickness was 2 μ m, the BSF thickness was 400 nm, the buffer was 100 nm, and the doping concentrations for these layers are 7×10^{17} , for the emitter 2×10^{18} , the base 4×10^{18} , the BSF 5×10^{18} , and the buffer 4×10^{18} . The obtained results were extracted from the *I-V* curve characteristics for the model as shown in Figure 4. The open-circuit voltage (V_{oc}), short-circuit current (I_{sc}), fill factor (FF), and the efficiency of this initial simulation were found, respectively: $V_{oc} = 1.08$ V, $I_{sc} = 22.88$ mA, FF = 84, and $\eta = 21\%$. A maximum power can be observed in Figure 5 with a value of 21 mW/cm². Table 2 summarizes the different thicknesses and doping concentrations for the initial model.

The next results exposed the optimization process. The simulation was done after several data exchange, between the genetic algorithm and the Silvaco ATLAS code in addition to data evaluation and generation optimization. In the end of simulation, a higher conversion of a 29.7% efficiency was recorded after a small-time computation, compared to the initial structure which has an efficiency of 21%, and new layers configuration were set to construct a new optimized GaAs single solar cells as shown in

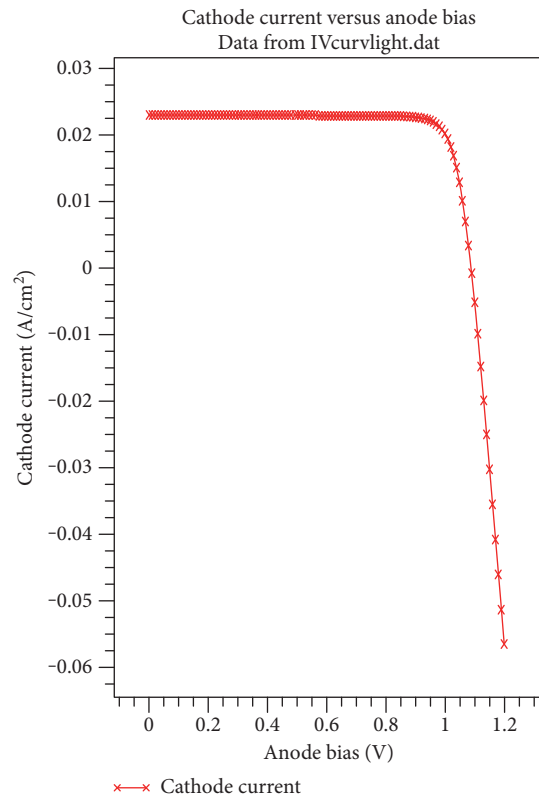


FIGURE 4: *I-V* characteristics of the initial model.

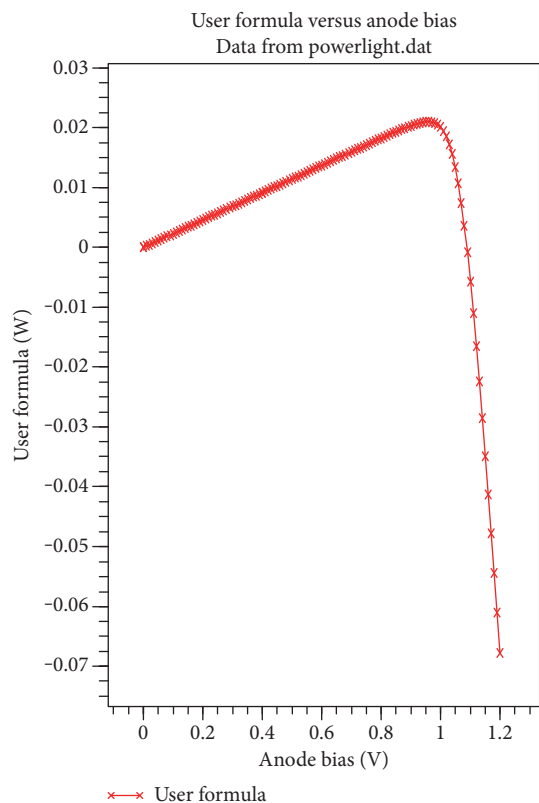


FIGURE 5: Power curve of the model of the initial solar cells.

TABLE 2: Doping and thicknesses of the initial structure.

Origin model solar cell		Doping (cm^{-3})	Thickness (μm)
ARC	Si_3N_4	—	—
<i>n</i> -layer	$\text{In}_{0.5}(\text{Al}_{0.7}\text{Ga}_{0.3})_{0.5}\text{P}$	$7e+017$	0.04
<i>n</i> -layer	GaAs	$2e+018$	0.2
<i>p</i> -layer	GaAs	$4e+018$	2
<i>p</i> -layer	AlGaAs	$5e+018$	0.4
<i>p</i> -layer	GaAs	$4e+018$	0.02

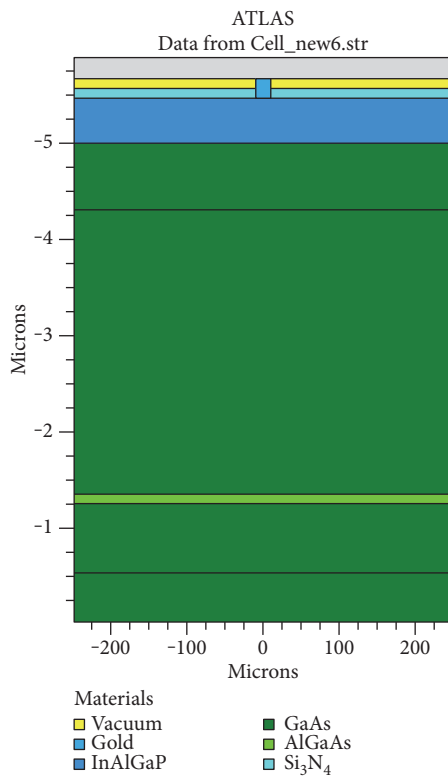


FIGURE 6: Final GaAs optimized structure.

Figure 6 enabling to produce a higher maximum power, its value achieved 29 mW/cm^2 as can be seen in Figure 7 under the AM1.5G illumination. The simulation parameters are also documented in Table 3. The optimized performances parameters, comprising the J_{sc} , V_{oc} , FF, I_{max} , V_{max} , and P_{max} , were found from the results of the GA and their values are listed in Table 4.

Figures 8 and 9 demonstrate the I - V curve of the optimized single-junction structure using the Silvaco and the genetic algorithms, although reached-optimized cell output parameters are listed in Table 4. Moreover, a comparison between the optimized and the initial solar cells can be observed in Figure 10, as well as results comparison with corresponding theoretical and experimental results for similar studies. Our GA-proposed simulation gives good result with high-efficient performance than others introduced in various previous studies as discussed elsewhere [14–17]. Differences

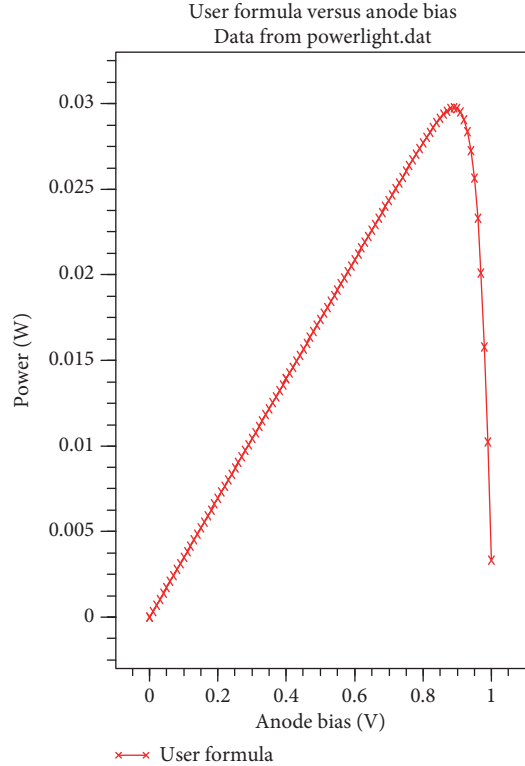


FIGURE 7: Power curve of the optimized solar cell.

TABLE 3: GA simulation parameters.

Parameters	Values
Number of generations	$G = 5$
Population	$P = 5$
Crossover rate	$\text{CR} = 1.0$
Mutation rate	$\text{MR} = 0.05$

TABLE 4: Output power improvement.

Parameters	Original single solar cell	Optimized single solar cell
Short-circuit current (I_{sc}) (mA)	22.88	34.79
Open-circuit voltage (V_{oc}) (V)	1.08	1
Max current (I_{mp}) (mA)	21.87	33.42
Max voltage (V_{mp}) (V)	0.96	0.89
Fill Factor FF (%)	84	85
Maximum power (P_{max}) (W/cm^2)	0.021	0.029
Efficiency (%)	21	29.7

are due to the variations in the material, optical parameters used, and optimization performance method presented in this work. Table 5 shows the various comparisons of this optimized structure with other previous publications; GaAs

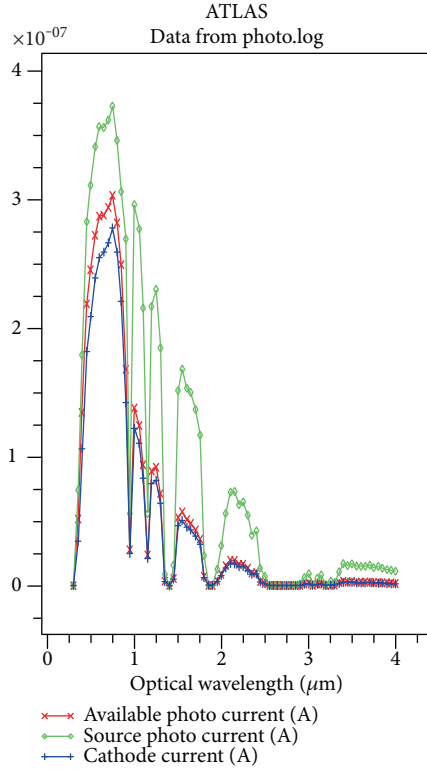


FIGURE 8: Generation of photocurrent by GaAs cell.

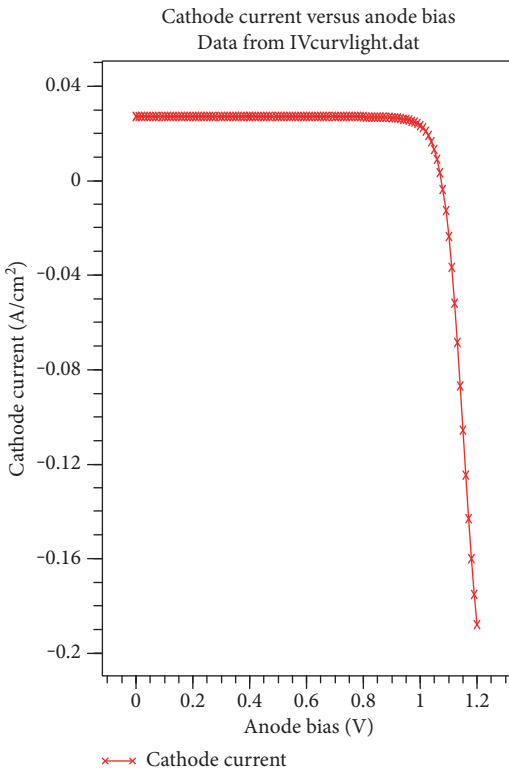


FIGURE 9: I-V characteristics of the optimized solar cell.

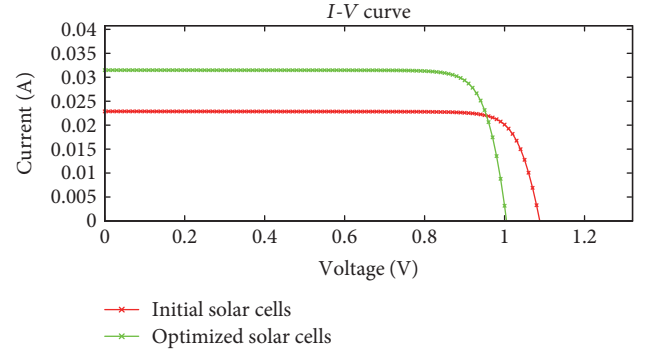


FIGURE 10: Comparison between the original and optimized I-V characteristic solar cells.

TABLE 5: Comparison between our optimized GaAs solar cell and others cells from publications.

Publications	J_{sc} (mA/cm ²)	V_{oc} (V)	FF	η (%)
Vandamme et al. [14]	19.4	0.865	0.77	12.9
Yang et al. [15]	24.5	1.0	0.78	19.1
Kayes et al. [16]	29.7	1.122	0.87	28.8
Lee et al. [17]	22.0	0.942	0.78	16.2
Moon et al. [18]	27.06	0.98	0.83	22.08
This work (initial structure)	22.88	1.08	0.84	21
This work (optimized solar cell)	34.79	1.0	0.85	29.75

solar cell achieves the highest efficiency as can be seen through the values $J_{sc} = 34.79 \text{ mA/cm}^2$, $V_{oc} = 1 \text{ V}$, and FF = 85%. Also, the close efficiency to our solar cell achieved 28.8% as can be seen in Table 5 by Kayes et al. [16]. Figure 8 shows the spectral response of the optimized solar cells. Figure 11 shows that the solar cell absorbs wavelength between 400 and 900 nm. The overall efficiency of the optimized GaAs solar cell is shown in Figure 12 which is higher at 685 nm compared to 200 nm in the initial structure shown in Figure 1 for the emitter thickness and $2.95 \mu\text{m}$ compared to $2 \mu\text{m}$ for the base thickness in the same figures.

5. Conclusion

In this paper, a single GaAs solar cell was designed and optimized in two phases; the first was by building a structure with new layers like the buffer and the BSF that can significantly improve the performance due to higher collection of photo-generation minority carriers. We have proposed a new structure configuration based on GaAs that can achieve significant efficiency. Also in this work, a GA is applied and combined with the ATLAS code to increase our designed cell output power efficiency. The simulations shows that the efficiency improvement performance of the proposed GA is better than the initial proposed structure, and as result, an optimization of more than 8% is reached and new layer configuration is obtained as shown in Figure 12; in addition, it was compared

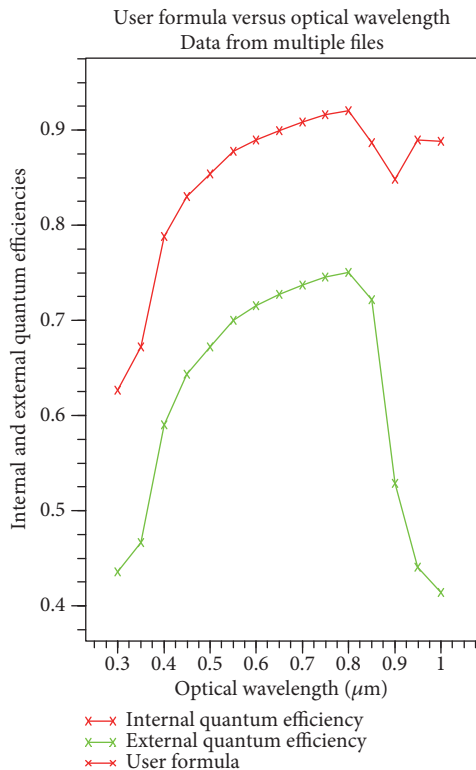


FIGURE 11: EQE and IQE of the optimized solar cells.

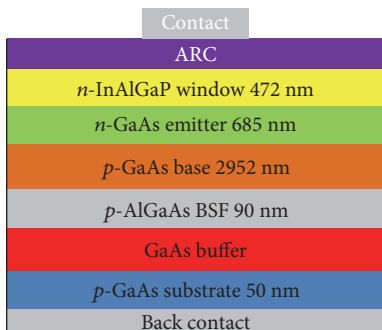


FIGURE 12: Schematic diagram of the optimized single solar cell structure.

to other single solar cells from previous publications. Its performance characteristics were $J_{sc} = 34.79 \text{ mA/cm}^2$, $V_{oc} = 1.0 \text{ V}$, $FF = 85\%$, and $\eta = 29.75\%$.

Conflicts of Interest

The authors declare that they have no conflicts of interest.

Acknowledgments

The authors acknowledge Mr. Karim Talhi for his help.

References

- [1] J. Nelson, *The Physics of Solar Cells*, Imperial College Press, London, 2003.
- [2] S. C. Tsaur, "Theoretical and experimental results for GaAs solar cells," in *Proceedings of the Fourth International Symposium on GaAs and related compounds, conference series no. 17*, 1972.
- [3] J. J. Liou and W. W. Wong, "Comparison and optimization of the performance of Si and GaAs solar cells," *Solar Energy Materials and Solar Cells*, vol. 28, pp. 9–28, 1992.
- [4] D. J. Aiken, "Antireflection coating design for series interconnected multi-junction solar cells," *Progress in Photovoltaics: Research and Applications*, vol. 8, p. 563, 2000.
- [5] B. Galiana, I. ReyStolle, M. Baudrit, I. Garcia, and C. Algara, "A comparative study of BSF layers for GaAs-based single-junction or multijunction concentrator solar cells," *Semiconductor Science and Technology*, vol. 21, pp. 1387–1393, 2006.
- [6] K. J. Singha and S. K. Sarkar, "A wide band gap In0.5(Al0.7Ga0.3)0.5P back surface field layer increases 6% more efficiency in DLAR dual junction InGaP solar cell," in *2016 International Conference on Energy Efficient Technologies for Sustainability (ICEETS)*, Nagercoil, India, 2016.
- [7] K. Barnham, J. Barnes, G. Haarpainter et al., "Quantum-well solar cells," *Materials Research Society Bulletin*, vol. 18, pp. 51–55, 1993.
- [8] A. Talhi, A. Belghachi, H. Moughli, B. Amiri, and L. Varani, "Numerical simulation of multi-quantum solar cells GaAs/InAs using Silvaco Atlas," *Digest Journal of Nanomaterials and Biostructures*, vol. 11, pp. 1361–1366, 2016.
- [9] K. J. Singh and S. K. Sarkar, "Highly efficient ARC less InGaP/GaAs DJ solar cell numerical modeling using optimized InAl-GaP BSF layers," *Optical and Quantum Electronics*, vol. 43, pp. 1–21, 2012.
- [10] SILVACO Data Systems Inc, *Silvaco ATLAS User's Manual*, 2015.
- [11] I. Vurgaftman, J. R. Meyer, and L. R. Ram-Mohan, "Band parameters for III-V compound semiconductors and their alloys," *Journal of Applied Physics*, vol. 89, no. 11, pp. 5815–5875, 2001.
- [12] D. E. Aspnes, S. M. Kelso, R. A. Logan, and R. Bhat, "Optical properties of AlxGa1-xAs," *Journal of Applied Physics*, vol. 60, no. 2, pp. 754–767, 1986.
- [13] C. Guo, "A programming of genetic algorithm in Matlab7.0," *Modern Applied Science*, vol. 5, pp. 230–235, 2011.
- [14] N. Vandamme, H. L. Chen, A. Gaucher et al., "Ultrathin GaAs solar cells with a silver back mirror," *IEEE Journal of Photovoltaics*, vol. 5, pp. 565–570, 2015.
- [15] W. Yang, J. Becker, S. Liu et al., "Ultra-thin GaAs single junction solar cells integrated with a reflective back scattering layer," *Journal of Applied Physics*, vol. 115, article 203105, 2014.
- [16] B. M. Kayes, N. Hui, R. Twist et al., "27.6% conversion efficiency, a new record for single-junction solar cells under 1 sun illumination," in *2011 37th IEEE Photovoltaic Specialists Conference*, pp. 000004–000008, Seattle, WA, USA, 2011.
- [17] S. M. Lee, A. Kwong, D. Jung et al., "High performance ultrathin GaAs solar cells enabled with heterogeneously integrated dielectric periodic nanostructures," *ACS Nano*, vol. 9, pp. 10356–10365, 2015.
- [18] S. Moon, K. Kim, Y. Kim, J. Heo, and J. Lee, "Highly efficient single-junction GaAs thin-film solar cell on flexible substrate," *Scientific Reports*, vol. 6, article 30107, 2016.

Research Article

Characteristics of Nanocrystallite-CdS Produced by Low-Cost Electrochemical Technique for Thin Film Photovoltaic Application: The Influence of Deposition Voltage

Obi Kingsley Echendu,^{1,2} Francis Birhanu Dejene,¹ Imyhamy Mudiy Dharmadasa,² and Francis Chukwuemeka Eze³

¹*Department of Physics, Qwa Qwa Campus, University of the Free State, X13, Phuthaditjhaba 9866, South Africa*

²*Electronic Materials and Sensors Group, Materials and Engineering Research Institute, Sheffield Hallam University, Sheffield S1 1WB, UK*

³*Department of Physics, Federal University of Technology, PMB 1526, Owerri, Nigeria*

Correspondence should be addressed to Obi Kingsley Echendu; oechendu@yahoo.com

Received 12 April 2017; Accepted 14 September 2017; Published 2 November 2017

Academic Editor: Prakash Basnyat

Copyright © 2017 Obi Kingsley Echendu et al. This is an open access article distributed under the Creative Commons Attribution License, which permits unrestricted use, distribution, and reproduction in any medium, provided the original work is properly cited.

Electrochemical deposition and characterization of nanocrystallite-CdS thin films for thin film solar cell application are reported. The two-electrode system used provides a relatively simple and cost-effective approach for large-scale deposition of semiconductors for solar cell and other optoelectronic device application. Five CdS thin films were deposited for 45 minutes each at different cathodic deposition voltages in order to study their properties. X-ray diffraction study reveals that the as-deposited films contain mixed phases of hexagonal and cubic CdS crystallites with large amounts of internal strain and dislocation density. Postdeposition annealing results in phase transformation which leaves the films with only the hexagonal crystal phase and reduced strain and dislocation density while increasing the crystallite sizes from 21.0–42.0 nm to 31.2–63.0 nm. Photoelectrochemical cell study shows that all the CdS films have n-type electrical conductivity. Optical characterization reveals that all samples show similar transmittance and absorbance responses with the transmittance slightly increasing towards higher growth voltages. All the annealed films show energy bandgap of 2.42 eV. Scanning electron microscopy and energy dispersive X-ray analyses show that grains on the surface of the films tend to get cemented together after annealing with prior CdCl₂ treatment while all the films are S-rich.

1. Introduction

CdS is a wide bandgap II–VI compound semiconductor with a direct bulk bandgap of 2.42 eV [1]. Due to its desirable properties, it finds use in photovoltaic solar cells [2, 3], piezo transducers [4], photoresistors, luminescence devices [5], Schottky diodes and metal-semiconductor field effect transistors (MESFETs) [6], heterojunction diodes [7], insulated gate thin film transistors [8], and gas sensors [9]. It is also used in microelectronics, nonlinear optics, catalysis, photoelectrochemistry [10], and in photodetectors [11]. In its application in photovoltaics, CdS has been used as an n-type heterojunction partner to CdTe, CuS, and Cu(In, Ga)Se₂ (CIGS)

absorber materials for the fabrication of CdS/CdTe, CdS/CuS, and CdS/CIGS solar cells [12–14].

Several growth techniques have been used for the deposition of CdS for various uses. These techniques include chemical bath deposition (CBD) [15], vacuum evaporation, chemical vapour deposition [16], spray pyrolysis [17], sputtering [18], screen printing [19], sol-gel [20], close space sublimation (CSS) [21], and electrodeposition (ED) [22]. As is common in most electrodeposition processes for semiconductors in the past, electrodeposition of CdS has always been reported in the literature based on the conventional three-electrode configuration [23]. Report on the use of two-electrode system for the electrodeposition of CdS is very

scarce in the literature, and one can only find two major reports to date [22, 24]. Diso et al. [22] grew their CdS materials using CdCl_2 and $\text{Na}_2\text{S}_2\text{O}_3$ as precursors but at a pH of 1.4 and temperature of 45°C for fear of precipitation. Both their reported as-deposited and heat-treated CdS films had hexagonal crystal structure without any phase transformation as a result of postdeposition heat treatment. Abdul-Manaf et al. [24] on the other hand used CdCl_2 and $(\text{NH}_4)_2\text{S}_2\text{O}_3$ as precursors but grew CdS at a pH of 2.0 and a temperature of 85°C. The as-deposited CdS materials in this case had a mixture of hexagonal CdS, cubic CdS, and orthorhombic sulphur crystal phases which transformed to purely hexagonal phase after postgrowth heat treatment. Both Diso et al. and Abdul-Manaf et al. did not report the postdeposition heat treatment with prior CdCl_2 treatment. Again, both groups did not report morphological characterization of CdS films grown at different growth voltages but only reported the morphological characterization of CdS grown at a particular voltage and annealed under different temperature conditions.

Under the low temperature (45°C) and low pH (1.4) used by Diso et al., they did not observe mixed phases of CdS. It is also noted that these temperature and pH are substantially far away from those (>80°C and ~2.00, resp.) under which CdTe is usually grown for CdS/CdTe solar cell fabrication [2, 25]. However, Abdul-Manaf et al. who grew CdS at relatively higher temperature of 85°C and pH of 2.00 reported the presence of mixed cubic and hexagonal phases of CdS with the presence of orthorhombic sulphur all in their as-deposited CdS materials. These mixed phases transformed to purely hexagonal phase after postgrowth heat treatment.

Then, in order to see whether the presence of these mixed phases is a function of growth temperature and pH or a function of the sulphur precursor, authors decided to grow CdS in the present work at a temperature of 80°C and pH of 1.80, both of which are in-between the values used by Diso et al. and Abdul-Manaf et al. These growth parameter values are still very close to those for the growth of CdTe on CdS for solar cell fabrication. We have also used $\text{Na}_2\text{S}_2\text{O}_3$ as the sulphur precursor since Abdul-Manaf et al. have observed mixed phases with $(\text{NH}_4)_2\text{S}_2\text{O}_3$ as sulphur precursor. In the present work, CdCl_2 and $\text{Na}_2\text{S}_2\text{O}_3$ have been used as precursors and the CdS materials were grown at a pH of 1.8 and temperature of 80°C.

The major reasons for the use of two-electrode system include the following: (i) to prevent any possible contamination of the deposition electrolyte by ions such as Ag^+ and K^+ which may eventually leak into the deposition electrolyte from the porous wick of the commonly used Ag/AgCl and Hg/HgCl (saturated calomel electrode (SCE)) reference electrodes during the electrodeposition process at elevated temperatures and (ii) to reduce the cost due to reference electrode, as reported in recent publications by the main author's research group [26, 27].

In the fabrication of high-efficiency solar cells using CdS as window material, the most commonly used technique for the deposition of CdS is CBD [2] while CdTe is deposited using CSS [2], sputtering [18], or electrodeposition [28]. Due to the nature of the CBD as a batch process, lots of

Cd-containing wastes are generated in the large-scale deposition of CdS for solar cell fabrication. This no doubt raises environmental concerns and costs a huge sum of money for waste management and disposal. In an industrial production line, this situation, coupled with the use of at least two different deposition techniques, presents real issues and leads to the production of expensive solar panels. It is preferable in such an industrial process to have only one production line by using only one technique to deposit both CdS and CdTe. A continuous process such as electrodeposition fits into this one production line that can be used for the production of less expensive solar panels.

One major factor in electrodeposition of semiconductors is the choice of the right deposition voltage as this, in most cases, affects the properties of the deposited materials. For example, the stoichiometry and therefore the electrical conductivity type of some compound semiconductors like CdTe are affected by the deposition voltage used [29]. It is for these reasons that the effect of deposition voltage on electrodeposited CdS thin films using two-electrode system has been studied and reported in this work. There is yet another major reason why the development of electrodeposited CdS material is important for the fabrication of all-electrodeposited solar cells employing CdS as window or buffer layer. CBD-grown CdS is usually deposited at very high pH values in the range of 9 and above [1] whereas electrodeposited CdTe is grown at low pH values in the range of 1-2 [27-29]. Experience has shown that immersing the CBD-CdS grown in alkaline environment into the acidic CdTe electrodeposition electrolyte could sometimes result in the peeling off of the CBD-CdS due to the sharp difference in pH of the deposition environments of the two materials. To solve this problem, the electrodeposition of CdS reported in the present work has been carried out at a pH of 1.8 ± 0.02 close to 2.0 ± 0.02 for CdTe deposition to bridge the pH gap between the deposition of CdS and CdTe.

2. Materials and Methods

2.1. Preparation of CdS Deposition Electrolyte. The CdS deposition electrolyte was prepared using 0.3 M $\text{CdCl}_2 \cdot \text{H}_2\text{O}$ and 0.03 M $\text{Na}_2\text{S}_2\text{O}_3 \cdot 5\text{H}_2\text{O}$ in 800 ml of de-ionised water. Both chemicals were of laboratory reagent grade and purchased from Fisher Scientific, United Kingdom. The resulting electrolyte is contained in a 1000 ml plastic beaker. The solution containing only $\text{CdCl}_2 \cdot \text{H}_2\text{O}$ was first prepared. The pH was adjusted to 1.80 ± 0.02 at room temperature using HCl and NH_4OH as the case may be. The 1000 ml plastic beaker containing this solution was put inside a 2000 ml glass beaker containing some de-ionised water. This serves as a water bath to ensure uniform heating of the solution. The entire container was placed on a hot plate with a magnetic stirrer. After stirring the $\text{CdCl}_2 \cdot \text{H}_2\text{O}$ solution moderately at 400 rotation per minute (r.p.m) for 24 hours, it was heated to a temperature of $80 \pm 2^\circ\text{C}$ and a cyclic voltammetry was carried out in two-electrode configuration using glass coated with fluorine-doped thin oxide (glass/FTO) as the working electrode (cathode) and high-purity carbon rod as the anode (counter electrode). From the resulting voltammogram, the

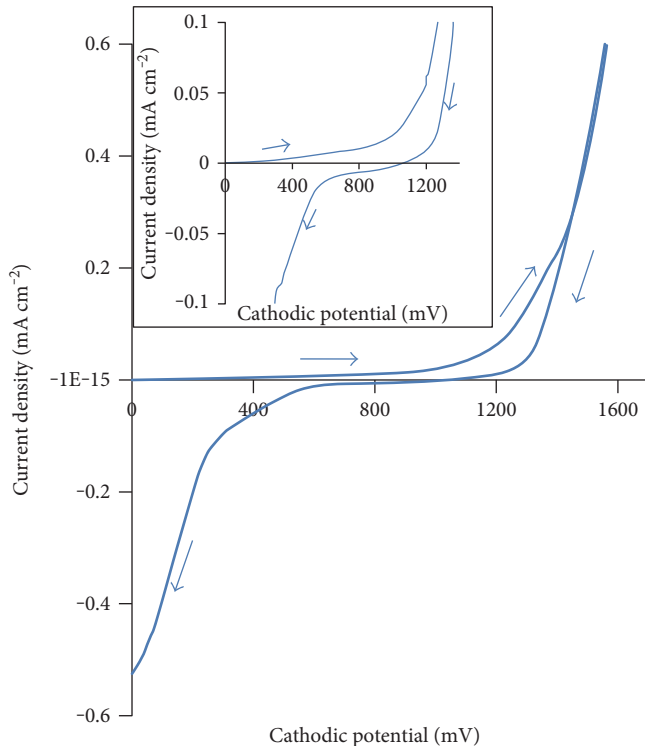


FIGURE 1: Two-electrode cyclic voltammogram of CdS deposition electrolyte containing 0.3 M CdCl₂ + 0.03 M Na₂S₂O₃ at a pH of 1.80 ± 0.02 and temperature of 80 ± 2°C. (Inset shows expansion of the potential axis for clarity.)

deposition voltage of Cd was identified. Slightly below this voltage, the CdCl₂-H₂O solution was then subjected to electro-purification for 48 hrs to remove any metallic impurities in the CdCl₂-H₂O before the addition of Na₂S₂O₃-5H₂O. The pH of the resulting electrolyte was then adjusted again to 1.80 ± 0.02 at room temperature.

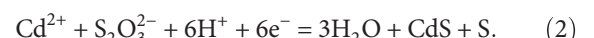
2.2. Substrate Preparation. The substrates used for the electrodeposition of CdS were glass/FTO which were prepared by cutting them into sizes of 3.0 cm × 2.0 cm × 3.0 mm followed by cleaning with soap solution in an ultrasonic bath for 15 minutes. This was also followed by cleaning with acetone and methanol using cotton buds. The substrates were then rinsed with de-ionised water and dried in a stream of N₂.

2.3. Electrodeposition of CdS. After preparing the CdS deposition electrolyte, a cyclic voltammogram of the electrolyte was recorded using a computerised Gill AC potentiostat (ACM Instruments, Cumbria, UK) in two-electrode configuration at a temperature of 80 ± 2°C with a stirring rate in the neighbourhood of 400 r.p.m using glass/FTO as the substrate. The cyclic voltammogram is shown in Figure 1.

The possible range of cathodic deposition voltages for CdS was obtained from the voltammogram to be 1300–1500 mV. Now, the reduction of S₂O₃²⁻ ions takes place earlier at a lower cathodic potential than the reduction of Cd²⁺ ions which happens at a relatively higher cathodic potential [30]. The proposed equation of reduction of S₂O₃²⁻ in the acidic solution is therefore given by



In the presence of Cd²⁺ in the solution, the overall reaction for the formation of CdS at the cathode is therefore given by



The presence of colloidal sulphur as observed in (1) and (2) turns the solution muddy with time. The rate at which this happens however depends on the concentration of the S₂O₃²⁻ in the solution. For this reason, the concentration of Na₂S₂O₃ is kept very low compared to that of CdCl₂.

Five CdS layers were deposited on glass/FTO within the above identified voltage range for 45 minutes each and at intervals of 5 mV. By controlling the stirring rate of the deposition electrolyte and gradually adding Na₂S₂O₃ to the deposition electrolyte, the deposition current density *J* was maintained at an average value of 246.6 μAcm⁻² for each sample for the duration of the deposition.

It is important to state that the thickness and uniformity of electrodeposited semiconductors are easily controlled by controlling the deposition parameters such as deposition current density, stirring rate, temperature, pH, and concentration of ions in the deposition electrolyte. Increasing the stirring rate increases the deposition current density and therefore the thickness of the deposited film. However, if the stirring rate and therefore the current density are very high, rapid deposition of the film takes place but with poor uniformity. Therefore for a uniform deposition, moderate

stirring rate and current density are desirable. From authors' experience, the stirring rate in the neighbourhood of 400 r.p.m and current density of 200–300 μAcm^{-2} for CdS produce very uniform layers. Again, increasing the deposition temperature and concentration of ions in the electrolyte increases the deposition current density and therefore the deposition rate. However, for better films with good uniformity, these parameters must be moderate. Deposition rate also varies with pH in such a way that very high and very low pH values do not produce films with good uniformity and stoichiometry. Moderate pH values are therefore necessary for good uniform films. The deposition parameters used in this work have been chosen from experience after some cycles of deposition. After deposition, each sample was divided into two equal parts. One set of the parts was designated as-deposited samples. For the other set, the samples were dipped in a saturated solution of CdCl_2 in methanol. The samples were allowed to dry in air and then annealed in air at 400°C for 20 minutes before characterising them. The reason for dipping the samples in CdCl_2 solution before annealing is to see the effect of the CdCl_2 treatment on CdS films. It can be recalled that CdCl_2 treatment is a well-known important step in the fabrication of CdTe-based solar cells, in which the treatment is usually done on CdS/CdTe stack before back metal contact fabrication. Both the as-deposited and annealed CdS samples were characterised in order to study the effect of the various selected cathodic deposition voltages on the electrical, structural, optical, morphological, and compositional properties of the electrodeposited CdS films for application in thin film solar cells.

2.4. Characterisation of the Deposited CdS Films. The selected techniques employed in this study for the electrical, structural, optical, morphological, and compositional characterisation of the electrodeposited CdS thin films, respectively, include photoelectrochemical (PEC) cell using a digital voltmeter, light source, and 0.1 M $\text{Na}_2\text{S}_2\text{O}_3$ electrolyte as reported previously [26]; X-ray diffraction (XRD) using Philips X'Pert Pro diffractometer (Philips Analytical, Almelo, The Netherlands) with Cu-K α excitation wavelength of 1.5406 Å; optical absorption using Cary 50 UV-VIS spectrophotometer (Varian Instrument, Australia); scanning electron microscopy (SEM) using FEG NOVA NANO SEM equipment (FEI company, The Netherland); and energy dispersive X-ray (EDX) using EDX detector attached to the SEM machine. The thickness T of each sample was determined using the Faraday formula [26].

$$T = \frac{MJt}{nF\rho}, \quad (3)$$

where M is the molar mass of CdS, J is the average deposition current density, t is growth time, n is the number of electrons transferred in the formation of CdS, and ρ is the density of CdS.

Since the deposition time and the deposition current density were the same for the growth of each sample, all five samples have equal thickness of about 516 nm. This is to ensure that the only variable during the deposition of the

samples is the cathodic growth voltage V_g . The crystallite sizes of the samples were estimated using the Scherer equation in (4) as reported recently in [31].

$$D = \frac{0.94\lambda}{\beta \cos \theta}, \quad (4)$$

where D is the crystallite size, λ is the wavelength of the X-ray, and β is the full width at half maximum (FWHM) of the XRD peak with which the crystallite size is calculated and θ is the corresponding Bragg angle.

The internal strain, ε , which is the distortion in the crystallites as a result of tensile or compressive stress is obtained for the films using (5) as reported in [32].

$$\varepsilon = \frac{\beta}{4 \tan \theta}. \quad (5)$$

The dislocation density, δ , which is the length of dislocation lines per unit volume of crystal in each sample, is estimated using the Williamson-Smallman relation given by (6) as reported in [33].

$$\delta = \frac{1}{D^2}. \quad (6)$$

The number of crystallites per unit area of each sample, N , was obtained using the expression in (7) as reported in [32].

$$N = \frac{t}{D^3}, \quad (7)$$

where t is the thickness of the film.

Equations (4), (5), (6), and (7) were used for the structural characterisation of the films. Optical characterisation of the samples was done using absorbance and transmittance measurements. From the graph of the square of absorbance versus photon energy, the energy bandgaps of the materials were estimated by extrapolating the straight-line portion of the graph to the photon energy axis. This is a very quick and easy way of estimating the energy bandgaps of semiconductors without actually determining the absorption coefficient and doing the Tauc plot.

3. Results and Discussion

3.1. Structural Characterisation Using X-Ray Diffraction Measurements. Figures 2(a) and 2(b) show the XRD patterns of CdS layers deposited for 45 minutes each at a temperature of $80 \pm 2^\circ\text{C}$ and at different cathodic voltages. The five layers were grown at cathodic voltages from 1445 mV to 1465 mV at 5 mV intervals. All as-deposited samples in Figure 2(a) show a characteristic polycrystalline feature with mixed hexagonal and cubic crystalline phases. There are four peaks corresponding to the hexagonal phase with (100), (002), (101), and (110) orientations and two peaks corresponding to the (111) and (200) cubic phase. The hexagonal phase peaks match the reference Joint Committee on Powder Diffractions and Standards (JCPDS) file number 01-075-1545 for hexagonal CdS while the cubic phase peaks match the reference file number 01-080-0019 for cubic CdS. In the five samples, the

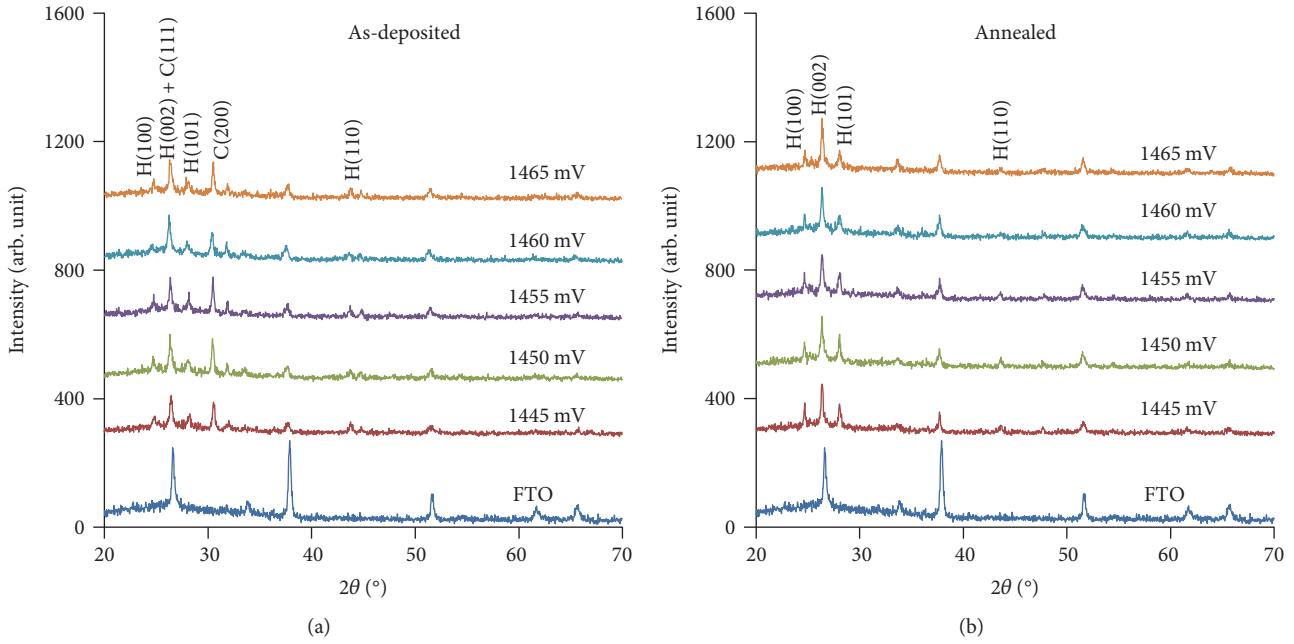


FIGURE 2: XRD patterns of (a) as-deposited and (b) annealed CdS layers deposited for 45 minutes at different cathodic growth voltages.

(100) peaks occur at 2θ values in the range 24.7–24.9°, the (002) peaks at 2θ values in the range 26.3–26.5°, the (101) peaks at 2θ values in the range 27.9–28.2°, and the (110) peaks at 2θ values in the range 43.6–43.7°. Similarly, the cubic (111) peaks occur at 2θ values in the range 26.3–26.4° and the (200) peaks occur at 2θ in the range 30.4–30.5°.

These observed mixed phases of cubic and hexagonal CdS in the as-deposited CdS materials grown at the different voltages are similar to those observed by Abdul-Manaf et al., who also observed the presence of elemental sulphur in addition. However, elemental sulphur has not been observed in our XRD results of the present work as against the observation of Abdul-Manaf et al. These results therefore suggest that the incidence of mixed phases in as-deposited CdS is not necessarily caused by the nature of sulphur precursor but rather it has to do with the growth conditions such as temperature and pH.

After CdCl_2 treatment and annealing in air at 400°C for 20 minutes, a startling observation was made. This was the disappearance of the peaks representing the cubic phase of CdS. Figure 2(b) shows the XRD patterns of the annealed CdS layers with only peaks for the hexagonal phase. Metin et al. [34] reported a similar scenario of mixed cubic and hexagonal phases in CBD-CdS in which the cubic phase disappeared after annealing. A slight narrowing of the range of 2θ values for the four hexagonal phase peaks was also observed with all the (100) peaks occurring at a 2θ value of 24.7°, all the (002) peaks occurring at a 2θ value of 26.4°, the (101) peaks occurring at 2θ range of 28.0–28.1°, and the (110) peaks occurring at 2θ range of 43.5–43.6°.

Figure 2(b) also shows that the preferred orientation of the crystallites in the hexagonal CdS phase is in the (002) crystal plane. The disappearance of the peaks corresponding to the cubic phase after annealing suggests that the cubic phase of CdS is not stable, at least, at the annealing

temperature used in this work. An estimation of the crystallite sizes of the layers was done using the Scherrer formula in (3), and the effect of annealing on them was investigated for the five samples. In doing this however, only the hexagonal phase is considered since the cubic phase is not stable on annealing. The (002) peak was considered as the preferred orientation for these samples. Although the (002) peak coincides with FTO peak, a close look at this peak in comparison with the highest FTO peak (at 2θ , ~37°) in the XRD patterns of the five samples shows that the (002) peak actually represents the preferred orientation of CdS crystallites in the layers. However, for crystallite size estimation, the (101) peaks were used for two reasons. First, the (002) peaks coincide with FTO peak which will likely introduce error in the result of the crystallite size estimation. Secondly, the (101) peaks are the next in intensity to the (002) peaks.

Tables 1 and 2 show the results of analysis of the (101) peak for as-deposited and annealed CdS layers, respectively. Using the JCPDS file number 01-075-1545 for hexagonal CdS phase ($2\theta = 28.2^{\circ}$, interplanar spacing $d = 3.1648 \text{ \AA}$ and relative intensity = 100%) for the (101) peak as a reference, Tables 1 and 2 show that all the as-deposited and annealed samples displayed a slight downward shift in the 2θ values and a slight upward shift in the d -spacing relative to the reference material.

In terms of the FWHM, all samples experienced increase in crystallite sizes after annealing, with the samples grown at 1445 mV and 1450 mV showing the highest crystallite size of 63.02 nm. However, in terms of the crystallite sizes after annealing, 1450 mV produces the highest percentage increase in crystallite size of ~200%.

The observed shift in 2θ positions and values of d -spacing from those of the standard reference material suggests that the deposited CdS films are strained. The increase in d -spacing values and decrease in 2θ values from the standard values

TABLE 1: XRD analysis of the (101) hexagonal peak for as-deposited CdS thin films grown at different cathodic voltages.

Cathodic growth voltage, V_g (mV)	Growth time, t (min)	2θ ($^{\circ}$)	FWHM, β ($^{\circ}$)	d -spacing, d (\AA)	Crystallite size, D (nm)
1445	45	28.2	0.3247	3.1658	25.22
1450	45	28.1	0.3897	3.1752	21.01
1455	45	28.1	0.3897	3.1768	21.01
1460	45	28.0	0.3897	3.1873	21.01
1465	45	28.1	0.3897	3.1704	21.01

TABLE 2: XRD analysis of the (101) hexagonal peak for annealed CdS thin films deposited at different cathodic voltages.

Cathodic growth voltage, V_g (mV)	Growth time, t (min)	2θ ($^{\circ}$)	FWHM, β ($^{\circ}$)	d -spacing, d (\AA)	Crystallite size, D (nm)
1445	45	28.0	0.1299	3.1840	63.02
1450	45	28.0	0.1299	3.1855	63.02
1455	45	28.0	0.2598	3.1818	31.51
1460	45	28.1	0.2598	3.1792	31.51
1465	45	28.1	0.2598	3.1803	31.51

TABLE 3: Evaluation of strain and dislocation density of the CdS films deposited at different cathodic voltages.

V_g (mV)	$\epsilon_1 \times 10^{-3}$	As-deposited		$\epsilon_2 \times 10^{-3}$	Annealed		Comparison		
		$\delta_1 \times 10^{11}$ (lines/cm 2)	$N_1 \times 10^{12}$ (cm $^{-2}$)		$\delta_2 \times 10^{11}$ (lines/cm 2)	$N_2 \times 10^{12}$ (cm $^{-2}$)	ϵ_1/ϵ_2	δ_1/δ_2	N_1/N_2
1445	5.64	1.57	3.2	2.68	0.25	0.2	2.10	6.28	16.0
1450	6.79	2.27	5.6	2.68	0.25	0.2	2.53	9.08	28.0
1455	6.79	2.27	5.6	4.54	1.01	1.6	1.50	2.25	3.5
1460	6.82	2.27	5.6	4.53	1.01	1.6	1.51	2.25	3.5
1465	6.79	2.27	5.6	4.53	1.01	1.6	1.50	2.25	3.5

indicate that there is inhomogeneous tensile stress on the crystallites of these films which induces strain in the crystallites. This also suggests the presence of defects such as dislocation, vacancies, or interstitials. However, for the electrodeposited CdS films under study, the influence of FWHM on the strain, dislocation density, and number of crystallites per unit area overrides those of 2θ and d -spacing. As a result, the annealed samples show reduced internal strain, dislocation density, and number of crystallites per unit area following (5), (6), and (7), as shown in Table 3, irrespective of the downward shift in 2θ and increase in d -spacing. This is a major advantage of postdeposition annealing in which case there is recrystallisation leading to release of stress and growth in crystallite size as a result of coalescence of smaller crystallites. Table 3 and Figures 3(a) and 3(b) show the results of evaluation of internal strain ϵ , dislocation density δ , and number of crystallites per unit area N for the as-deposited and annealed CdS samples.

After annealing, there is an overall reduction in the amount of strain and dislocation lines in the CdS samples as observed in Table 3 and Figures 3(a) and 3(b). The internal strain and dislocation density slightly increase towards higher growth voltage. The number of crystallites per unit

area also follows similar trend as strain and dislocation density as deposition voltage changes. The reduction in the values of N after annealing shows that the observed crystallite size growth on annealing, for most of the samples, must be as a result of recrystallisation and coalescence of small crystallites into large ones. The sample grown at cathodic voltage of 1445 mV has the least strain, dislocation density, and number of crystallites per unit area both before and after annealing followed by that grown at 1450 mV.

3.2. Electrical Characterisation Using Photoelectrochemical (PEC) Cell Study. Photoelectrochemical cell principle is based on the formation of a solid (semiconductor)/liquid (electrolyte) Schottky barrier junction when the solid is brought in intimate contact with the appropriate electrolyte [26]. If the solid (semiconductor in this case) is photoactive, electrons are promoted to the conduction band of the solid by the incident photons and electric current is produced. If the material is not photoactive, this will not happen. The difference between the voltages measured under illumination and in dark condition gives the PEC signal. Large PEC signals indicate the formation of wide or healthy depletion region in the semiconductor as a result of moderate doping. Small PEC

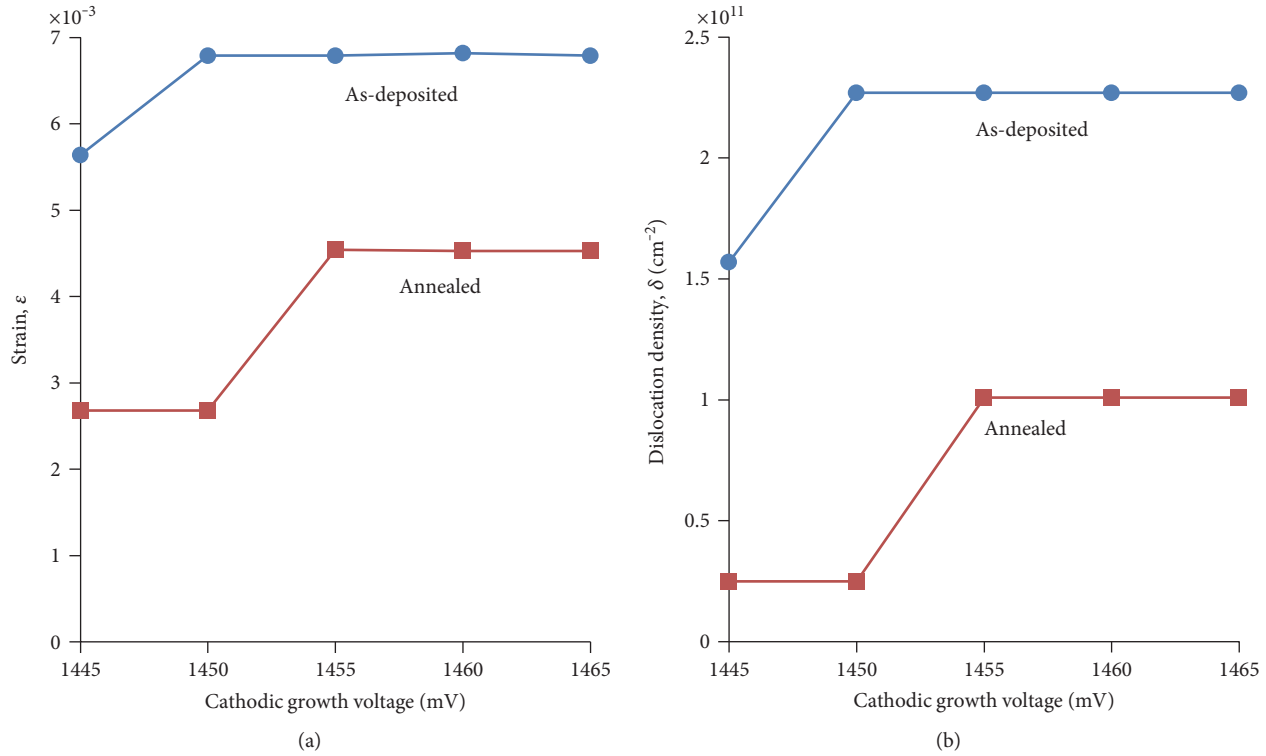


FIGURE 3: Variation of (a) internal strain and (b) dislocation density with growth voltage for the as-deposited and annealed CdS samples.

TABLE 4: PEC signals of n-type as-deposited and annealed CdS layers grown at different cathodic voltages.

V_g (mV)	PEC signal (mV) (as-deposited)	PEC signal (mV) (annealed)
1445	-158	-178
1450	-107	-120
1455	-103	-111
1460	-99	-106
1465	-97	-100

signals indicate a heavily doped semiconductor with narrow depletion region. No PEC signal at all indicates an insulator, a conductor, or an intrinsic semiconductor. In the system used in the present study, which is calibrated using well-known n-type and p-type silicon, negative PEC signal indicates an n-type semiconductor while positive PEC signal indicates a p-type semiconductor as a result of different directions of band bending in each case.

The PEC results of the electrodeposited CdS layers under study are shown in Table 4. The PEC signals of all the samples have negative values before and after annealing indicating that the samples all have n-type electrical conductivity. This result is in perfect agreement with the fact that CdS occurs naturally as an n-type semiconductor. It is a difficult task to obtain intrinsic p-type doping of CdS. However, some researchers have achieved extrinsic p-doping of CdS by mainly using Cu as a dopant [35]. Bi has also been used to achieve p-type doping in CdS through ion implantation

[36]. It is important to mention that the physical appearance of these CdS samples was dark greenish yellow in the as-deposited form which is not the colour of pure CdS. This is due to the long period of growth (45 minutes) at the growth conditions used.

However, after annealing, the samples became yellowish or orange yellow which is the right colour of CdS. The dark as-deposited samples do not show good optical properties and end up producing CdS/CdTe solar cells with very poor photovoltaic activity as a result of poor optoelectronic quality. For this reason and the fact that CdS is usually heat-treated before use in the fabrication of CdTe-based solar cell, the optical characterisation of the CdS samples under study in this work is based on the annealed samples only.

3.3. Optical Characterisation Using Spectrophotometry. Figures 4(a), 4(b), and 4(c), respectively, show the graphs of transmittance versus photon wavelength, absorbance (A) versus photon wavelength, and square of absorbance (A^2) versus photon energy for the annealed CdS samples grown at different cathodic voltages for 45 minutes. The three figures show that the five samples have similar transmittance and absorption spectra, indicating that CdS films of similar optical properties can be grown in the deposition voltage range under study. This supports the reproducibility and suitability of electrodeposition as a semiconductor growth technique.

The transmittance spectra have edges in the range 480–490 nm while the absorbance spectra have edges in the range 525–530 nm, and the different layers display approximately the same energy bandgap of ~ 2.42 eV with similar absorption

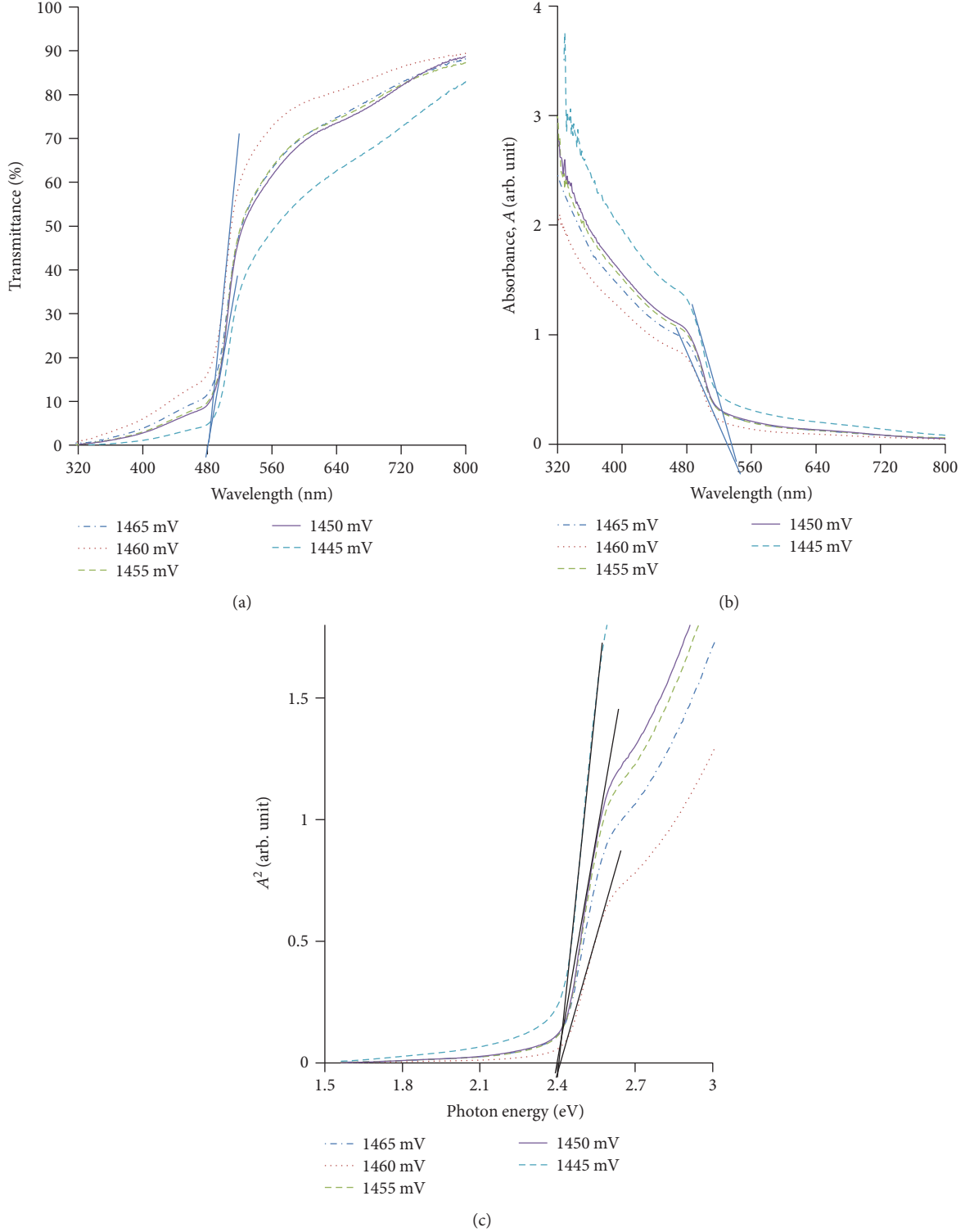


FIGURE 4: (a) Transmittance versus wavelength, (b) absorbance (A) versus wavelength, and (c) A^2 versus photon energy for annealed CdS samples grown at different cathodic voltages for 45 minutes.

edges. These results show that CdS layers of similar optical quality can be deposited in this range of growth voltage. Figure 4(a) shows that the transmittance gets slightly weaker at lower deposition voltages in the higher wavelength range. From the wavelength of 512 nm corresponding to the energy

bandgap to the wavelength of 800 nm in the near infrared, the samples have transmittance values in the range 28%–80% (for 1445 mV), 40%–88% (for 1450 mV), 45%–87% (for 1455 mV), 52%–89% for (1460 mV), and 45%–88% (for 1465 mV). The sample grown at 1460 mV has the best

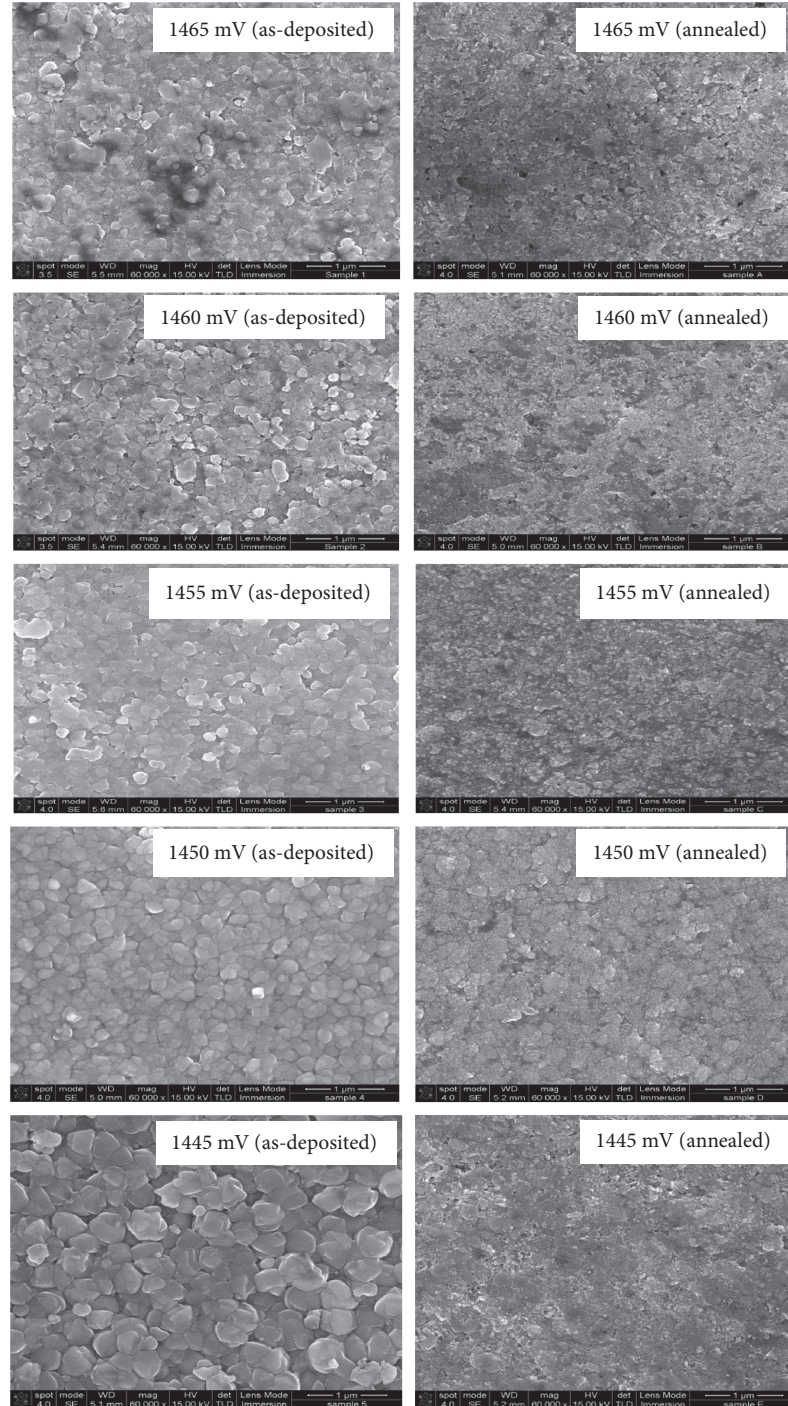


FIGURE 5: SEM images of as-deposited and annealed CdS samples grown at different cathodic voltages for 45 minutes. CdCl₂ treatment was done with saturated CdCl₂ in methanol.

transmittance while that grown at 1445 mV has the least transmittance. The absorption spectra (Figures 4(b) and 4(c)) follow an opposite trend with the 1445 mV sample showing the best absorbance and the 1460 mV sample showing the least absorbance. It is important to note that for application as window layer in solar cell fabrication, CdS with the highest possible transmittance (mostly in the visible region) is desirable.

3.4. Morphological Characterisation Using Scanning Electron Microscopy (SEM). Figure 5 shows the SEM images of as-deposited and annealed CdS samples grown for 45 minutes each at the five different cathodic voltages. The very first striking observation in the figures is the effect of postdeposition annealing (with CdCl₂ treatment) on these samples. It is important to recall that these samples were treated with saturated CdCl₂ solution in methanol before annealing at

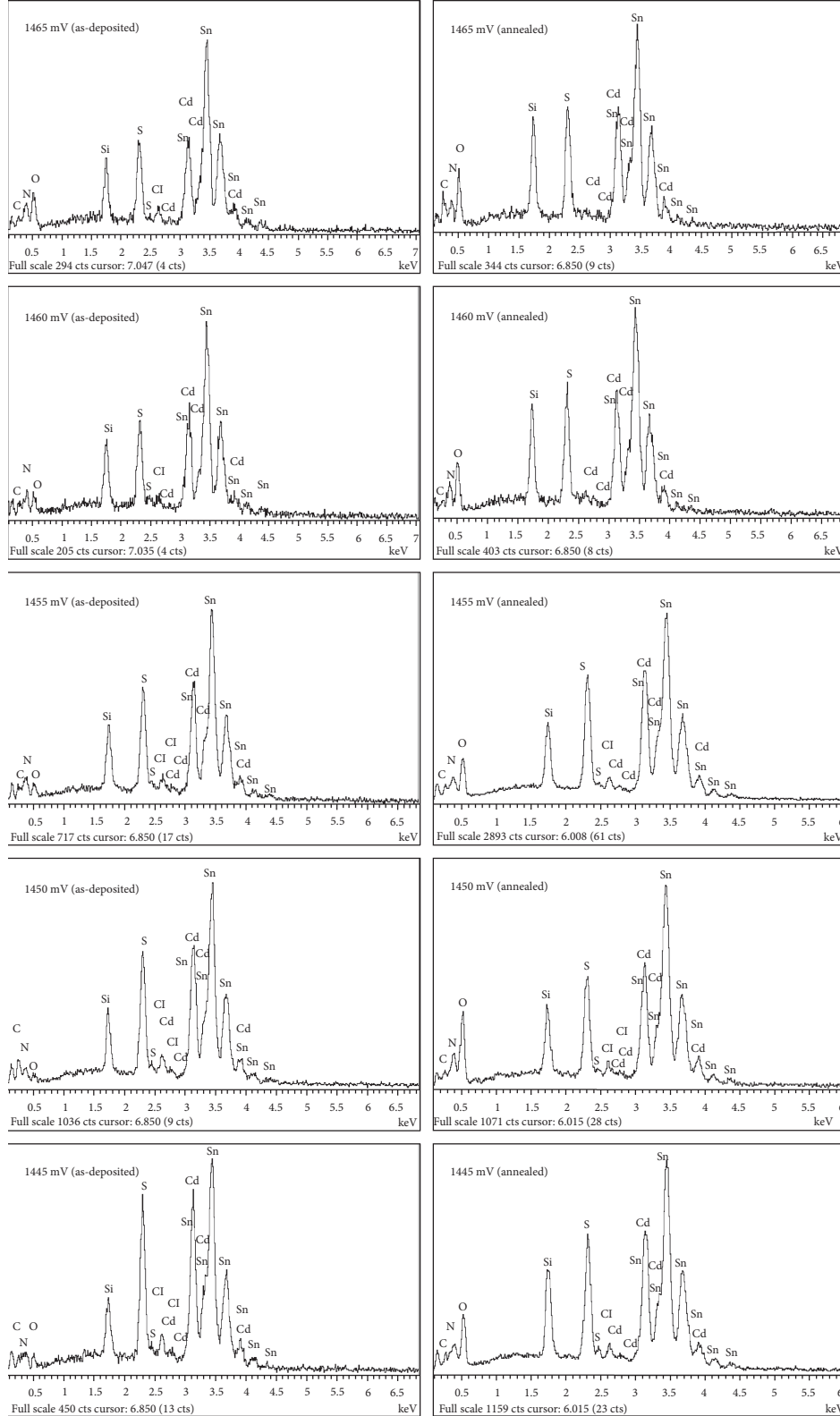


FIGURE 6: EDX spectra of as-deposited and annealed CdS samples grown at different cathodic voltages for 45 minutes. Annealing was preceded by CdCl_2 treatment.

400°C for 20 minutes in air. The “cementing” effect on the surface grains after annealing has not been observed in samples annealed without this treatment [37]. This cementing

effect on the surface grains therefore appears to be as a result of treatment with excess CdCl_2 in methanol since this effect is seen in samples grown at the different voltages explored.

TABLE 5: Percentage Cd and S atomic compositions of as-deposited and annealed CdS samples grown for 45 minutes at different cathodic voltages.

Cathodic growth voltage (mV)	Growth time (min)	Atomic composition (%)				As-deposited Cd/S	Annealed Cd/S
		As-deposited Cd	As-deposited S	Annealed Cd	Annealed S		
1445	45	46.6	53.4	46.7	53.3	0.87	0.88
1450	45	46.6	53.4	47.8	52.2	0.87	0.92
1455	45	46.6	53.4	47.8	52.2	0.87	0.92
1460	45	45.1	54.9	45.7	54.3	0.82	0.84
1465	45	42.1	57.9	44.2	55.8	0.73	0.79

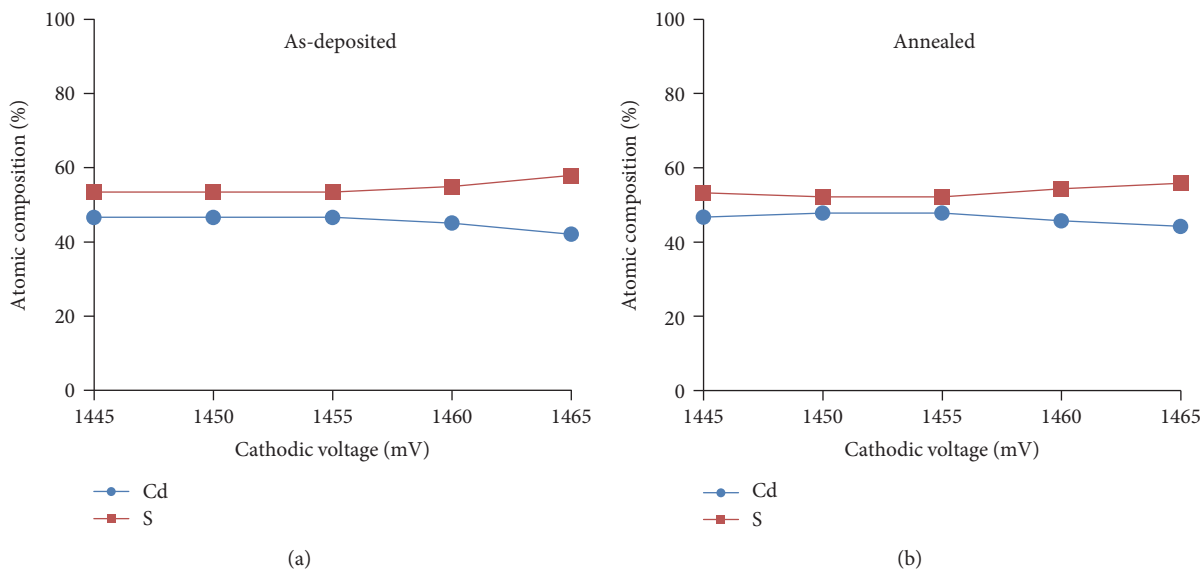


FIGURE 7: Percentage Cd and S atomic compositions of (a) as-deposited and (b) annealed CdS samples grown for 45 minutes at different cathodic voltages.

In the as-deposited samples, one notices that the grains are more clearly visible in the samples grown at lower cathodic voltages of 1445 mV and 1450 mV. As the growth voltage increases, the tendency of the grains to fuse together increases as well. This therefore makes it difficult to estimate the grain sizes of these layers from the SEM images as is also the case in the annealed sample. The observation of clear grain sizes in the samples grown at cathodic voltages of 1445 mV and 1450 mV is in agreement with the XRD analysis of the crystallites in these materials. It can be recalled that the XRD analysis of Tables 1 and 2 shows that only the samples grown at these two voltages displayed higher increase in crystallite sizes after annealing. The crystallite size after annealing according to Table 2 was 63.02 nm for both 1445 mV and 1450 mV. This is in agreement with the observed grain sizes of the as-deposited samples in Figure 5 with the sample grown at 1445 mV showing larger grains than the sample grown at 1450 mV. This surface “cementing” effect may be viewed as an advantage when these films are used in fabricating CdS/CdTe solar cells as it will tend to fill the gaps between grains in CdS. These gaps, if not covered, could act as shunting paths when CdTe is deposited

on CdS resulting in solar cells with poor open-circuit voltage and fill factor.

3.5. Compositional Characterisation Using Energy Dispersive X-Ray (EDX) Analysis. Figure 6 shows the EDX spectra of the five samples before and postdeposition annealing indicating the presence of both Cd and S atoms in these materials.

The peaks showing C, N, O, and Si must have come from the underlying glass/FTO substrate on which these CdS layers were grown. The percentage atomic concentrations of Cd and S in these samples, obtained from analysis of the EDX, are presented in Table 5 and Figure 7.

Both Table 5 and Figure 7(a) show that all the as-deposited CdS samples were S-rich. It is also observed in the as-deposited samples that the concentration of S in the layers roughly increases as the growth voltage increases while the concentration of Cd roughly decreases accordingly.

After annealing, both Table 5 and Figure 7(b) reveal all samples to be clearly S-rich at all growth voltages. A very close observation also shows that the samples become more stoichiometric after annealing with a slight increase in Cd

concentration and a corresponding decrease in S concentration. These results and others seen previously demonstrate also that the best electrodeposited CdS material from this experiment comes after postdeposition annealing. The samples with the best stoichiometry before and after annealing are the samples grown at the cathodic voltages of 1450 mV and 1455 mV with Cd/S = 0.92 after annealing. All other samples have Cd/S < 0.92 after annealing. It should be mentioned at this point though that EDX is not a very accurate technique for the precise determination of chemical composition. However, it is the only available technique within our reach at the time of this project. As a result, the compositional analysis results presented in this work are rather qualitative than quantitative.

4. Conclusions

Electrodeposition of CdS thin films at different cathodic growth voltages and characterisation of the films before and after postdeposition heat treatment have been presented. The electrodeposition of these layers was carried out using two-electrode system for process simplification and cost reduction. PEC results show that all the deposited samples have n-type electrical conductivity over the range of cathodic deposition voltages of 1445–1465 mV considered. XRD results show that as-deposited samples were polycrystalline in nature with mixed cubic and hexagonal CdS phases. After annealing however, the XRD peaks representing cubic phase disappear completely while the peaks of the hexagonal phase are enhanced with preferred orientation in the (002) plane. Further analysis of the structural properties shows that crystallites of the electrodeposited CdS samples are strained with internal strain values in the range 5.64×10^{-3} – 6.82×10^{-3} which reduced to 2.68×10^{-3} – 4.54×10^{-3} after annealing with prior CdCl₂ treatment. The number of dislocation lines per unit area is found to be in the range 1.57×10^{11} – $2.27 \times 10^{11} \text{ cm}^{-2}$ and reduced to 0.25×10^{11} – $1.01 \times 10^{11} \text{ cm}^{-2}$ after annealing. The number of crystallites per unit area is found to reduce from 3.2×10^{12} – $5.6 \times 10^{12} \text{ cm}^{-2}$ for as-deposited samples to 0.2×10^{12} – $1.6 \times 10^{12} \text{ cm}^{-2}$ after annealing, indicating increase in crystallite sizes after annealing. Crystallite sizes of the as-deposited films were in the range 21–25 nm which increased to 31–63 nm after annealing. The result of optical characterisation shows that the transmittance gets slightly weaker at lower deposition voltages while absorbance follows the opposite trend. The energy bandgap of all the annealed CdS films comes to 2.42 eV. SEM reveals that CdCl₂ treatment, with saturated CdCl₂ solution in methanol, results in cementing together of the surface grains after annealing thus modifying the surfaces of the films. EDX analysis shows that the electrodeposited CdS films are S-rich under the conditions used. The overall result suggests the best cathodic growth voltage to be in the range 1445–1450 mV.

Conflicts of Interest

The authors declare that there is no conflict of interest regarding the publication of this paper.

Acknowledgments

The principal author wishes to thank the Federal University of Technology, Owerri, Nigeria, and University of the Free State, South Africa, for financial support.

References

- [1] F. Lisco, P. M. Kaminski, A. Abbas et al., "High rate deposition of thin film cadmium sulphide by pulsed direct current magnetron sputtering," *Thin Solid Films*, vol. 574, pp. 43–51, 2015.
- [2] A. A. Ojo and I. M. Dharmadasa, "15.3% efficient graded bandgap solar cells fabricated using electroplated CdS and CdTe thin films," *Solar Energy*, vol. 136, pp. 10–14, 2016.
- [3] W. K. Metzger, "The potential and device physics of interdigitated thin film solar cells," *Journal of Applied Physics*, vol. 103, no. 9, article 094515, 2008.
- [4] X. Wang, X. He, H. Zhu et al., "Subatomic deformation driven by vertical piezoelectricity from CdS ultrathin films," *Science Advances*, vol. 2, no. 7, article e1600209, 2016.
- [5] Y. Kraftmankher, "Experiments on photoconductivity," *European Journal of Physics*, vol. 33, pp. 503–511, 2012.
- [6] R. M. Ma, L. Dai, and G. G. Qin, "High-performance nano-Schottky diodes and nano-MESFET's made on single CdS nanobelts," *Nano Letters*, vol. 7, no. 4, pp. 868–873, 2007.
- [7] T. Gaewdang and N. Wongcharoen, "Heterojunction properties of p-CuO/n-CdS diode," *Advanced Materials Research*, vol. 1098, pp. 1–5, 2015.
- [8] J. S. Meth, S. G. Zane, and G. Nunes Jr., "Dual insulated-gate field-effect transistors with cadmium sulfide active layer and a laminated polymer dielectric," *Applied Physics Letters*, vol. 84, no. 15, pp. 2922–2924, 2004.
- [9] S. T. Navale, A. T. Mane, M. A. Chougule, N. M. Shinde, J. H. Kim, and V. B. Patil, "Highly selective and sensitive CdS thin film sensors for detection of NO₂ gas," *RSC Advances*, vol. 4, pp. 44547–44554, 2014.
- [10] I. A. Kirovskaya, O. T. Timoshenko, and E. O. Karpova, "The catalytic and photocatalytic properties of InP-CdS and ZnTe-CdS system components," *Russian Journal of Physical Chemistry A*, vol. 85, no. 4, pp. 557–560, 2011.
- [11] K. Deng and L. Li, "CdS nanoscale photodetectors," *Advanced Materials*, vol. 26, no. 17, pp. 2619–2635, 2014.
- [12] A. Bosio, N. Romeo, S. Mazzamuto, and V. Canevari, "Polycrystalline CdTe thin films for photovoltaic applications," *Progress in Crystal Growth and Characterization of Materials*, vol. 52, no. 4, pp. 247–279, 2006.
- [13] M. Kim, A. Ochirbat, and H. J. Lee, "CuS/CdS quantum dot composite sensitizer and its applications to various TiO₂ mesoporous film-based solar cell devices," *Langmuir*, vol. 31, no. 27, pp. 7609–7615, 2015.
- [14] N. Naghavi, G. Renou, V. Bockele et al., "Chemical deposition methods for cd-free buffer layers in CI(G)S solar cells: role of window layers," *Thin Solid Films*, vol. 519, no. 21, pp. 7600–7605, 2011.
- [15] Z. Lu, R. Jin, Y. Liu et al., "Optimization of chemical bath deposited cadmium sulfide buffer layer for high-efficient CIGS thin film solar cells," *Materials Letters*, vol. 204, pp. 53–56, 2017.
- [16] X. Shen, A. Yuan, F. Wang, J. Hong, and Z. Xu, "Fabrication of well-aligned CdS nanotube by CVD-template method," *Solid State Communications*, vol. 133, no. 1, pp. 19–22, 2005.

- [17] A. Kerimova, E. Bagiyev, E. Aliyeva, and A. Bayramov, "Nanostructured CdS thin films deposited by spray pyrolysis method," *Physica Status Solidi C*, vol. 14, no. 6, article 1600144, pp. 1–3, 2017.
- [18] N. R. Paudel, K. A. Wieland, and A. D. Compaan, "Ultrathin CdS/CdTe solar cells by sputtering," *Solar Energy Materials and Solar Cells*, vol. 105, pp. 109–112, 2012.
- [19] P. J. Sebastian and M. E. Calixto, "Porous CdS:CdO composite structure formed by screen printing and sintering of CdS in air," *Thin Solid Films*, vol. 360, no. 1-2, pp. 128–132, 2000.
- [20] A. A. Ziabari and F. E. Ghodsi, "Growth, characterization and studying of sol-gel derived CdS nanocrystalline thin films incorporated in polyethyleneglycol: effect of post-growth heat treatment," *Solar Energy Materials and Solar Cells*, vol. 105, pp. 249–262, 2012.
- [21] J. Schaffner, E. Feldmeier, A. Swirschuk, H. J. Schimper, A. Klein, and W. Jaegermann, "Influence of substrate temperature, growth rate and TCO substrate on the properties of CSS-deposited CdS thin films," *Thin Solid Films*, vol. 519, no. 21, pp. 7556–7559, 2011.
- [22] D. G. Diso, G. E. A. Muftah, V. Patel, and I. M. Dharmadasa, "Growth of CdS layers to develop all-electrodeposited CdS/CdTe thin film solar cells," *Journal of Electrochemical Society*, vol. 157, no. 6, pp. H647–H651, 2010.
- [23] M. Rami, E. Benamar, M. Fahoume, F. Chraibi, and A. Ennaoui, "Effect of heat treatment with CdCl₂ on the electrodeposited CdTe/CdS heterojunction," *Moroccan Journal of Condensed Matter*, vol. 3, no. 1, pp. 66–70, 2000.
- [24] A. N. Abdul-Manaf, A. R. Weerasinghe, O. K. Echendu, and I. M. Dharmadasa, "Electro-plating and characterisation of cadmium sulphide thin films using ammonium thiosulfate as the sulfur source," *Journal of Materials Science: Materials in Electronics*, vol. 26, no. 4, pp. 2418–2429, 2015.
- [25] O. K. Echendu and I. M. Dharmadasa, "Graded-bandgap solar cells using all-electrodeposited ZnS, CdS and CdTe thin-films," *Energies*, vol. 8, no. 5, pp. 4416–4435, 2015.
- [26] O. K. Echendu, A. R. Weerasinghe, D. G. Diso, F. Fauzi, and I. M. Dharmadasa, "Characterization of *n*-type and *p*-type ZnS thin layers grown by electrochemical method," *Journal of Electronic Materials*, vol. 42, pp. 692–700, 2013.
- [27] O. K. Echendu, F. Fauzi, A. R. Weerasinghe, and I. M. Dharmadasa, "High short-circuit current density CdTe solar cells using all-electrodeposited semiconductors," *Thin Solid Films*, vol. 556, pp. 529–534, 2014.
- [28] A. A. Ojo and I. M. Dharmadasa, "Optimisation of pH of cadmium chloride post-growth-treatment in processing CdS/CdTe based thin film solar cells," *Journal of Materials Science: Materials in Electronics*, vol. 28, no. 10, pp. 7231–7242, 2017.
- [29] M. Miyake, K. Murase, T. Hirato, and Y. Awakura, "Hall effect measurements on CdTe layers electrodeposited from acidic aqueous electrolyte," *Journal of Electroanalytical Chemistry*, vol. 562, no. 2, pp. 247–253, 2004.
- [30] G. Sasikala, R. Dhanasekara, and C. Subramanian, "Electrodeposition and optical characterization of CdS thin films on ITO-coated glass," *Thin Solid Films*, vol. 302, pp. 71–76, 1997.
- [31] O. I. Olusola, O. K. Echendu, and I. M. Dharmadasa, "Development of CdSe thin films for application in electronic devices," *Journal of Materials Science: Materials in Electronics*, vol. 26, no. 2, pp. 1066–1076, 2015.
- [32] S. Chander and M. S. Dhaka, "Preparation and physical characterization of CdTe thin films deposited by vacuum evaporation for photovoltaic applications," *Advanced Materials Letters*, vol. 6, no. 10, pp. 907–912, 2015.
- [33] S. Chander and M. S. Dhaka, "Optimization of physical properties of vacuum evaporated CdTe thin films with the application of thermal treatment for solar cells," *Materials Science in Semiconductor Processing*, vol. 40, pp. 708–712, 2015.
- [34] H. Metin, S. Erat, F. M. Emen et al., "Thermoluminescence properties of CdS films under nitrogen atmosphere," *Journal of Luminescence*, vol. 130, no. 8, pp. 1531–1538, 2010.
- [35] R. Xie, J. Su, M. Li, and L. Guo, "Structural and photoelectrochemical properties of Cu-doped CdS thin films prepared by ultrasonic spray pyrolysis," *International Journal of Photoenergy*, vol. 2013, Article ID 620134, 7 pages, 2013.
- [36] F. Chernow, G. Eldridge, G. Ruse, and L. Wahlin, "High conductivity p-type CdS," *Applied Physics Letters*, vol. 12, no. 10, pp. 339–341, 1968.
- [37] O. K. Echendu, *Thin Film Solar Cells Using All-Electrodeposited ZnS, CdS and CdTe Materials*, Doctoral Thesis, Sheffield Hallam University, United Kingdom, 2014.

Research Article

The Effects of Interdot Spacing and Dot Size on the Performance of InGaAs/GaAs QDIBSC

Sayed Amina Amin,¹ Md. Tanvir Hasan,² and Muhammad Shaffatul Islam³

¹Department of Electrical and Electronic Engineering, American International University-Bangladesh (AIUB), Dhaka 1213, Bangladesh

²Department of Electrical and Electronic Engineering, Jessore University of Science and Technology (JUST), Jessore 7408, Bangladesh

³Department of Electrical and Electronic Engineering, World University of Bangladesh (WUB), Dhaka 1205, Bangladesh

Correspondence should be addressed to Sayeda Anika Amin; anika.amin.30@gmail.com

Received 2 June 2017; Accepted 24 September 2017; Published 26 October 2017

Academic Editor: Srinivas Devayajanam

Copyright © 2017 Sayeda Anika Amin et al. This is an open access article distributed under the Creative Commons Attribution License, which permits unrestricted use, distribution, and reproduction in any medium, provided the original work is properly cited.

In_{0.53}Ga_{0.47}As/GaAs-based quantum dot intermediate band solar cells (QDIBSCs) have been designed and optimized for the next generation photovoltaic technology. The wave behavior of charge carriers inside the dot and their barrier have been analyzed with different dot sizes and interdot spacing. The device characteristics such as short circuit current density, J_{sc} , open circuit voltage, V_{oc} , and conversion efficiency, η , have been evaluated. Based on the behavior of electron wave function, it is found that varying the dot spacing leads to a change in the IB width and in the density of states, whereas varying the size of dots leads to a formation of a second IB. For a fixed dot spacing, two ranges of dot sizes vary the number of IBs in In_{0.53}Ga_{0.47}As/GaAs QDIBSC. Smaller dots of a size ranging from 2 nm to 5 nm form a single IB while larger dots of a size ranging from 6 nm to 9 nm can produce 2 IBs. The efficiency of 2 IBs close to 1 IB suggests that formation of multiple IBs can possibly enhance the device efficiency.

1. Introduction

The concept of an intermediate band solar cell (IBSC) has created enormous interests to replace the traditional solar devices. The major reason behind this is the maximum theoretical limit of 63.2% [1] calculated by Luque and Martí which outstrips the single-junction Shockley-Queisser limit [2]. For fully concentrated light, this efficiency occurs when the largest bandgap is 1.93 eV under certain assumptions [1]. The intermediate band (IB) is attained by introducing an IB material between two selective contacts of *p* type and *n* type [3] which split the energy bandgap E_g into two subbandgaps. This allows the formation of additional electron-hole pairs from the absorption of two subbandgap energy photons [4]. Low-dimensional semiconductor quantum dots (QDs) positioned in the absorption region of a p-i-n solar cell have been proved to be pertinent to realize IBSC concept [1, 5, 6]. The tight and regular arrangements of QDs in a quantum dot intermediate band solar

cell (QDIBSC) lead to the formation of an IB or a superlattice miniband that is well separated in energy from the higher order states.

The InAs/GaAs and InGaAs/GaAs quantum dot systems have become the most canonical systems for studying the concept of IBSCs [7, 8]. The GaAs has reached an efficiency of 28.8% as reported by Green et al. [9] which is quite close to its Shockley-Queisser limit. However, irrespective of the potential to achieve high efficiency, reports of QDIBSCs have shown significantly low efficiencies. An efficiency of 18.7% is achieved under air mass 1.5 condition with an antireflective coating by Tanabe et al. [10]. In order to mitigate the gap between the theoretical and experimental results, researchers are constantly probing new approaches to heighten the efficiency of the IBSC devices. A major part of the ongoing research is devoted to increase the photocurrent generation of two-step photon absorption. However, limited attention has been paid to the structural issues such as the dot shape, size, dot-to-dot spacing, and number of IBs which have a

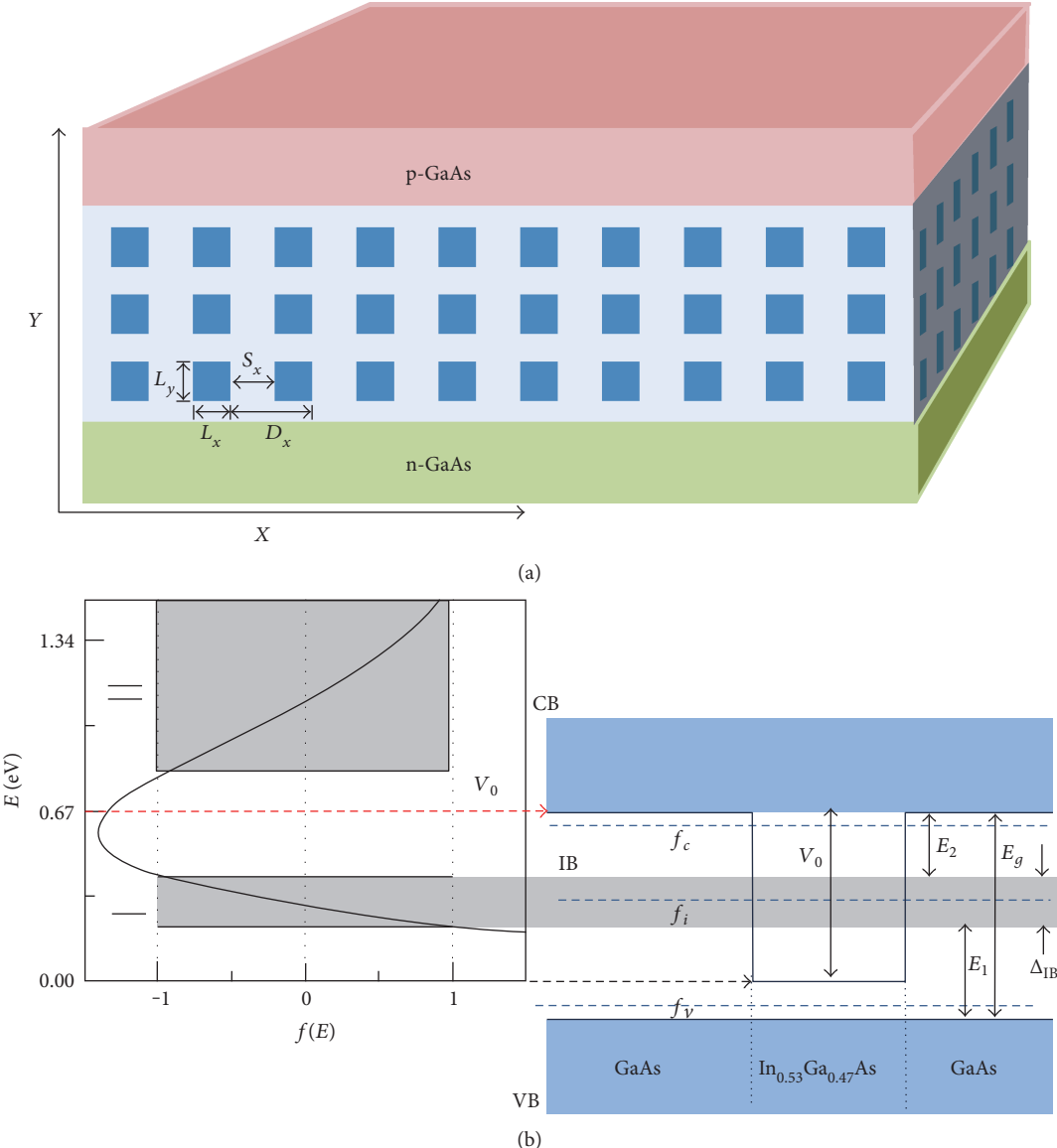


FIGURE 1: (a) Schematic structure and (b) miniband dispersion along with energy band diagram of In_{0.53}Ga_{0.47}As/GaAs quantum dot intermediate band solar cell.

significant impact on the collection efficiency of photon-generated carriers. Advancement in the structural issues can pave the way for higher efficiency and eventually provide a guideline for growth engineers. In our previous study, we demonstrated the influence of In_{0.53}Ga_{0.47}As/GaAs QDs in the IBSC and obtained the values of horizontal and vertical dot spacing which exhibited the maximum efficiency [11]. In this work, a detailed analysis of electron wave function for different dot spacing and size have been performed. The relation between the dot size and number of IBs is determined from the discrete quantized energy levels of quantum dots. Further, the characteristic parameters of the device, such as conversion efficiency, η , short circuit current density, J_{sc} , and open circuit voltage, V_{oc} , have been evaluated, and their relation with the widths and subbandgaps of the IB was derived.

2. Theory and Model

In the present work, a QDIBSC model consisting of In_{0.53}Ga_{0.47}As dots and GaAs barrier material is studied. The schematic structure of the device is shown in Figure 1(a). As the In_{0.53}Ga_{0.47}As QDs are regularly placed in the intrinsic region of the p-i-n GaAs cell, the energy levels spread out into minibands. For the analysis, the In_{0.53}Ga_{0.47}As dots are assumed to have a cubical structure with equal dimensions, and the size of each dot in an infinite sequence is denoted by L_x , L_y , and L_z along with the three coordinate axis directions as depicted in Figure 1(a). S_x , S_y , and S_z stand for the interdot spacing/dot spacing along with the three coordinate axes. $D_x = L_x + S_x$ stands for a single period of QDs. Both the dot size and spacing are assumed to be equivalent along with every direction. The device is simulated using

the commercial software Silvaco ATLAS [12]. All calculations are performed at a room temperature under AM 1.5, 1 sun condition. The values of the band parameters used in the simulation are presented in Table 1.

To describe the wave function of electrons in dot and barrier, the time-independent Schrodinger equation and Kronig-Penney model are used [13]. Figure 1(b) shows the energy band diagram along with the wave function of electron inside the $\text{In}_{0.53}\text{Ga}_{0.47}\text{As}$ dots and GaAs barrier. The structure produces two potential energies for the barrier, one for conduction band electrons, that is, conduction band offset, V_0 , and the other for valence band holes, that is, valence band offset. For the simplicity of analysis, it is assumed that the energy corresponding to the top of the valence band is the same both in the barrier and in the dot; that is, the valence band offset is zero. As a consequence, only the effect of the conduction band offset, V_0 , to create the wave vectors is considered. The effects of strain and piezoelectricity are ignored, and their effects on the electronic and optical properties of the QD array are also neglected. The Schrodinger equation in a quantum dot array for a single electron can be expressed as [13]

$$\left[-\frac{\hbar^2}{2} \nabla_r \frac{1}{m^*(r)} \nabla_r + V(r) \right] \phi(r) = E \phi(r), \quad (1)$$

where the electronic potential, $V(r) = Vx(x) + Vy(y) + Vz(z)$, is the sum of the potential functions D_x , D_y , and D_z along with the three dimensional directions, respectively. In $\hbar = h/2\pi$, h is Planck's constant and $\phi(r)$ is the envelope wave function. According to the Kronig-Penney model [13], the solution of the Schrodinger equation (1) can be given in the following form.

The energy of a single electron along a particular coordinate axis direction, E_ξ , is greater than or equal to the potential barrier, V_0 , that is, if $E_\xi \geq V_0$,

$$\cos(q\xi D\xi) = \cos(k_\xi^w L\xi) \cos(k_\xi^B S_\xi) - \frac{1}{2} \left(\frac{k_\xi^w m_B^*}{k_\xi^B m_w^*} + \frac{k_\xi^B m_w^*}{k_\xi^w m_B^*} \right) \sin(k_\xi^w L\xi) \times \sin(k_\xi^B S_\xi). \quad (2)$$

If $0 < E_\xi < V_0$,

$$\cos(q\xi D\xi) = \cos(k_\xi^w L\xi) \cosh(k_\xi^B S_\xi) - \frac{1}{2} \left(\frac{k_\xi^w m_B^*}{k_\xi^B m_w^*} - \frac{k_\xi^B m_w^*}{k_\xi^w m_B^*} \right) \sin(k_\xi^w L\xi) \times \sinh(k_\xi^B S_\xi), \quad (3)$$

where

$$k_\xi^B = \frac{\sqrt{2m_B^* |E_\xi - V_0|}}{\hbar}, \quad (4)$$

$$k_\xi^w = \frac{\sqrt{2m_w^* |E_\xi|}}{\hbar},$$

TABLE 1: Values of different parameters [15].

Parameters	Values	
	GaAs	$\text{In}_{0.53}\text{Ga}_{0.47}\text{As}$
Bandgap (eV)	1.42	0.75
Electron effective mass (m_0)	0.067	0.0452
Permittivity (F/cm)	13.2	14.2
Electron affinity (eV)	4.07	4.13
Density of states in conduction band (cm^{-3})	4.35×10^{17}	1.15×10^{17}
Density of states in valence band (cm^{-3})	8.16×10^{18}	8.12×10^{18}
Electron/hole lifetime (ns)		1

where m_B^* and m_w^* are the effective masses of electron in the barrier region and dot region, respectively. In order to obtain the electron wave vector in the dot and barrier regions, the left side of (2) and (3), $\cos(q\xi D\xi)$, can be expressed as a function $f(E_\xi)$ of energy E_ξ [14].

For $E_\xi \geq V_0$,

$$f(E_\xi) = \cos(k_\xi^w L\xi) \cos(k_\xi^B S_\xi) - \frac{1}{2} \left(\frac{k_\xi^w m_B^*}{k_\xi^B m_w^*} + \frac{k_\xi^B m_w^*}{k_\xi^w m_B^*} \right) \sin(k_\xi^w L\xi) \times \sin(k_\xi^B S_\xi). \quad (5)$$

For $0 < E_\xi < V_0$,

$$f(E_\xi) = \cos(k_\xi^w L\xi) \cosh(k_\xi^B S_\xi) - \frac{1}{2} \left(\frac{k_\xi^w m_B^*}{k_\xi^B m_w^*} - \frac{k_\xi^B m_w^*}{k_\xi^w m_B^*} \right) \sin(k_\xi^w L\xi) \times \sinh(k_\xi^B S_\xi). \quad (6)$$

Apparently, from (5) and (6), the left hand side is a function of energy (E) only which should be constrained by ± 1 [13]. As the energy changes from 0 to V_0 , (5) and (6) determine the IBs inside the potential barrier, V_0 . For $\text{In}_{0.53}\text{Ga}_{0.47}\text{As}$ dots, Figure 1(b) exhibits two minibands labeled as miniband I (0.087, 0.235) and miniband II (0.424, 0.938). As the valence band offset is assumed to be zero, the value of potential barrier V_0 can be calculated by subtracting the bandgap of the dot from the barrier material. For $\text{In}_{0.53}\text{Ga}_{0.47}\text{As}$ dots, the value of V_0 is found to be 0.67 eV. As seen from Figure 1(b), the miniband I has energy lower than V_0 ; subsequently, it is located inside the dot, whereas miniband II has energy above V_0 , hence distributed in the barrier region. As the minibands in the barrier become a part of the conduction band, only the minibands formed inside the dots are regarded as IBs. For the separation of minibands from the CB and VB, it is crucial to determine their widths. The widths of the formed minibands can be calculated from Figure 1(b). The total width of the miniband I is equal to 3 times the width of miniband I along with every direction. So, $\Delta_{IB} = 3 \times (\text{the bottom point of miniband I} - \text{starting point of miniband I}) = 3 \times (0.235 - 0.087) \text{ eV} = 0.444 \text{ eV}$.

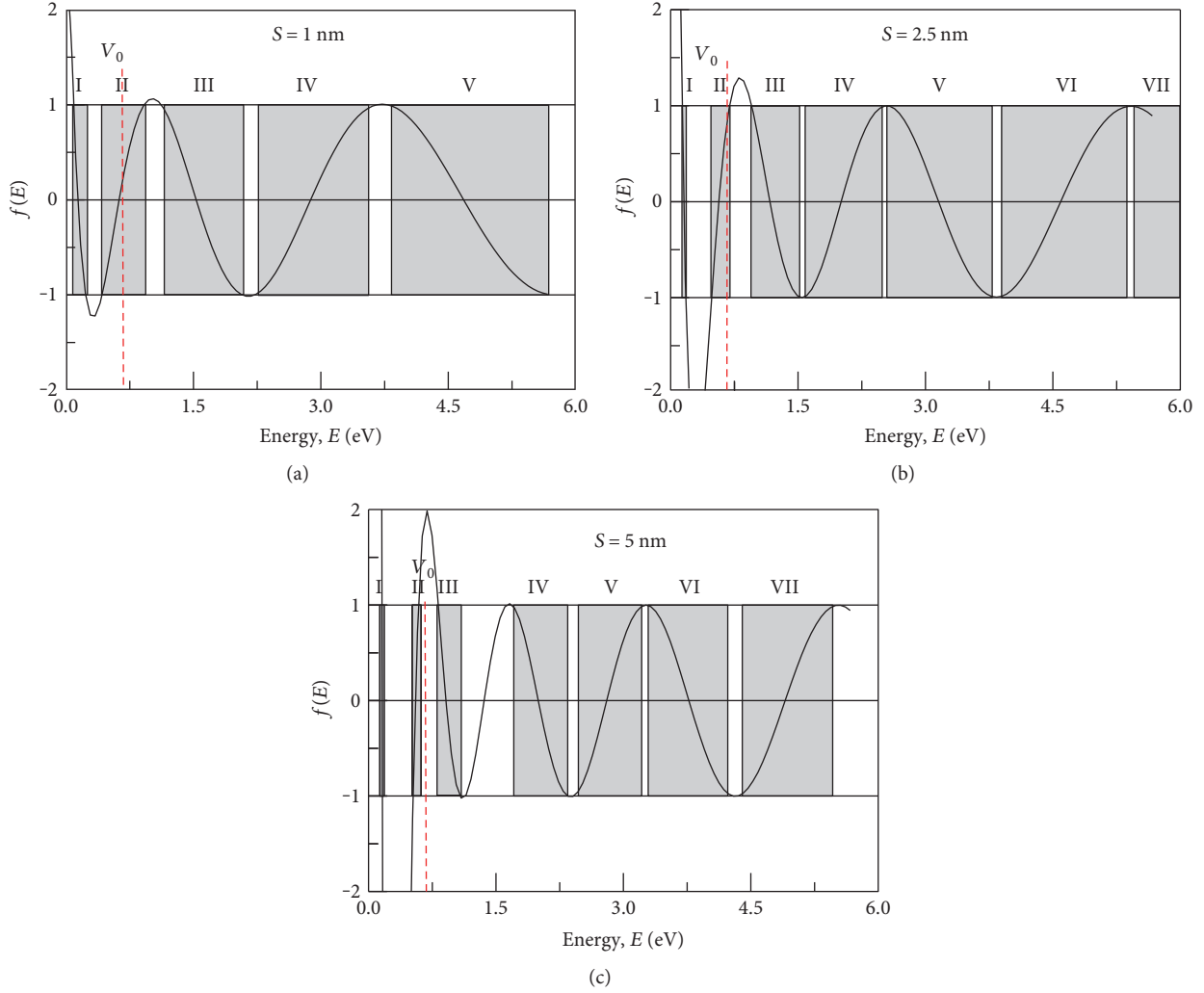


FIGURE 2: Miniband dispersion in $\text{In}_{0.53}\text{Ga}_{0.47}\text{As}$ QDIBSC for dot spacing of (a) 1 nm, (b) 2.5 nm, and (c) 5 nm.

The subbandgap, E_1 , can be given by $E_1 = E_{\text{gIn}_{0.53}\text{Ga}_{0.47}\text{As}} + 3 \times (\text{starting point of miniband I}) \text{ eV} - E_{\text{gIn}_{0.53}\text{Ga}_{0.47}\text{As}} + 3 \times (0.087) \text{ eV}$ where $E_{\text{gIn}_{0.53}\text{Ga}_{0.47}\text{As}}$ is the bandgap of $\text{In}_{0.53}\text{Ga}_{0.47}\text{As}$. The subbandgap E_2 is given by $E_2 = E_{\text{g}} - E_1 - \Delta_{\text{IB}}$ eV for a single IB.

3. Results and Discussion

3.1. Dot Spacing. In our previous study, we found the values of dot spacing which yielded the maximum efficiency for $\text{In}_{0.53}\text{Ga}_{0.47}\text{As}/\text{GaAs}$ QDIBSC [11]. However, relation between the dot spacing and the distribution of IB energies in the forbidden gap was not studied. Here, we commence the discussion first by manifesting the relation of dot spacing, S , with the electron wave function and then with the width and position of IB. The bandwidth $f(E)$, as a function of different dot spacing ($S = 1 \text{ nm}, 2.5 \text{ nm}, \text{ and } 5 \text{ nm}$) for a fixed value of dot size ($L = 5 \text{ nm}$), in the dot and barrier regions is depicted in Figure 2. From Figure 2, it is recognized that in all three cases, that is, Figures 2(a), 2(b), and 2(c) miniband I lies inside the boundary of V_0 , while miniband II remains outside. As a consequence, miniband I is the only

intermediate band found in the forbidden energy gap. It is also seen that the distance between miniband I and CB increases with increasing S from 1 nm to 5 nm, producing more number of minibands. Figure 3 demonstrates the variation of the width of the miniband I, Δ_{IB} , with dot spacing, S , and the subbandgaps, E_1 and E_2 . Inside the host gap, the subbandgaps E_1 and E_2 determine the position of the IB. Figure 3 shows increasing S evidently broadens the subbandgaps E_1 and E_2 shrinking the width Δ_{IB} to a value close to zero. As shown in Figure 3(a), from 1 nm to 2.5 nm, the value of Δ_{IB} decreases from 0.444 eV to 0.135 eV, while from 2.5 nm to 5 nm, it decreases to 0.018 eV. The reduction in Δ_{IB} can be assigned to the decrease in the quantum states and the weak coupling of wave functions in more distant dots. In Figure 3(b), from 1 nm to 2.5 nm, both E_1 and E_2 increase approximately 13.6%, which can be attributed to the enhancement of quantum localization. These results also coincide with other works which exhibit that increasing the dot spacing results in reduced IB widths [16]. However, a larger value of Δ_{IB} is beneficial for the absorption of more sunlight to increase the current, whereas diminishing E_1 and E_2 will reduce it. As a consequence, it is in this regard

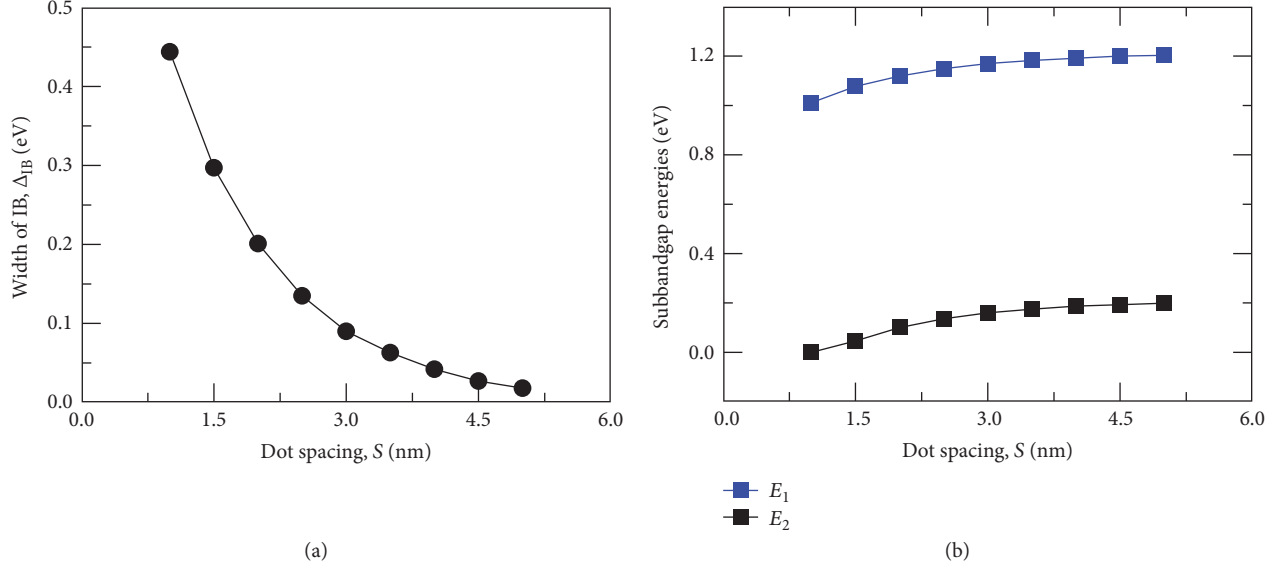
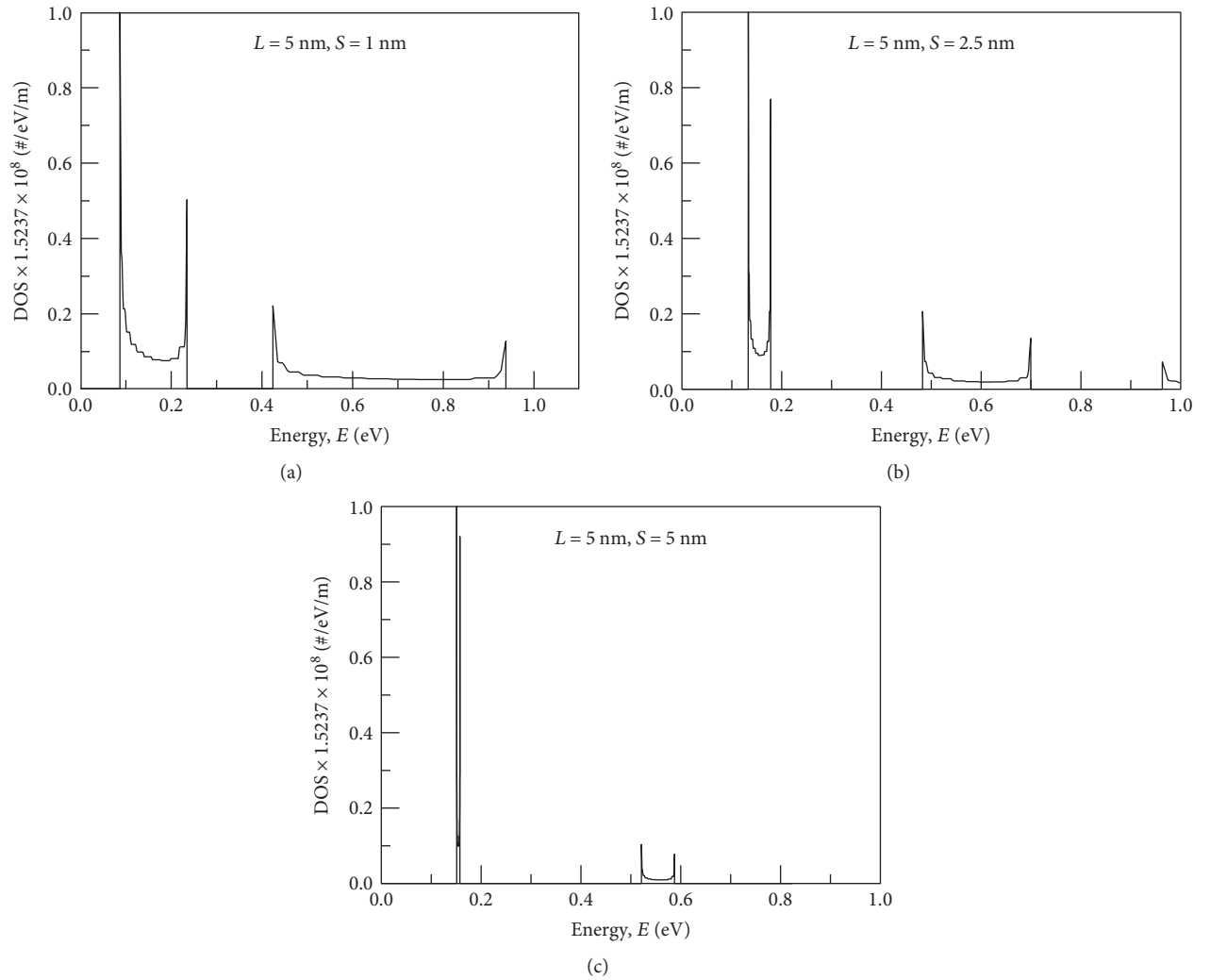
FIGURE 3: Variation of (a) IB width Δ_{IB} and (b) subbandgaps E_1 and E_2 with dot spacing, S , for a single IB.

FIGURE 4: The electron density of states (DOS) in the minibands for dot spacing of (a) 1 nm, (b) 2.5 nm, and (c) 5 nm.

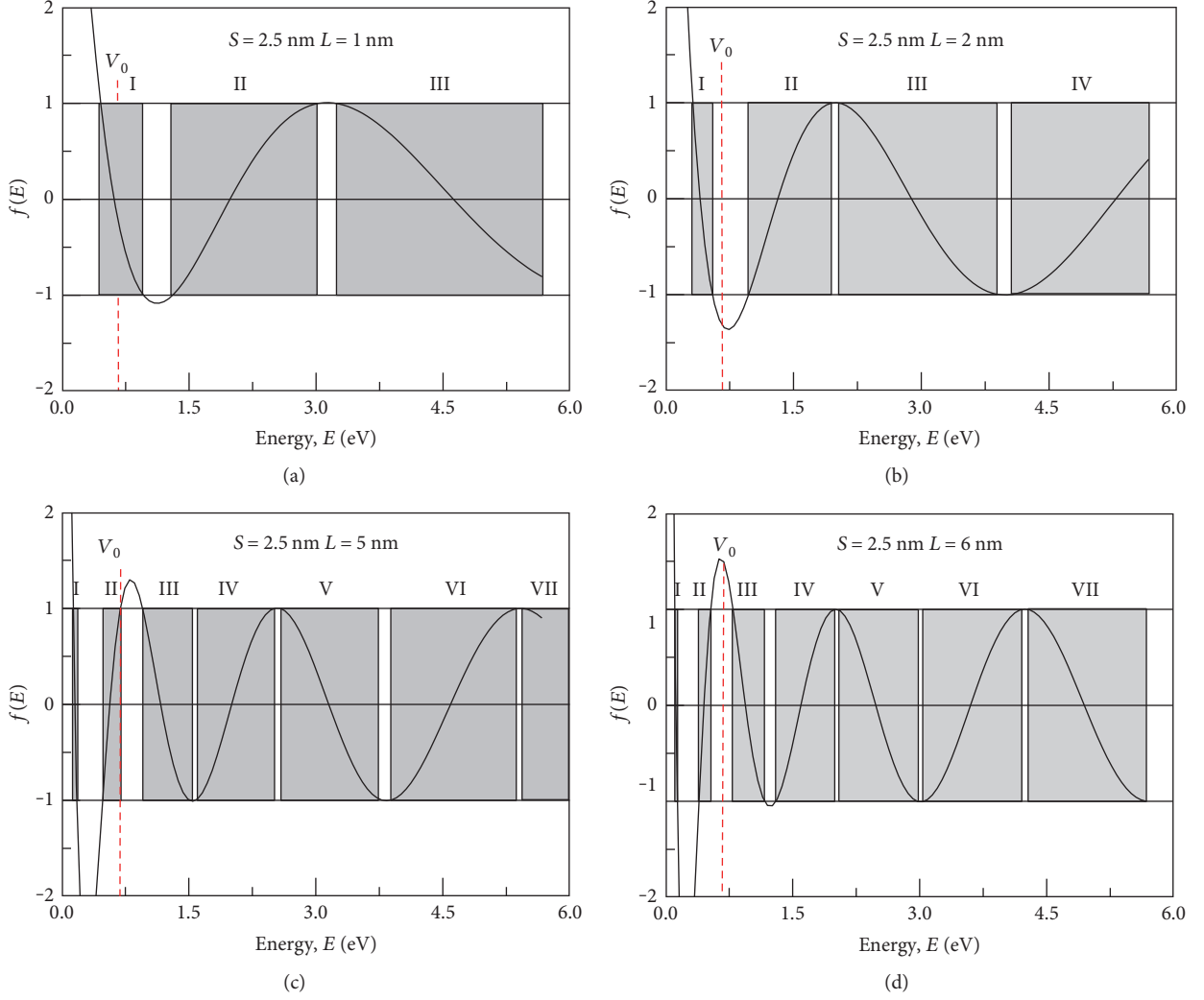


FIGURE 5: Miniband dispersion in $\text{In}_{0.53}\text{Ga}_{0.47}\text{As}$ QDIBSC dot for different dot sizes of (a) 1 nm, (b) 2 nm, (c) 5 nm, and (d) 6 nm.

imperative to attain a trade-off between the higher values of E_1 and E_2 and the lower values of Δ_{IB} . Furthermore, the electron density of states (DOS) in IB has to be as high as possible in order to pin the quasi Fermi level at its equilibrium position [17]. The DOS in the minibands for $S = 1$ nm, 2.5 nm, and 5 nm is illustrated in Figure 4. As seen from Figure 4(a), for $S = 1$ nm, a broad bandwidth of IB yields a high DOS, whereas for $S = 5$ nm, a narrow IB assists in the loss of carrier density, that is, a lower DOS. It is therefore of great necessity to choose a value between 1 nm and 5 nm in order to obtain a sufficiently high IB width and sub-bandgaps. At $S = 2.5$ nm, a moderate value of Δ_{IB} and E_1 , E_2 is achieved.

3.2. Dot Size. Next, the size of dots, L , is varied to infer its relation with the formed intermediate bands. $f(E)$ as a function of electron's energy is exhibited in Figure 5. Figures 5(a) and 5(b) illustrate the wave function of electron in the dot for $L = 1$ nm and 2 nm. For $L = 1$ nm, no intermediate band is formed as the miniband I extends to a value beyond the energy level of V_0 . For $L = 2$ nm, in Figure 5(b),

TABLE 2: Ranges of dot size which vary the number of IBs.

	1st range	2nd range
Size of dots	2 nm–5 nm	6 nm–9 nm
Number of IBs	1 IB	2 IBs

miniband I is regarded as an IB, as it remains inside the boundary value of V_0 . This implies that, for $S = 2.5 \text{ nm}$, a dot size less than 2 nm does not form any intermediate band. From Figures 5(b), 5(c), and 5(d), it can be seen that, with subsequent increase in L from 2 nm , the number of minibands tend to increase. Up to $L = 5 \text{ nm}$, only miniband I is regarded as an IB (Figure 5(c)), whereas for $L = 6 \text{ nm}$ (Figure 5(d)), both miniband I and II are considered as IBs, as both have energies lower than V_0 .

Hence, an apparent deduction that can be made from the miniband dispersion of Figure 5 is for a fixed spacing of 2.5 nm; dot sizes ranging from 2 nm to 5 nm generate a single intermediate band whereas the dot sizes from 6 nm to 9 nm are more likely to produce two IBs. It also denotes that the

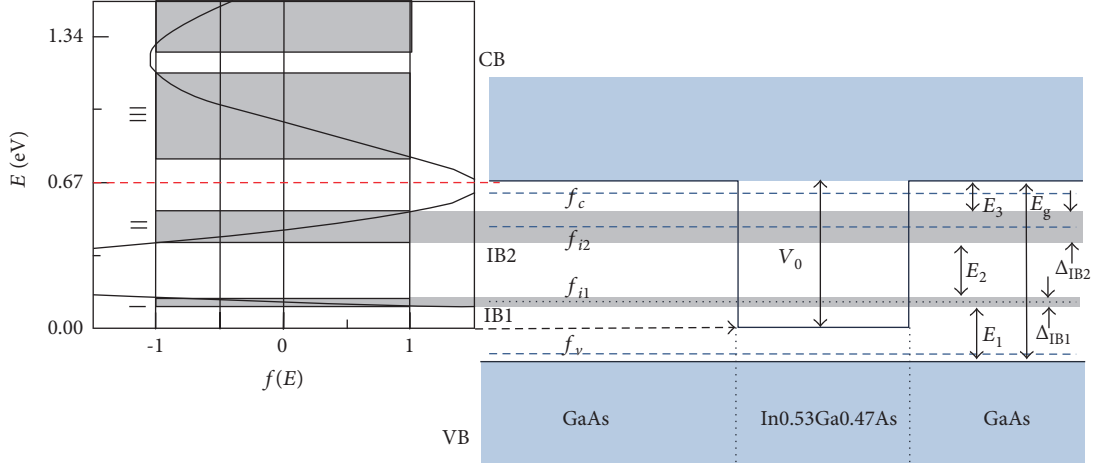


FIGURE 6: Energy band diagram and miniband dispersion of $\text{In}_{0.53}\text{Ga}_{0.47}\text{As}/\text{GaAs}$ quantum dot intermediate band solar cell for two intermediate bands.

number of IBs in a QD system is directly related to the size of dots. From these results, two ranges of dot sizes for a fixed dot spacing can be provided which vary the number of IBs. Table 2 shows these two ranges of dot sizes. The first range is from $L = 2 \text{ nm}$ to 5 nm , under which a single intermediate band is attained. The second range is from 6 nm to 9 nm , under which two intermediate bands are obtained. Figure 6 shows the energy band diagram and the distribution of minibands in dot and barrier for two IBs.

The width of the first intermediate band Δ_{IB1} as a function of dot size is shown in Figure 7(a). As the size of the dot increases from 2 nm to 5 nm , the width tends to decrease. The same trend is also found in Figure 7(b), where the widths, Δ_{IB1} and Δ_{IB2} , decrease with rising L . This decrease can be assigned to the fact that the overlap quantized levels between different QDs become small, which can cause a decline in the transitional probabilities of photo-generated carriers from VB to CB via IBs. Also, the quantum effect on the low-quantized levels is stronger than that on the higher ones. A high value of Δ_{IB2} is essential to include most of the excited electrons that come from the lower subband Δ_{IB1} and VB, respectively.

Compared to a single IB, two IBs in a QDIBSC have six upward transitions and three subbandgaps E_1 , E_2 , and E_3 as shown in Figure 6. Introducing more levels in the bandgap increases the number of upward transitions as well as the probability of absorption of low-energy photons. According to the bound state energy levels obtained for typical QD parameters, the subbandgap energies are organized as $E_1 > E_2 > E_3$. This condition is important as it preserves the discrete nature of QDs inside the host semiconductor material. Figure 7(c) illustrates the variation of the subbandgaps E_1 , E_2 , and E_3 with the second range of dot sizes for two IBs. In Figure 7(c), subbandgaps E_1 and E_2 descend with the increasing L while E_3 shows an ascending trend. The increase in L tends to decrease the gap between VB and Δ_{IB1} and also the gap between Δ_{IB1} and Δ_{IB2} . However, at the same time, an increasing L leads to an increase in the gap between CB and Δ_{IB2} due to a fixed host gap of GaAs. Since the positions of the two intermediate bands are

determined by the subbandgaps E_1 , E_2 , and E_3 , an optimization of these subbandgaps is required for achieving the maximum cell efficiency.

The variation of the current density, J_{sc} , and open circuit voltage, V_{oc} , with two ranges of L is illustrated in Figure 8. From 2 nm to 5 nm , the J_{sc} increases around 6.5% while the open circuit voltage V_{oc} remains almost constant. The enhancement in the current density with dot size can be attributed to the increase in a generation rate. Larger dots lead to higher generation rates [18] and broaden the range of photon energy which can further result in creation of electron-hole pairs that in turn boosts the J_{sc} . On the other hand, as the V_{oc} is dependent on the chemical potential between VB and CB, in other words, in the host bandgap, E_g , the variation in L does not affect E_g ; hence, V_{oc} implies a weak dependence on L . In the second range of L , from 6 nm to 7 nm , J_{sc} increases around 1% and then decreases. This slight increase in the current can be assigned to the formation of a second IB which heightens the photo collection efficiency. Beyond $L = 7 \text{ nm}$, the decreasing slope of J_{sc} can be due to the positioning of the two IBs in the host gap. The peak value of J_{sc} is achieved at $L = 5 \text{ nm}$ and $L = 7 \text{ nm}$ for 1 IB and 2 IBs, respectively. Figure 9 shows the J - V characteristic curves for single IB and two IBs for optimized L values. For a single IB, the maximal efficiency of 22.8% is achieved at $L = 5 \text{ nm}$ due to the obtained maximum J_{sc} . For two IBs, the optimal efficiency is around 22.6% for $L = 7 \text{ nm}$. Table 3 shows the summarized results of J_{sc} , V_{oc} , FF , and η for no IB, that is, a single junction GaAs cell, 1 IB, and 2 IBs. From Table 3, it is found that, without the insertion of QD layer, the efficiency of the cell is 21.5% which increases approximately 6.04% and 5.1% with inclusion of 1 IB and 2 IBs, respectively. The insertion of QD layers introduces several confined electrons and hole states inside the intrinsic region which enhance the drifting action of the carriers by making use of the built-in electric field of the p-n junction. Increasing the number of IBs in a QDIBSC should lead to higher efficiency. Theoretically, two IBs should have higher efficiency compared to 1 IB. However, for $\text{In}_{0.53}\text{Ga}_{0.47}\text{As}/\text{GaAs}$, it is found that two IBs resulted in a lower efficiency than that of using one IB,

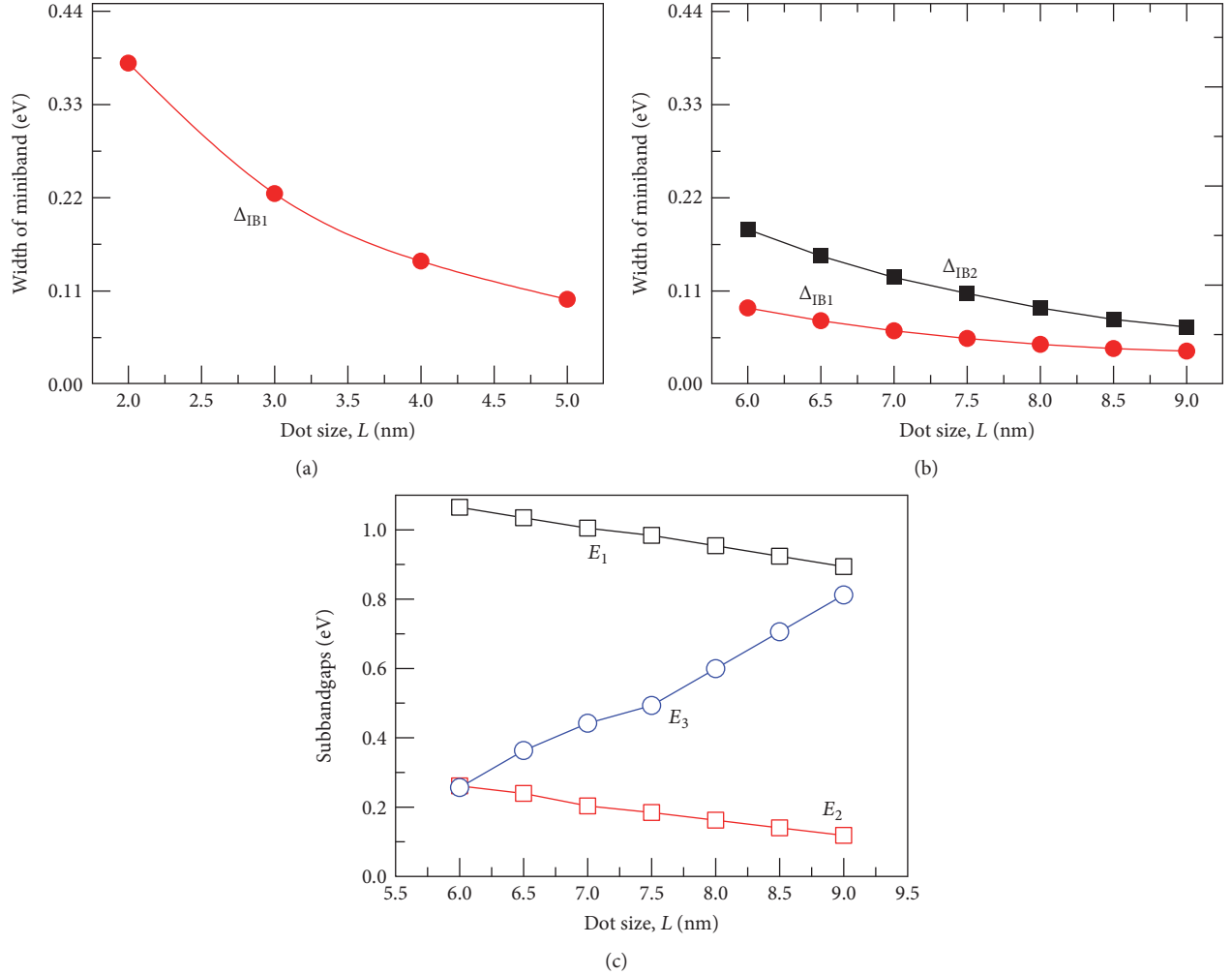


FIGURE 7: (a) Variation of Δ_{IB1} with the 1st range of dot size. (b) Variations of Δ_{IB1} and Δ_{IB2} with the second range of dot size and (c) subbandgaps E_1 , E_2 , and E_3 with dot size.

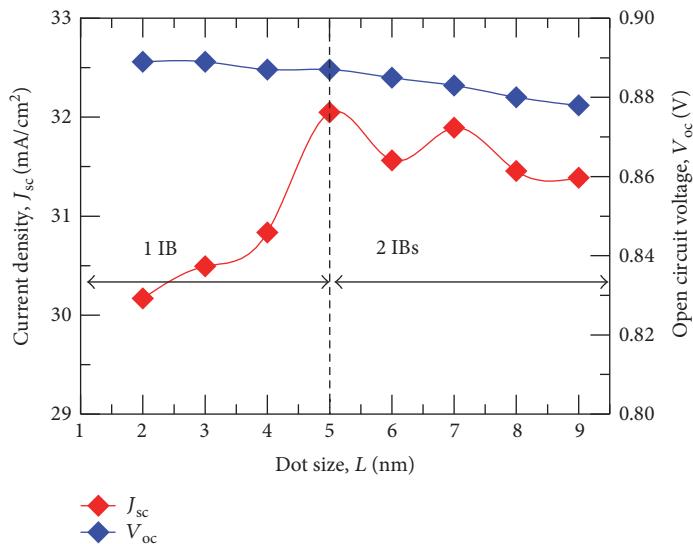
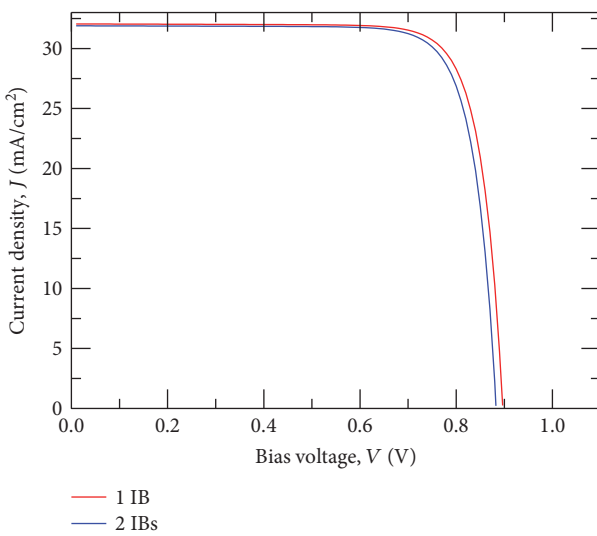


FIGURE 8: Dot size versus J_{sc} and V_{oc} for 1 IB and 2 IBs.

FIGURE 9: J - V characteristic curves for 1 IB and 2 IBs.TABLE 3: Summarized results of J_{sc} , V_{oc} , FF, and η for 0, 1, and 2 intermediate bands.

Number of IBs	J_{sc} (mA/cm ²)	V_{oc} (volt)	FF (%)	η (%)
0	29.5	0.9	81.2	21.5
1 IB	32.05	0.886	80.3	22.8
2 IBs	31.89	0.883	80.3	22.6

by a margin of 0.2%. This decrease could have been caused due to a narrow host gap, E_g (for $In_{0.53}Ga_{0.47}As$, E_g is fixed at a value of 1.42 eV). For two IBs to surpass one IB in efficiency, the host gap should have a value greater than or equal to 2 eV [19]. Efficiency of two IBs is likely to exceed that of one IB, given that there is a scope for independent energy transitions, that is, E_1 , E_2 , and E_g , to be optimized and matched well with the absorption of solar spectrum.

4. Conclusion

In this work, a study based on $In_{0.53}Ga_{0.47}As/GaAs$ QD array was investigated. Formation of minibands with regard to the behavior of electron wave function in dot and barrier regions for various dot spacing and sizes is analyzed. Results reveal that emergence of a second IB in $In_{0.53}Ga_{0.47}As/GaAs$ QDIBSC relies more on the size of dots than dot spacing. Increasing dot spacing results in a narrower IB width and a lower density of states, while increasing the dot size results in formation of multiple IBs. Based on the results obtained, two different ranges of dot sizes are provided which vary the number of IBs. Smaller dots ranging from the size of 2 nm to 5 nm yield a single IB while larger dots ranging from the size of 6 nm to 9 nm produce two IBs. The conversion efficiency of 2 IBs close to the efficiency of 1 IB suggests that multiple IBs can potentially improve the efficiency, if the host bandgap and subbandgaps are optimized to match well with the absorption of solar spectrum.

Conflicts of Interest

The authors declare that they have no conflicts of interest.

References

- [1] A. Luque and A. Martí, "Increasing the efficiency of ideal solar cells by photon induced transitions at intermediate levels," *Physical Review Letters*, vol. 78, no. 26, pp. 5014–5017, 1997.
- [2] W. Shockley and H. Queisser, "Detailed balance limit of efficiency of p-n junction solar cells," *Journal of Applied Physics*, vol. 32, no. 3, p. 510, 1961.
- [3] A. Luque, A. Martí, and A. Nozik, "Solar cells based on quantum dots: multiple exciton generation and intermediate bands," *MRS Bulletin*, vol. 32, no. 03, pp. 236–241, 2007.
- [4] A. Luque, A. Martí, and C. Stanley, "Understanding intermediate-band solar cells," *Nature Photonics*, vol. 6, no. 3, pp. 146–152, 2012.
- [5] V. Aroutiounian, S. Petrosyan, A. Khachatryan, and K. Touryan, "Quantum dot solar cells," *Journal of Applied Physics*, vol. 89, no. 4, pp. 2268–2271, 2001.
- [6] R. Strandberg and T. Reenaas, "Photofilling of intermediate bands," *Journal of Applied Physics*, vol. 105, no. 12, article 124512, 2009.
- [7] Y. Okada, N. Ekins-Daukes, T. Kita et al., "Intermediate band solar cells: recent progress and future directions," *Applied Physics Reviews*, vol. 2, no. 2, article 021302, 2015.
- [8] T. Li and M. Dagenais, "High saturation intensity in InAs/GaAs quantum dot solar cells and impact on the realization of the intermediate band concept at room-temperature," *Applied Physics Letters*, vol. 110, no. 6, article 061107, 2017.
- [9] M. Green, Y. Hishikawa, W. Warta et al., "Solar cell efficiency tables (version 50)," *Progress in Photovoltaics: Research and Applications*, vol. 25, no. 7, pp. 668–676, 2017.
- [10] K. Tanabe, D. Guimard, D. Bordel, and Y. Arakawa, "High-efficiency InAs/GaAs quantum dot solar cells by metalorganic chemical vapor deposition," *Applied Physics Letters*, vol. 100, no. 19, article 193905, 2012.
- [11] S. Amin, M. Hasan, and M. Islam, " $In_xGa_{1-x}As/GaAs$ -based intermediate band solar cell: effects of quantum dots," in *2016 IEEE Region 10 Conference (TENCON)*, pp. 2753–2756, Singapore, 2016.
- [12] Silvaco Support - Download User Manuals, "Dynamic.silvaco.com," 2017, <https://dynamic.silvaco.com/dynamicweb/jsp/downloads/DownloadManualsAction.do?req=silen-manuals&nm=atlas>.
- [13] O. Lazarenkova and A. Balandin, "Miniband formation in a quantum dot crystal," *Journal of Applied Physics*, vol. 89, no. 10, pp. 5509–5515, 2001.
- [14] G. Bastard, "Theoretical investigations of superlattice band structure in the envelope-function approximation," *Physical Review B*, vol. 25, no. 12, pp. 7584–7597, 1982.
- [15] I. Vurgaftman, J. Meyer, and L. Ram-Mohan, "Band parameters for III-V compound semiconductors and their alloys," *Journal of Applied Physics*, vol. 89, no. 11, pp. 5815–5875, 2001.
- [16] A. Aly and A. Nasr, "Theoretical study of one-intermediate band quantum dot solar cell," *International Journal of Photoenergy*, vol. 2014, Article ID 904104, 10 pages, 2014.
- [17] L. Cuadra, A. Martí, and A. Luque, "Present status of intermediate band solar cell research," *Thin Solid Films*, vol. 451-452, pp. 593–599, 2004.

- [18] F. Rahayu and Y. Darma, "Simulation of charge carriers generation rate of SiGe quantum dot based intermediate band solar cell," in *AIP Conference Proceedings*, pp. 203–206, 2012.
- [19] S. Jenks and R. Gilmore, "Material selection for the quantum dot intermediate band solar cell," in *Lecture Notes in Nano-scale Science and Technology*, pp. 135–166, Springer, New York, NY, USA, 2013.

Research Article

Optical Tests on a Curve Fresnel Lens as Secondary Optics for Solar Troughs

D. Fontani,¹ P. Sansoni,¹ F. Francini,¹ M. DeLucia,² G. Pierucci,² and D. Jafrancesco¹

¹CNR-National Institute of Optics (INO), Largo E. Fermi, 6, 50125 Firenze, Italy

²Department DIEF, University of Florence, Via Santa Marta, 3, 50139 Firenze, Italy

Correspondence should be addressed to P. Sansoni; paola.sansoni@ino.it

Received 30 May 2017; Accepted 9 July 2017; Published 12 September 2017

Academic Editor: Prakash Basnyat

Copyright © 2017 D. Fontani et al. This is an open access article distributed under the Creative Commons Attribution License, which permits unrestricted use, distribution, and reproduction in any medium, provided the original work is properly cited.

A curve Fresnel lens is developed as secondary concentrator for solar parabolic troughs to reduce the number of photovoltaic cells. Specific measurements and optical tests are used to evaluate the optical features of manufactured samples. The cylindrical Fresnel lens transforms the focal line, produced by the primary mirror, into a series of focal points. The execution of special laboratory tests on some secondary concentrator samples is discussed in detail, illustrating the methodologies tailored to the specific case. Focusing tests are performed, illuminating different areas of the lens with solar divergence light and acquiring images on the plane of the photocell using a CMOS camera. Concentration measurements are carried out to select the best performing samples of curve Fresnel lens. The insertion of the secondary optics within the concentrating photovoltaic (CPV) trough doubles the solar concentration of the system. The mean concentration ratio is 1.73, 2.13, and 2.09 for the three tested lenses. The concentration ratio of the solar trough is 140 and approaches 300 after the introduction of the secondary lens.

1. Introduction

Optical characterization and practical experimentation on manufactured components are key elements to address and ameliorate the production process and to select the best performing samples. When the optical component presents a particular geometry of radiation collection, the tests need to be tailored to examine it. Furthermore, specific measurement procedures and customized set-ups can study peculiarities or interesting aspects of the examined samples. Optical tests are frequently used to identify defective portions of the realized samples to correct manufacture.

The tested component is a novel secondary optics especially designed and implemented for an existing concentrating photovoltaic (CPV) trough. It is a cylindrical prismatic lens of Fresnel type [1]. This secondary concentrator reduces the number of photovoltaic (PV) cells in the solar trough [2–6], which is used for the combined production of heat and electricity [7, 8]. The examined parabolic trough combines photovoltaic systems and thermal devices: PV cells directly exploit the sunlight

concentrated on them, and their cooling system supplies thermal energy.

The linear parabolic reflector (primary mirror) acts only in the direction transversal to the solar trough, so the entire focal line must be covered by a cell row [2]. The proposed secondary optics is interposed between the linear parabolic mirror and the linear row of PV cells [9, 10]. The sunlight collected by the parabolic mirror is intercepted by the secondary optics and concentrated, in portions, along the longitudinal axis of the solar trough.

The working principle of the cylindrical Fresnel lens (CFL) is that it transforms the focal line, concentrated by the linear parabolic mirror, into a series of focal points (Figure 1). Hence, the proposed solution allows to reduce the number of PV cells because it increases the sunlight concentration. In practice, the production of electricity is not affected by the reduction of cell number, because it is balanced by an enhancement of solar concentration.

The research started with the optical design of the secondary component [1], selecting a configuration that optimizes collection efficiency of the whole system and

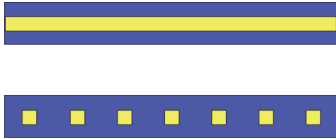


FIGURE 1: The cylindrical Fresnel lens (CFL) reconcentrates the radiation on a square photocell.

uniformity of the PV cell illumination. The optical design [11] of this secondary concentrator must take into account the characteristics of the existing trough and of the photovoltaic cells [9, 10]. The optical parameters of the secondary optics are principally determined by examining the irradiance distribution on the receiver [9, 10]. Analyses and simulations of the effects due to collector deformation, axial defocusing, tracking errors, and receiver alignment errors completed the study [1]. Some auxiliary analyses optimized operative conditions and collection efficiency of the whole system, in order to maintain elevated performance of the solar trough in real working conditions.

The solar installation is not a classical linear trough but is an innovative device provided with a two-axis tracking system that permits to follow the sun and to keep the receiver always aligned. Therefore, the insertion of a secondary element does not require to modify the original tracker.

In practice, the curve Fresnel lens was specifically designed for a trough, whose parabolic mirror focuses the light over an articulated absorber. The focal image is a rectangle, and it is concentrated on a row of squared photovoltaic cells [9, 10]. The cells are placed on a metallic tube of rectangular section, which acts as cooling system by means of a liquid flowing inside. An external protection tube in glass, enclosing cells and cooler, completes the absorber (Figure 2). The photocells directly exploit the concentrated sunlight providing electricity, while the cooling system of the cells furnishes heat. In this concentration geometry, the curve Fresnel lens must be located inside the parabolic mirror around and near the absorber, constituted by a glass tube enclosing a row of photovoltaic cells placed over a rectangular tube. The receiver photo in Figure 2 shows the cell row before the insertion of the cylindrical Fresnel lens that will reduce the number of photocells. The system concentration ratio before the introduction of the secondary optics was 140. The improvement of concentration ratio is not so great to require a change in cell type. The concentration is double, so it can be managed by the original cells.

The next phase was the practical implementation of the cylindrical Fresnel lens. Successive series of samples were manufactured, improving the quality of the production by adjusting the optical realization parameters. To check the optical quality of the realized samples, they were optically characterized in laboratory. The test procedures were especially tailored taking into account collection geometry and particular shape of the curve Fresnel lens. Some of these tests and measurements are illustrated in the next sections, presenting as exemplificative results the data measured on three lenses of the last production of CFLs.

2. Collection Geometry

Based on the optical design of the cylindrical Fresnel lens (CFL), developed as secondary optics for parabolic troughs, some samples were implemented by molding production. The research proceeded with the optical characterization of the samples by means of tests to evaluate the accuracy of the realized shape of the CFLs. These optical tests are useful both to control the progresses achieved by the successive series of mass production and to select the best performing samples among the realized optical components.

The examined solar trough uses a parabolic trough concentrator (PTC) and a series of cylindrical Fresnel lenses that concentrate solar radiation in two orthogonal directions. Figure 1 illustrates the action of a row of CFLs. The PTC concentrates the sunlight (in transversal direction) on the receiver tube; then the CFLs are interposed between the tube and the PTC and reconcentrate the light. The coupled concentrators (PTC and CFL) are optically designed to illuminate a PV cell of 10×10 mm size. In practice, the CFLs are used in the same number as the PV cells mounted on the tube and the action of the lens row is to transform the focal line into a row of focal points.

As can be seen from Figure 3, the CFL has cylindrical symmetry. Concentration takes place in both directions: Figure 3 shows the directions of light concentration. The lens is completely illuminated in the longitudinal direction (red arrow); while in the transversal axis (blue arrow), where the PTC concentrates, the rays arrive on the cell within an aperture angle of about $\pm 50^\circ$ (Figure 4(a)). The red arrow direction coincides with the axis of the cylinder of the curve Fresnel lens. The pictures in Figure 4 show top and lateral views of the CFL inserted into the trough. In Figure 4(b), the green rays are those reflected by the parabolic mirror, while the blue ones are the rays arriving from the sun; for clarity, the tube has not been drawn.

The next sections present tailored methodologies and results of laboratory tests on prototypes of these cylindrical Fresnel lenses. The purpose of the optical tests is to evaluate the quality of the production process by testing the optical behavior of the samples in terms of concentration factor and image quality. To perform these tests, a set-up has been developed to separately illuminate different lens sectors in order to analyze their optical features.

3. Tailored Optical Tests: Image Analysis

The test [12] performed on the CFL samples used a solar divergence collimator and a CMOS camera.

A solar divergence collimator [13] produces a beam with solar divergence of about 250 mm in diameter, with a high uniformity. Choosing appropriate components and set-up, the value of solar divergence results 0.48 degrees (total angular aperture, 2θ).

The beam was used directly to illuminate the CFL sample. A vertical diaphragm (Figure 5) was placed between the mirror of the solar divergence collimator and the CFL; in this way, the lens is fully illuminated in longitudinal direction, while in the transversal direction, the illumination is limited



FIGURE 2: The receiver of the solar trough is made of a tube covered by a photocell row and is inside a glass tube. This is the receiver before the insertion of the CFLs.

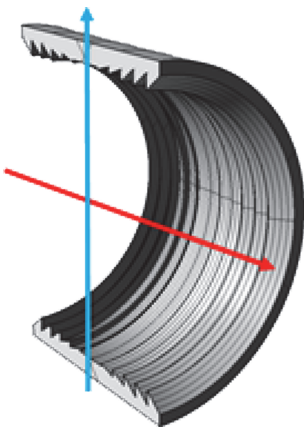


FIGURE 3: Perspective view of the CFL. The red arrow indicates the longitudinal axis (tube axis) and the blue arrow the transversal axis of the trough.

in a few millimeters, thus allowing to evaluate the behavior of the different sectors of the lens.

To do this, the CFL and detector are rotated around the same axis by placing them on a rotator. The detector is placed in the PV cell plane, so it is rotated together with the lens, as visualized in Figures 6 and 7. The angle of rotation is indicated by α in Figure 7. The axis of rotation coincides with the axis of the cylinder (red arrow in Figure 3), 25 mm behind the external side of the lens. The nominal focal plane of the CFL is situated at this distance.

Figures 6 and 7 illustrate the measurement scheme for two different α angles. By varying α , the light strip crossing the diaphragm alternately illuminates various CFL areas.

For these tests, the sensor is a CMOS camera Vector International BCi4-6600 High Resolution USB. The camera is mounted on an x-y translation support, separate from the lens rotation stage, which allows scanning a vertical plane. This is because the size of the image formed by the CFL is greater than the size of the camera sensor (CMOS image sensor 7.74×10.51 mm). In this way at each rotation of the lens, the camera had to be realigned with the lens.

An additional translator is added to vary the distance D (Figure 5). This became necessary because in visual examination, it was noted that the focal plane (i.e., the plane in which the most concentrated and uniform image was formed) was not 25 mm from the lens front face but slightly further. The translator is therefore necessary to perform the test at different lens-detector distances.

The procedure used to test the CFL samples is as follows:

- (i) The diaphragm is adjusted to generate a 5 mm wide beam on the lens.
- (ii) The lens is aligned in a central position ($\alpha = 0^\circ$).
- (iii) The sensor is aligned to the lens, and three images, upper edge, center, and bottom edge of the image, are captured by moving the camera with the x-y translator along the red arrow direction in Figure 3.
- (iv) For each lens, acquisitions of the center and edge of the image were made at angles α between -40° and $+40^\circ$ at 5° intervals and D distances between 25 mm and 40 mm at intervals of 2.5 mm.

The laboratory set-up was also simulated with the Zemax optical simulation program, using the CFL optical design. The measurement layout is reproduced in Figure 8. The source emits a beam with solar divergence. The diaphragm is set to the same width as the one used in the laboratory tests. The detector has the same size and orientation of the CMOS camera.

As can be seen from simulations, the CFL should generate an image of about 10 mm in length on the PV cell (about the same size as the long side of the CMOS camera sensor). The image should have a good uniformity of lighting inside it and quite sharp edges. In fact, the laboratory tests show that

- (i) the images produced by the analyzed lenses have no sharp edges and extend to a width much greater than the cell size;
- (ii) the lighting has a maximum in the central part and it gradually falls towards the lateral zones;
- (iii) the different lens sectors should, by symmetry, produce the same image on the camera, unless small differences are due to the inclination of the lens with respect to the diaphragm plane; instead, the images of the lateral sectors ($\alpha \neq 0^\circ$) are very degraded compared to the central sector ($\alpha = 0^\circ$).

4. Images Results and Discussion

The results, as measured imaged and simulations, are illustrated for three selected samples of the last CFL production, named lens_A, lens_B, and lens_C. They are able to create (in the image plane at a suitable distance) images with better optical characteristics with respect to the previous productions. Figures 9–16 represent a selection of the most significant images measured on the three lenses, comparing each acquired image with the corresponding simulated image.

The tests performed in laboratory are done only on the secondary lens, so the concentration due to the parabolic trough is absent. When the lens is mounted on the parabolic trough, the rectangles in Figures 9–16 become squares.

Figures 9(a), 9(b), and 9(c) are images acquired at the nominal focal distance ($D = 25$ mm) without rotation

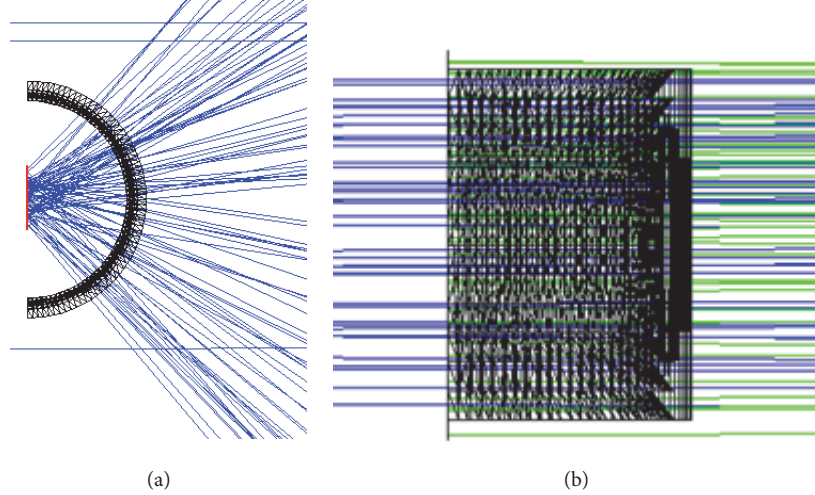


FIGURE 4: (a) Top view of the lens: the red segment represents the CFL image plane. (b) Side view of the lens: the green lines are the rays reflected by the trough.

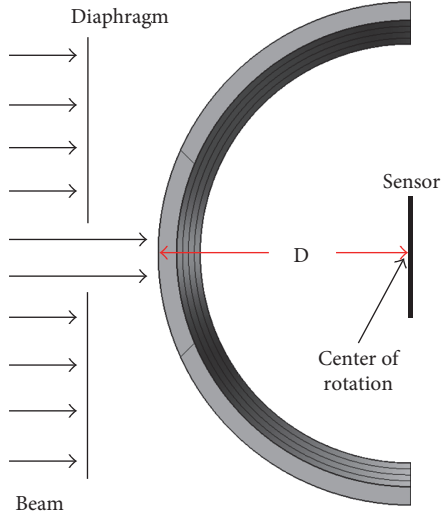


FIGURE 5: Top view of the lens. Lens and sensor rotate around the same axis that coincides with the CFL axis.

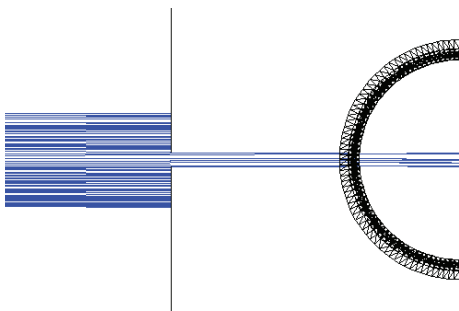


FIGURE 6: The light strip rays form an angle $\alpha = 0^\circ$.

$(\alpha = 0^\circ)$, that is, using the set-up of Figure 6. They evidence that the sample manufacturing is quite defective for lens_A, is better for lens_C, and reaches an acceptable

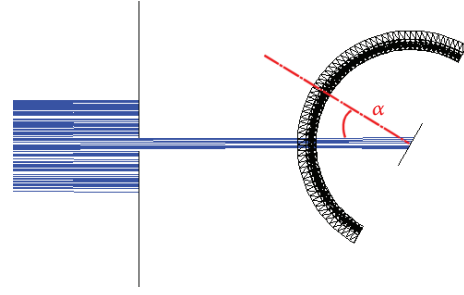


FIGURE 7: The light strip rays form an angle $\alpha = 30^\circ$.

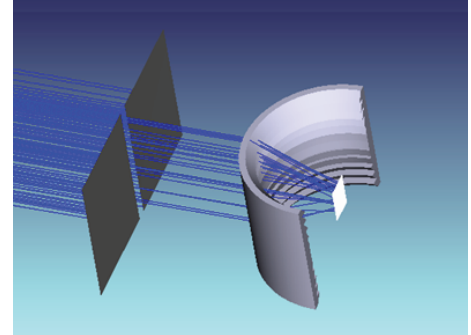


FIGURE 8: Zemax simulation of the layout of the laboratory set-up.

uniformity of illumination for lens_B. The related ray-tracing simulation gives Figure 9(d) as image map at $D = 25 \text{ mm}$: the simulated image is in fair agreement with Figures 9(a), 9(b), and 9(c). For the simulated images, a code color is used: blue for the minimum, red for the maximum (never reached), and green is about 40% of the maximum.

Considering lens_B, Figures 10(a), 11(a), 12(a), and 13(a) were obtained from the images acquired at the

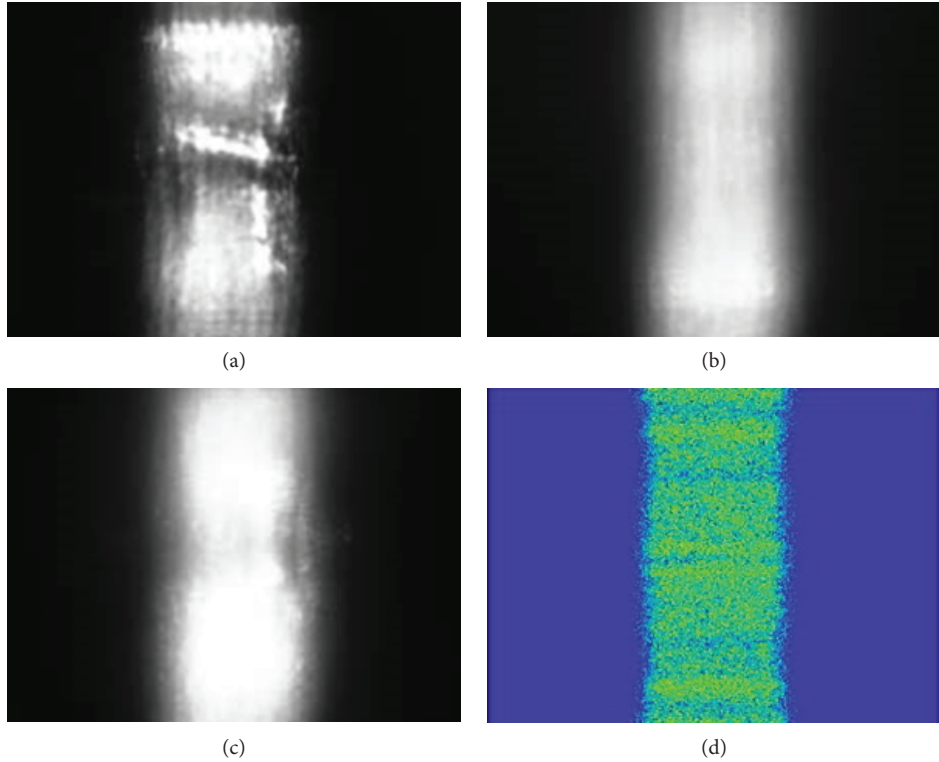


FIGURE 9: Images at $D = 25$ mm with $\alpha = 0^\circ$ generated by lens_A (a), lens_B (b), and lens_C (c), compared with the Zemax simulation (d).

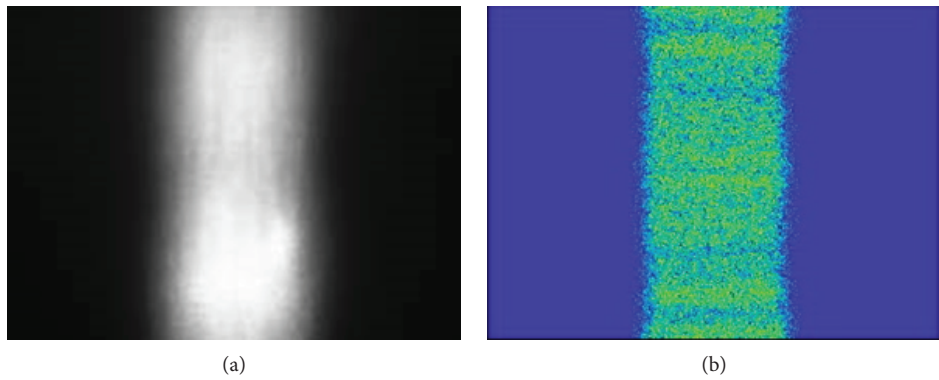


FIGURE 10: Images at $D = 25$ mm with $\alpha = 10^\circ$ generated by lens_B (a), compared with the Zemax simulation (b).

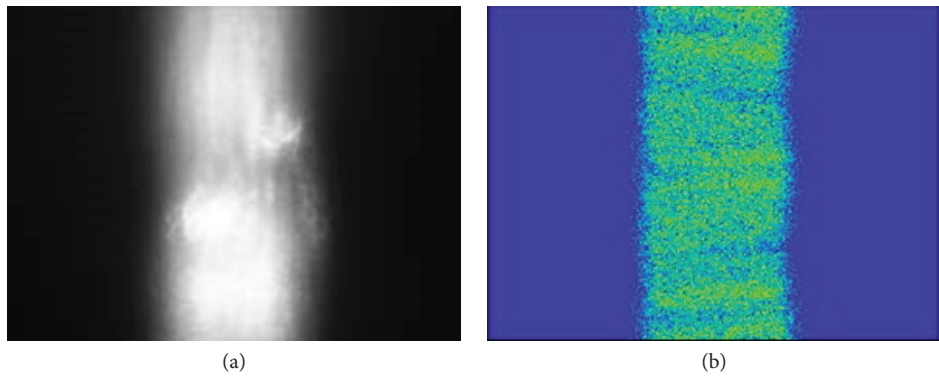


FIGURE 11: Images at $D = 25$ mm with $\alpha = 20^\circ$ generated by lens_B (a), compared with the Zemax simulation (b).

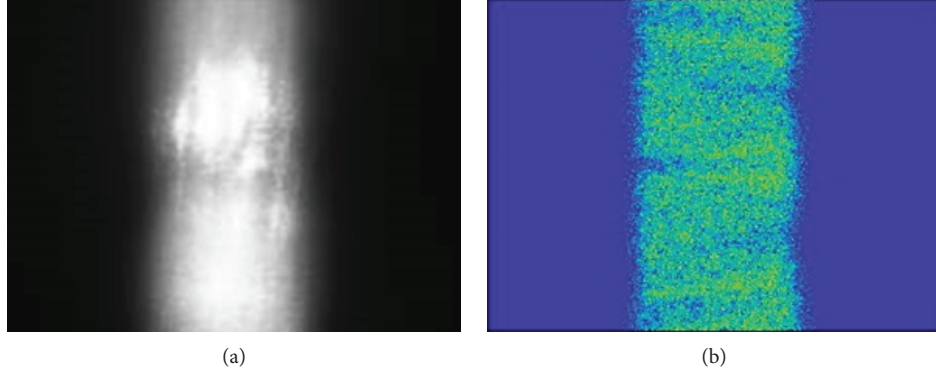


FIGURE 12: Images at $D = 25$ mm with $\alpha = 30^\circ$ generated by lens_B (a), compared with the Zemax simulation (b).

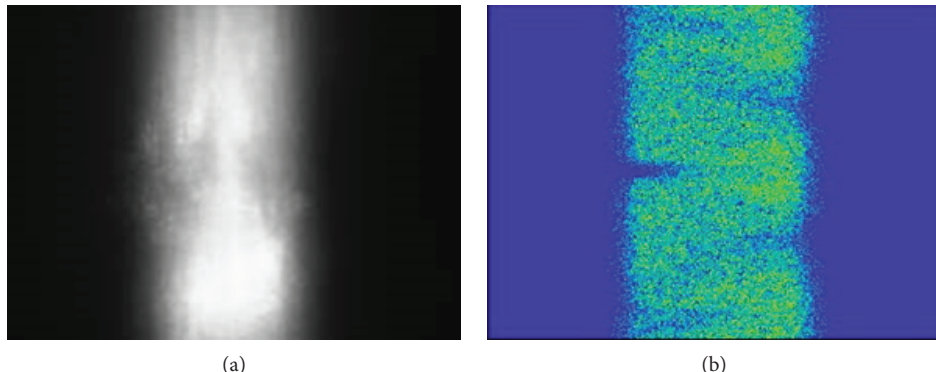


FIGURE 13: Images at $D = 25$ mm with $\alpha = 40^\circ$ generated by lens_B (a), compared with the Zemax simulation (b).

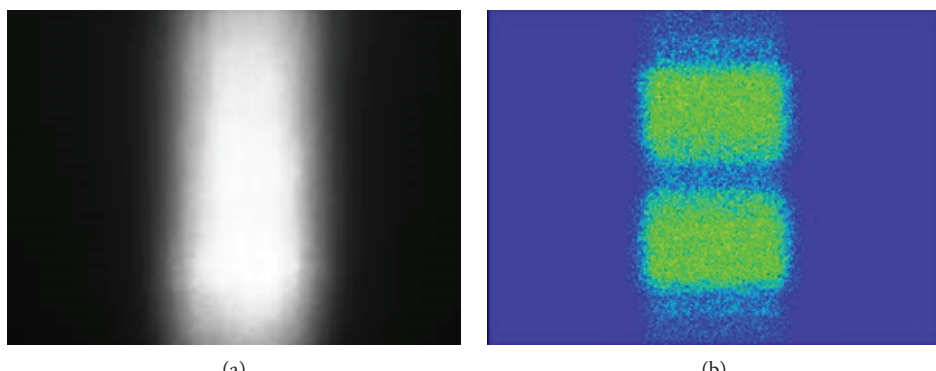


FIGURE 14: Images at $D = 30$ mm with $\alpha = 0^\circ$ generated by lens B (a), compared with the Zemax simulation (b).

nominal focal distance ($D = 25$ mm) for positive α angles ($10^\circ \leq \alpha \leq 40^\circ$). The images pertaining to negative α angles are similar and therefore are not reported. For each case examined, a Zemax simulation was performed in the corresponding configuration (the values of the parameters α and D are indicated in the captions). The aperture width, dimension, and orientation of the detector used in the simulations correspond exactly to the set-up used in laboratory to allow direct comparison. The irradiance

maps (Figures 10(b), 11(b), 12(b), and 13(b)) obtained from the simulations are shown alongside the corresponding image captured with the camera. The image distortion at angles $\alpha \neq 0$ is due to the inclination of the detector with respect to the diaphragm plane.

The principal test concerns the angular scan, so the images measured varying the α angle, which give information about the uniformity of manufacturing of the cylindrical lens.

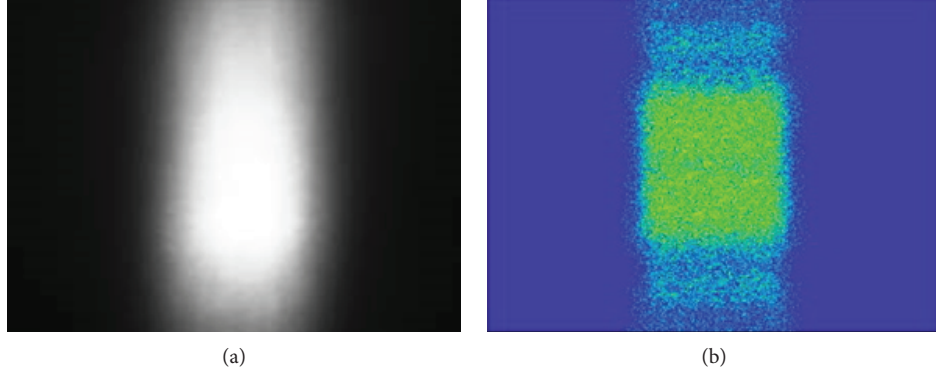


FIGURE 15: Images at $D = 35$ mm with $\alpha = 0^\circ$ generated by lens_B (a), compared with the Zemax simulation (b).

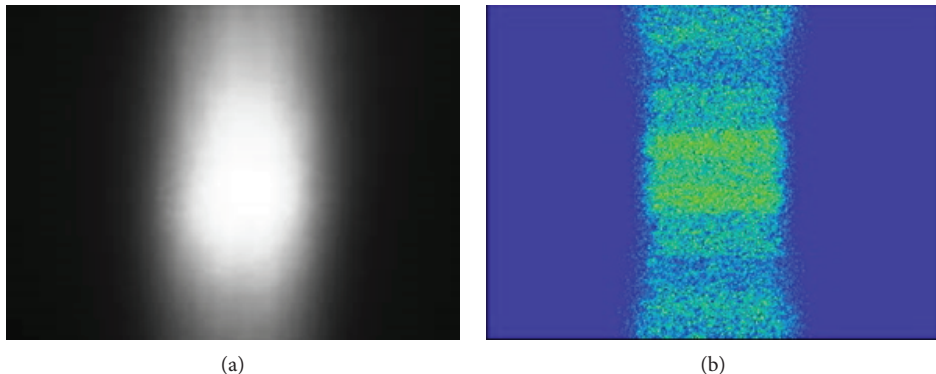


FIGURE 16: Images at $D = 40$ mm with $\alpha = 0^\circ$ generated by lens_B (a), compared with the Zemax simulation (b).

On the other hand, some measurements varying the D distance are useful to individuate the best focusing position to illuminate the PV cell area.

Again, choosing lens_B, Figures 14(a), 15(a), and 16(a) present acquisitions with the CFL sample in central position ($\alpha = 0^\circ$) and the distance D variable between 30 mm and 40 mm. For comparison, Figures 14(b), 15(b), and 16(b) report the irradiance maps calculated in the planes at the examined distances D between lens and detector.

The main requirements concern the concentration factor and uniformity of illumination over the cell area. The concentration should be around the value that maximizes the photovoltaic conversion of the PV cell. The collected light should be uniformly distributed over the cell area to have a good functioning of the cell. If the photocell is unevenly lighted, it does not work well and can disturb the whole cell line or even cause damage.

The three examined samples are compared in Figures 9(a), 9(b), and 9(c), and the best performing one seems to be lens_B. The results of the angular scan test on lens_B, reported in Figures 9(b), 10(a), 11(a), 12(a), and 13(a) ($0^\circ \leq \alpha \leq 40^\circ$), indicate that the sample contains some manufacturing imperfections, which appear as the α angle increases. The effect of defocusing on lens_B is analyzed in Figures 9(b), 14(a), 15(a), and 16(a): elevated

levels of lighting uniformity are obtained at 25 and 30 mm. Hence, the optimal position to place the CFL is between the nominal focal distance (25 mm) and $D = 30$ mm.

The comparison with the irradiance maps shows a general agreement between the acquired images and the results of the Zemax ray-tracing simulations.

5. Tailored Optical Tests: Concentration Measurements

A quantitative assessment of the solar concentration factor was effectuated by laboratory measurements. Due to the peculiarity of the system geometry, it was chosen to calculate the concentration factor C as the ratio between the density (δ_C) of luminous power on the cell and the power density (δ_L) on the lens:

$$C = \frac{\delta_C}{\delta_L}. \quad (1)$$

The quantity δ_C is the ratio between the signal (S_C) measured in the presence of the lens and the area (a_R) illuminated by the receiver itself: $\delta_C = S_C/a_R$, while δ_L is the ratio between the signal (S_L) incident on the lens and the illuminated area (a_R) of the receiver: $\delta_L = S_L/a_R$.

The illuminated area in the two cases is the same and is limited in one direction by the cell height (10 mm), in the other by the beam width (3 mm).

In conclusion,

$$C = \frac{\delta_C}{\delta_L} = \frac{S_C}{S_L}. \quad (2)$$

The set-up for the measurements is similar to the layout previously described (Figures 5–8), but with two differences.

- (i) The sensor used in this case is a Hamamatsu S6337-01 silicon photodiode, with 18×18 mm active area. A mask with a square aperture of 10 mm side was placed in front of the sensor, to limit the active area to the size of the photovoltaic cell. The center of the lens and center of the sensor are aligned with the beam direction.
- (ii) The detector does not rotate solidly with the lens but is placed on a fixed support and is constantly facing in direction perpendicular to the beam, as in Figure 5. The reasons for this choice are essentially two. The first is that this procedure eliminates the uncertainty due to the fact that the sensor response is not the same at various angles of incidence. The second reason is that, as α changes, the determination of δ_C involved a factor $\cos \alpha$, because $a_R(\alpha) = a_R(\alpha = 0) \times \cos \alpha$. This is not the case for δ_L because, due to the cylindrical symmetry, the lens illuminated area is always the same as α varies, and then $a_L(\alpha) = a_L(\alpha = 0)$. In conclusion, the value of C at different α would have been difficult to compare. By keeping the photodiode in a fixed position, however, it is possible to make a direct comparison of the behavior of the various lens sectors in terms of concentration factor.

The procedure used for the quantitative measurements of C is as follows.

- (1) The aperture width of the diaphragm is set to 3 mm.
- (2) The lens-receiver distance is set to $D = 25$ mm.
- (3) An angular scan is performed between $\alpha = 40^\circ$ and $\alpha = -40^\circ$ at 5° steps. For each angle, the signal of the photodiode $S_C(\alpha)$ was acquired.
- (4) The lens was removed, and point (3) was repeated to capture the signal $S_L(\alpha)$ incident on the lens.
- (5) The procedure was repeated for $D = 27.5$ mm, 30 mm, 32.5 mm, and 35 mm.

6. Concentration Results and Discussion

The results of the measurement of the concentration factor C are presented in Tables 1, 2, and 3 as a function of the α angle at the different lens-receiver distances considered. The C values are discussed for three samples of the last

production: lens_A, lens_B, and lens_C. Each table refers to a prototype of cylindrical Fresnel lens.

Only the concentration ratio of the secondary lens is measured, because the laboratory set-up does not reproduce the parabolic trough focalization. The value of C is circa two, so when the CFL is inserted inside the solar trough, the original concentration is doubled.

The results of concentration factor C are in agreement with the CLF behavior discussed in Section 4 about the images. The visual inspection shows that the best working plane is located farther than 25 mm (nominal focal distance). In effect, the C values increase for D around 30 mm or 32.5 mm.

The graphs in Figures 17, 18, and 19 illustrate the trend of the C concentration factor as the α angle changes for three samples of CFL. For more readability, only results of $D = 25$ mm, 30 mm, and 35 mm are reported, and the other curves are among them.

The mean values of concentration factor are reported in Table 4 for each lens-receiver distance D and for the three examined lenses. The maximum value of C is 1.73 for lens_A, 2.13 for lens_B, and 2.09 for lens_C. The corresponding optimal positions are at $D = 35$ mm for lens_A, $D = 30$ mm for lens_B, and $D = 32.5$ mm for lens_C.

Some considerations can be done to conclude the concentration factor assessment.

- (i) The theoretical concentration factor, calculated with the formulas described in Section 5 and using Zemax with the layout of Figure 8, is $C = 3.4$ for a distance $D = 25$ mm. Concentration values measured in laboratory are therefore much lower than expected for the three analyzed samples. In addition, the maximum value should be recorded for $D = 25$ mm at the nominal focal length of the CFL, while in reality the maximum is found for higher distances.
- (ii) The concentration factor should remain constant along the entire angular profile of the CFL. In fact, only lens_B shows such behavior.
- (iii) The behavior of the three CFL samples is not the same, although the measurements have been carried out with the same procedure. Actually, the trend of C for lens_A has a minimum in the center of the lens ($\alpha = 0$) and increases toward the edges; this fact is also found in the images in Section 4, in which it can be noted that for $\alpha \approx 0$, there is a shadow area at the center of the images. For lens_C, the values are slightly lower on either side.

Test results show that the idea of adding a secondary system to perform a concentration on the longitudinal axis is both feasible and convenient. The lens construction solution, however, did not dare to get the expected performance for the CFL. The study has also provided accurate guidance on the emerging criticalities and possible solutions that will necessarily take into account the lens construction technique.

TABLE 1: Concentration factor C as a function of α for lens_A.

α ($^{\circ}$)	$D = 25$ mm	$D = 27.5$ mm	$D = 30$ mm	$D = 32.5$ mm	$D = 35$ mm
40	1.56	1.67	1.77	1.84	1.87
35	1.51	1.64	1.74	1.83	1.86
30	1.46	1.58	1.69	1.80	1.84
25	1.45	1.53	1.62	1.74	1.79
20	1.42	1.51	1.59	1.68	1.71
15	1.38	1.46	1.54	1.62	1.65
10	1.36	1.45	1.51	1.56	1.58
5	1.35	1.44	1.49	1.54	1.57
0	1.35	1.44	1.49	1.54	1.56
-5	1.34	1.42	1.48	1.54	1.56
-10	1.36	1.45	1.51	1.57	1.60
-15	1.39	1.47	1.55	1.61	1.65
-20	1.42	1.52	1.59	1.67	1.72
-25	1.46	1.56	1.65	1.74	1.80
-30	1.52	1.63	1.73	1.83	1.87
-35	1.58	1.69	1.81	1.89	1.89
-40	1.65	1.76	1.84	1.90	1.90

TABLE 2: Concentration factor C as a function of α for lens_B.

α ($^{\circ}$)	$D = 25$ mm	$D = 27.5$ mm	$D = 30$ mm	$D = 32.5$ mm	$D = 35$ mm
40	1.96	2.03	2.07	2.07	2.05
35	1.98	2.05	2.09	2.10	2.06
30	1.98	2.06	2.11	2.12	2.08
25	2.00	2.07	2.11	2.11	2.09
20	2.02	2.11	2.15	2.13	2.10
15	2.00	2.11	2.16	2.16	2.13
10	1.98	2.07	2.13	2.13	2.10
5	1.97	2.06	2.10	2.10	2.08
0	2.00	2.09	2.15	2.15	2.13
-5	2.03	2.13	2.19	2.19	2.16
-10	2.04	2.13	2.18	2.17	2.13
-15	2.02	2.11	2.17	2.17	2.15
-20	2.03	2.13	2.18	2.17	2.14
-25	2.02	2.11	2.15	2.15	2.12
-30	2.01	2.08	2.13	2.13	2.10
-35	1.99	2.07	2.12	2.12	2.07
-40	2.00	2.07	2.10	2.09	2.05

7. Conclusion

The purpose was to develop a secondary optics for a concentrating photovoltaic trough that increases the solar concentration and reduces the photovoltaic cell number. The proposed cylindrical Fresnel lens (CFL) focuses in the direction where the trough does not concentrate: in practice, it transforms the focal line into a series of focal points.

Some lens prototypes were produced based on the CFL optical design. Tailored tests were developed to optically characterize and check the quality of the manufactured CFL

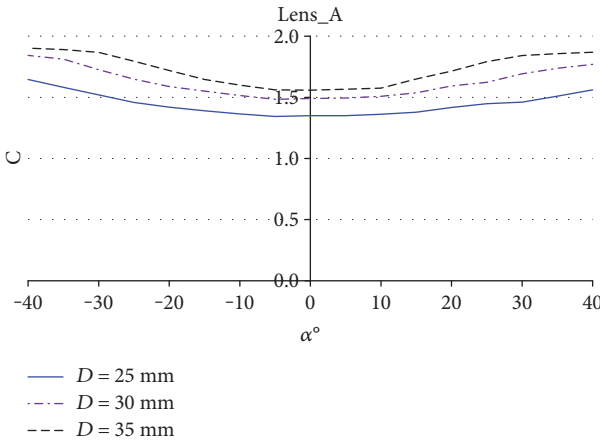
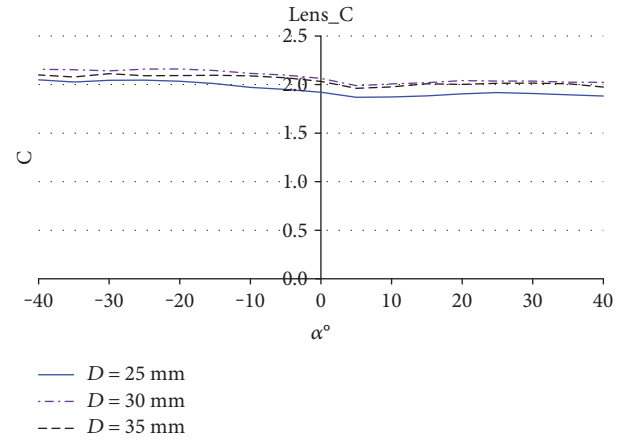
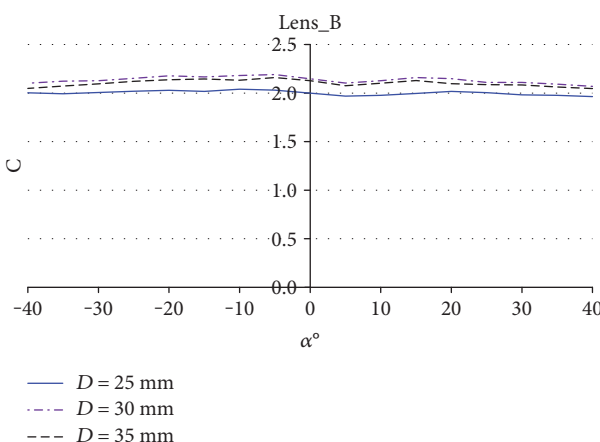
samples [12]. The performed tests help to localize the zones with defects, so to improve the lens production.

The image analysis gives a qualitative assessment of the CFL quality: every image measured on a lens indicates the level of uniformity of sun concentration, which is fundamental to correctly exploit the solar cells. The behavior of each examined lens was simulated using a ray-tracing software (Zemax), and the simulated CFL image is in general agreement with the measured image, but some exceptions are presented.

Quantitative measurements assessed the concentration factor C , for various angles along the curve lens and for

TABLE 3: Concentration factor C as a function of α for lens_C.

α ($^{\circ}$)	$D = 25$ mm	$D = 27.5$ mm	$D = 30$ mm	$D = 32.5$ mm	$D = 35$ mm
40	1.88	1.98	2.02	2.03	1.97
35	1.90	1.98	2.03	2.05	2.01
30	1.91	1.99	2.04	2.05	2.02
25	1.92	2.00	2.04	2.06	2.01
20	1.91	2.00	2.04	2.05	2.00
15	1.88	1.98	2.02	2.05	2.01
10	1.87	1.97	2.01	2.01	1.98
5	1.87	1.95	1.99	2.00	1.96
0	1.92	2.02	2.06	2.08	2.03
-5	1.95	2.06	2.10	2.11	2.07
-10	1.97	2.07	2.12	2.14	2.09
-15	2.01	2.11	2.15	2.14	2.10
-20	2.03	2.13	2.16	2.14	2.09
-25	2.05	2.13	2.16	2.15	2.09
-30	2.05	2.12	2.14	2.14	2.11
-35	2.03	2.10	2.15	2.18	2.08
-40	2.05	2.14	2.16	2.15	2.10

FIGURE 17: Concentration factor C as a function of α for lens_A.FIGURE 19: Concentration factor C as a function of α for lens_C.FIGURE 18: Concentration factor C as a function of α for lens_B.

different lens-cell distances D . The maxima of average C are 1.73 for lens_A, 2.13 for lens_B, and 2.09 for lens_C, respectively, obtained at $D = 35$ mm, 30 mm, and 32.5 mm. For each lens, C varies depending on D , so the C maximum corresponds to the best distance D for placing the cell.

The trough concentration ratio before the introduction of the secondary optics was 140; since the CFL doubles it, C approaches 300 for the system with primary mirror and secondary lens. This C value allows to utilize the original PV cells and avoids the need to employ more expensive multijunction cells.

The optical performance improves with the successive CFL productions. The three selected samples reach a higher concentration factor and create images with better optical characteristics with respect to the previous products. In spite of this, they do not meet the requirements in terms of concentration and lighting uniformity on the cell plane (in fact

TABLE 4: Mean values of the concentration factor C .

Lens	$D = 25 \text{ mm}$	$D = 27.5 \text{ mm}$	$D = 30 \text{ mm}$	$D = 32.5 \text{ mm}$	$D = 35 \text{ mm}$
Lens_A	1.44	1.54	1.62	1.70	1.73
Lens_B	2.00	2.09	2.13	2.12	2.10
Lens_C	1.95	2.04	2.08	2.09	2.04

the C maximum is at different D), so the manufacturing process needs further improvements.

The study and the tests have made possible to detect the criticality of the first CFL prototypes, and they provide some precise indications of the possible actions to be implemented, also considering a rethinking of the lens construction processes adopted, which can be considered as the main responsible for the loss of optical lens performance.

- [12] D. Fontani, F. Francini, and P. Sansoni, “Optical characterisation of solar concentrator,” *Optics and Lasers in Engineering*, vol. 45, pp. 351–359, 2007.
- [13] D. Fontani, P. Sansoni, E. Sani, S. Coraggia, D. Jafrancesco, and L. Mercatelli, “Solar divergence collimators for optical characterisation of solar components,” *International Journal of Photoenergy*, vol. 2013, Article ID 610173, 10 pages, 2013.

Conflicts of Interest

The authors declare that they have no conflicts of interest.

References

- [1] D. Fontani, P. Sansoni, F. Francini, and D. Jafrancesco, *Designing an Innovative Secondary Optics for Parabolic Trough*, *Proceedings of SWC2015*, Daegu, Korea, International Solar Energy Society, 2016.
- [2] D. W. Kearney, *Parabolic Trough Collector Overview, Parabolic Trough Workshop 2007 at the National Renewable Energy Laboratory*, Golden CO, 2007, <http://www.doc88.com/p-882640289219.html>.
- [3] D. Krüger, Y. Pandian, K. Hennecke, and M. Schmitz, “Parabolic trough collector testing in the frame of the REACT project,” *Desalination*, vol. 220, no. 1–3, pp. 612–618, 2008.
- [4] G. C. Bakos, I. Ioannidis, N. F. Tsagas, and I. Seftelis, “Design, optimisation and conversion-efficiency determination of a line-focus parabolic-trough solar-collector (PTC),” *Applied Energy*, vol. 68, no. 1, pp. 43–50, 2000.
- [5] H. Price, E. Lüpfert, D. Kearney et al., “Advances in parabolic trough solar power technology,” *Journal of Solar Energy Engineering*, vol. 124, no. 2, pp. 109–125, 2002.
- [6] D. E. Prapas, B. Norton, and S. D. Probert, “Optics of parabolic-trough, solar-energy collectors, possessing small concentration ratios,” *Solar Energy*, vol. 39, no. 6, pp. 541–550, 1987.
- [7] W. Weiss and M. Rommel, *Solar Heat for Industrial Process: State of the Art—Medium Temperature Collectors*, IEA-SHC Task 33/IV, 2005.
- [8] J. Klapp, J. L. Cervantes-Cota, and J. F. Alcalá Chávez, *Towards a Cleaner Planet: Energy for the Future*, Springer, 2007.
- [9] T. C. Kandpal, S. S. Mathur, and A. K. Singhal, “Optical performance of a composite parabolic trough,” *Applied Energy*, vol. 19, no. 3, pp. 231–239, 1985.
- [10] H. M. Güven and R. B. Bannerot, “Determination of error tolerances for the optical design of parabolic troughs for developing countries,” *Solar Energy*, vol. 36, no. 6, pp. 535–550, 1986.
- [11] R. Winston, J. C. Miñano, P. Benítez, N. Shatz, and J. C. Bortz, *Nonimaging Optics*, Elsevier Academic Press, Amsterdam, 2005.